DEPARTMENT OF PHYSICS
UNIVERSITY OF JYVÄSKYLÄ
RESEARCH REPORT No. 6/2003

COMPETING STRUCTURES IN VERY LIGHT BISMUTH ISOTOPES

BY
PÄIVI NIEMINEN

Academic Dissertation
for the Degree of
Doctor of Philosophy

To be presented, by permission of the
Faculty of Mathematics and Natural Sciences
of the University of Jyväskylä,
for public examination in Auditorium FYS-1 of the
University of Jyväskylä on October 31, 2003
at 12 o'clock noon

Jyväskylä, Finland
October 2003

ISBN 978-951-39-3144-5

URN:ISBN:978-951-39-3144-5

Preface

The work reported in this thesis was carried out at the Department of Physics of the University of Jyväskylä during the years 1998-2003.

First of all, I want to sincerely thank my supervisors Dr. Sakari Juutinen and Prof. Rauno Julin for all their help and support. Their experience in the field has guided me past many pitfalls throughout the course of this work. The successful realisation of the experiments has been a feat of strength from the past and present members of the γ-RITU group, to whom I wish to express my gratitude. A special mention in the γ group belongs to Dr. Pete Jones, Dr. Paul Greenlees and Mr. Panu Rahkila for their help on electronics, data analysis and computers, and to the former members of the 'gamma girls' who have defended their theses and thereby shown the way. The required expertise in α-decay spectroscopy has been provided by Prof. Matti Leino and the members of his RITU group. During the measurements, especially Dr. Juha Uusitalo and Mr. Heikki Kettunen have shown a thorough understanding of the logic of RITU and made the experiments run smoothly. Thanks go also to the cyclotron staff for delivering the required ion beams. However, the picture only becomes complete when every member of the combined group is appreciated for the inspiring spirit and versatile lunch-break discussions during working hours, and for the get-togethers outside the lab. It has also been a great pleasure to meet the numerous colleagues from the worldwide nuclear physics community who have participated in experiments, summer schools and conferences both in Finland and abroad.

The atmosphere of the Department of Physics has been extensively praised - and for a very good reason. The open door policy and equal opportunities have formed a community in which it has been a privilege to work. Competitiveness has not dominated during the working hours but has mainly concentrated in other arenas like the sports field during the annual athletics event, skiing tracks or a rowing boat when there is five kilometers to go before the finishing line of a 60-km race. The whole staff of the department is thanked for the encouragement and solidarity which can guarantee the best possible outcome of a demanding process, like that of preparing a Ph.D. thesis.

As material requirements have also to be met, the financial support from the University of Jyväskylä, the Academy of Finland, Finnish Cultural Foundation and Emil Aaltonen Foundation has been accepted and is gratefully acknowledged.

Finally, I would like to thank those of my friends who are not included in the list above, and my parents for all their support and for being proud and constantly amazed at my achievements.

Jyväskylä, September 2003

Päivi Nieminen

Abstract

In the present work, the structure of the very neutron-deficient nuclei ^{191,193}Bi has been studied at the Accelerator laboratory of the University of Jyväskylä using an experimental apparatus which combines arrays of Ge detectors and the high-transmission recoil separator RITU. The very selective recoil-decay tagging, isomer tagging and recoil gating techniques have provided the first identification of prompt and delayed γ rays from ^{193}Bi and ^{191}Bi, resulting in extensive level schemes for both nuclei. Excitation energies of the isomeric $13/2^+$ states, observed in all the heavier odd-A bismuth isotopes have been established and strongly coupled bands based on them have been constructed indicating oblate deformation. The proton $2p-2h$ core excitation responsible for the oblate shape has been associated also with the observed negative-parity bands. Bands feeding the $1/2^+$ intruder state in both nuclei suggest a change in shape for this structure when going from ^{193}Bi to ^{191}Bi. Some quasiparticle excitations corresponding to those which dominate the structure of the heavier isotopes down to ^{195}Bi have been observed to survive in ^{193}Bi and interpreted as the odd proton coupled to spherical states of the ^{192}Pb core. The present results extend the knowledge on the odd-A bismuth nuclei close to the proton drip line and are in agreement with the picture of coexistence of spherical and deformed nuclear shapes, widely established in neutron-deficient nuclei in the tin and lead regions.

Contents

1 Introduction

The first principles in explaining the structure of a nucleus were developed based on the knowledge gained by studying materials existing in nature. As experimental methods to produce (wo)man-made isotopes have become available, information on nuclear species lying further away from the valley of stability has remarkably increased. Many nuclei have been observed to exhibit structural properties which could not have been inferred from observations made of the naturally abundant isotopes. Some neutron-rich nuclei in the $A \sim 10$ region can be described as a neutron halo surrounding a compact core [Tan85]. Highly elongated superdeformed shapes were first identified in the ^{152}Dy ($Z = 66$) nucleus [Twi85, Twi86], and have since been established in approximately 120 neutron-deficient isotopes mainly with $57 < Z < 68$ and $79 < Z < 84$ [Sin02]. More recently, the observation of regular bands with enhanced M1 transitions and weak or absent E2 crossover transitions in nearly spherical nuclei around ^{198}Pb ($Z = 82$) led to the introduction of the new concept of magnetic rotation [Fra93].

The continuous development of nuclear physics is founded on the dialogue between theoretical modelling and experimental measurements. To extend this basis, experimental nuclear physics today concentrates on studying nuclear matter under extreme conditions like high angular momentum, high excitation energy or an excess of either protons or neutrons over the other constituent. When pursuing these limits, new challenges arise. All nuclear reactions are based on the re-organisation of nucleons from the interacting beam and target nuclei in a manner that is determined by the mass and proton numbers of both reaction partners and the kinetic energy of the beam particle. As the resultant nuclei and properties that can be measured from them depend on the type of reaction, the relatively narrow selection of beam and target combinations can restrict the use of a given method to a small region of the nuclear chart. Nowadays, the most extensive efforts to produce new exotic nuclei focus on the development of radioactive beam facilities. When the residual nucleus has been successfully synthesised, a further demand is to observe emitted radiation which releases the energy excess from the system and simultaneously reveals properties of the nucleus of interest. The selection of the rarely occurring valid signals from a background which is usually many orders of magnitude greater requires the development of efficient and selective experimental devices as well as sophisticated analysis methods.

In some nuclear mass regions, low-lying excited states can be associated with a variety of nuclear shapes. The shape-coexistence phenomenon was introduced when the first excited $I^\pi = 0^+$ state in ^{16}O ($Z = 8$) was proposed to be deformed [Mor56]. However, the largest selection of nuclei in which coexistent deformed configurations at relatively

low excitation energies have so far been observed, have a proton number close to the magic $Z = 50$ (tin) or $Z = 82$ (lead) and lie in the neutron mid-shell region. The explanation for these structures can be derived from the intruder picture, where the development of non-sphericity is associated with shell-model intruder states formed by exciting protons across the magic shell gap [Hey83, Woo92]. An alternative approach to account for the shape coexistence phenomenon is provided by the Nilsson model [Nil55] where the energies of single-particle states are calculated in a deformed nuclear potential. These two models have been observed to be in good overall agreement, as demonstrated by Heyde *et al.* [Hey89] for the lowest 0^+ intruder states in the neutron-deficient even-even Pb isotopes.

The accumulation of data is quite comprehensive in the tin region where the neutron mid-shell nuclei lie close to the β-stability line. The low-lying excited states in these nuclei can be reached via light-ion induced compound reactions while the higher-lying levels can be probed using fusion-evaporation or binary reactions. The complications in the high-spin studies arise from the lack of suitable beam and target combinations. The only possible exit channels for the production of the nuclei of interest in this region via fusion-evaporation reactions may be rare, involving *e.g.* the evaporation of an α particle together with a few neutrons. For example, the stable nucleus ^{112}Cd can be produced in the ^{110}Pd(α,2n) reaction [Kum92] but there is no access to this isotope via neutron evaporation channels in compound nucleus reactions with heavier beams. In an experiment for ^{116}Sn, the yield for the ^{104}Ru(^{18}O,α2n) reaction was only 1% of the yield for the 4n channel leading to ^{118}Te [Sav98]. On the other hand, studies using binary reactions with heavy-ion beams require either particle detectors for the observation of the binary products in thin-target experiments, or very high statistics for γ-γ coincidence techniques used in the identification of γ rays in thick-target experiments. However, the production cross sections of these near-stable nuclei are high (even hundreds of millibarns) compared to the yield of the very neutron-deficient isotopes in the lead region, leading to extensive data on shape coexistence in the $Z = 50$ region.

The first observation of shape coexistence in the lead region was made in isotope shift measurements for the odd-A Hg nuclei [Fra75, Bon76] and subsequently confirmed via α-decay fine-structure measurements, β-decay studies and γ-ray spectroscopy [Hey83, Woo92]. More recently, coexisting shapes in the neutron-deficient Hg ($Z = 80$), Tl ($Z = 81$), Pb and Po ($Z = 84$) isotopes have been examined via the observation of collective bands in in-beam γ-ray spectroscopic measurements [Jul01]. There are no similar data available for the very light Bi ($Z = 83$) isotopes to complement the results from the α- and β-decay studies. Therefore, the objective of the present work is to use in-beam spectroscopic methods to explore whether deformed structures corresponding to those observed in the neighbouring isotopes can be established also in the ^{191,193}Bi nuclei (see Figure 1.1).

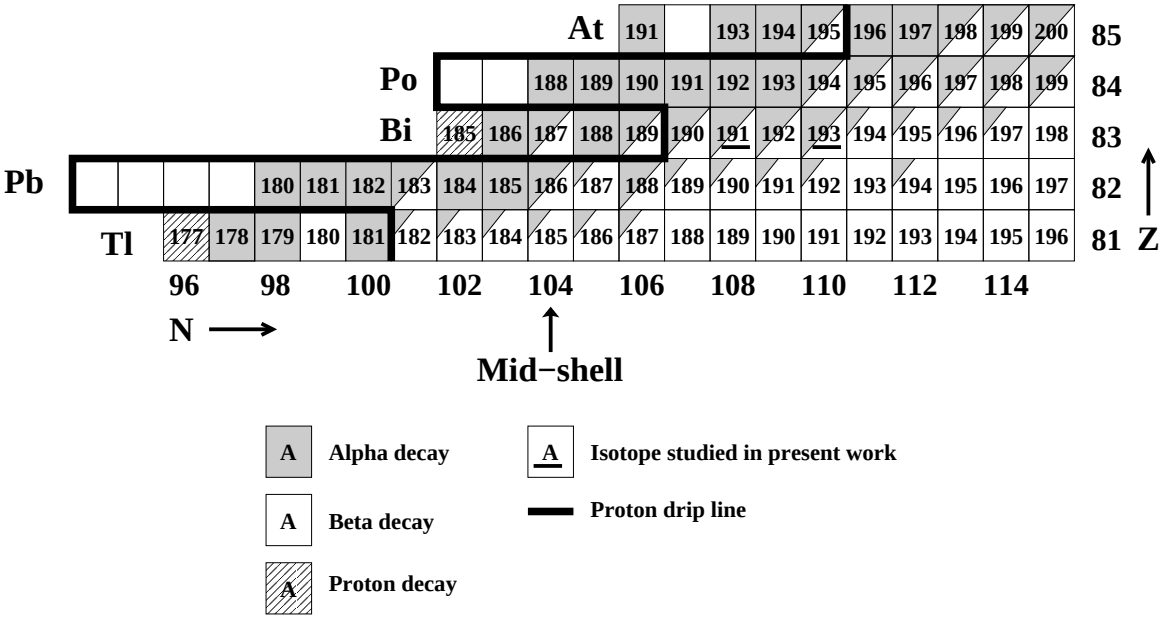

Figure 1.1: Part of the nuclear chart relevant to the present work. The known isotopes (data published) are marked with their mass numbers and the shaded area indicates the intensity of the α-decay branch. Mass numbers of bismuth isotopes studied in the present work are underlined. The one-proton drip line [Lir76, Nov02] is drawn with a thick line.

As the nuclei exhibiting non-spherical shapes in the lead region are very neutron-deficient, the only method to access these isotopes for in-beam spectroscopic studies is to use heavy-ion induced fusion-evaporation reactions. Although the nuclei of interest may result from the synthesis of a larger selection of stable beam-target combinations than in the tin mid-shell region, the significantly lower cross sections make these experiments very demanding. Moreover, the γ rays of interest have to be separated from the background originating from fission, which is the dominant exit channel in reactions leading to heavy nuclei and increases in going towards the proton drip line. However, since the fusion-evaporation reactions preferentially populate high-spin states, they fulfill the requirements of the present work where the primary aim is to study collective structures based on the deformed intruder states. The main drawback of the compound-nucleus reactions is their inability to populate the non-yrast states which would yield more detailed information on the intrinsic structure of the nucleus.

The experiments reported in the present work were performed at the Accelerator Laboratory of the University of Jyväskylä, Finland (JYFL). The ^{193}Bi and ^{191}Bi nuclei were produced in fusion-evaporation reactions initiated by ^{32}S and ^{52}Cr beams incident on ^{165}Ho and ^{142}Nd targets, respectively. The first observation of prompt γ rays from these nuclei was realised using the Jurosphere II Ge-detector array at the target position of the gas-filled recoil separator RITU [Lei95a], which was used to separate

the fusion products recoiling out of the thin target from the primary beam and fission fragments. At the separator focal plane, the recoils were implanted into a Si detector and γ rays following the de-excitation of isomeric states were observed with a small array of Ge detectors in close geometry around the Si-detector chamber. The first identification of γ rays feeding the ground state of ^{193}Bi was made based on the measured excitation functions while for the other α-decaying states in the nuclei of interest, the recoil-decay tagging (RDT) method [Sim86, Pau95] was utilised. Isomer tagging was exploited in the correlation of prompt and delayed γ rays across isomeric states and recoil-gated data were used to examine γ-γ coincidences.

In this thesis, the experimental methods and instrumentation are introduced in Chapter 2, followed by a description of the procedures for calibrating and analysing the data in Chapter 3. The results of the data analysis for ^{193}Bi and ^{191}Bi are presented in Chapter 4 and discussed in the context of TRS calculations, $B(M1)/B(E2)$ ratios, moments of inertia and level-energy systematics in Chapter 5. Finally, the results are summarised and future perspectives for further investigations of these nuclei are described in Chapter 6.

The results of the present work for ^{193}Bi and ^{191}Bi are reported in papers 1-3 and those for the lighter isotopes ^{189,187}Bi in paper 4. The results of studies of deformation and shape coexistence in other nuclei in the lead region are reviewed in papers 5-17. The author of this thesis has written papers 1-3 and actively participated in all of the experiments. The author has been partly responsible for the planning and completion of the experiment for ^{193}Bi, as well as for the Ge-detector units and construction of the target-position and focal-plane Ge-detector arrays used in the measurements.

1. **Gamma-ray Spectroscopy of ^{191,193}Bi**
   P. Nieminen, S. Juutinen, A.N. Andreyev, J.F.C. Cocks, O. Dorvaux, K. Eskola, P.T. Greenlees, K. Hauschild, K. Helariutta, M. Huyse, P.M. Jones, R. Julin, H. Kankaanpää, H. Kettunen, P. Kuusiniemi, Y. Le Coz. M. Leino T. Lönnroth, M. Muikku, P. Rahkila, A. Savelius, J. Uusitalo, N. Amzal, N.J. Hammond, C. Scholey and R. Wyss, to be published.

2. **Gamma-ray Spectroscopy of ^{191,193}Bi**
   P. Nieminen, J.F.C. Cocks, O. Dorvaux, P.T. Greenlees, K. Helariutta, P.M. Jones, R. Julin, S. Juutinen, H Kankaanpää, H. Kettunen, P. Kuusiniemi, M. Leino, M. Muikku, P. Rahkila, A. Savelius, J. Uusitalo, A.N. Andreyev, F. Becker, K. Eskola, K. Hauschild, M. Houry, M. Huyse, W. Korten, Y. Le Coz, R. Lucas, T. Lönnroth, Ch. Theisen, K. Van de Vel, P. Van Duppen, N. Amzal, P.A. Butler, N. Hammond, C. Scholey and R. Wyss, Acta Physica Polonica B **32**, 1019 (2001).

3. **Gamma-ray Spectroscopy of Very Neutron-Deficient Bi Isotopes**
P. Nieminen, S. Juutinen, J.F.C. Cocks, O. Dorvaux, T. Enqvist, T. Grahn, P.T. Greenlees, K. Helariutta, P.M. Jones, R. Julin, H. Kankaanpää, A. Keenan, H. Kettunen, P. Kuusiniemi, M. Leino, A.-P. Leppänen, M. Muikku, J. Pakarinen, P. Rahkila, A. Savelius, J. Uusitalo, E. Bouchez, A. Hürstel, K. Hauschild, W. Korten, Y. Le Coz, M. Rejmund, Ch. Theisen, N. Amzal, A.N. Andreyev, K. Eskola, N. Hammond, M. Huyse, T. Lönnroth, C. Scholey, P. Van Duppen and R. Wyss, Proceedings of Conference Frontiers of Nuclear Structure, Berkeley, California, USA, 29 July - 2 August 2002, edited by P. Fallon and R. Clark (AIP Conference proceedings **656**, Melville, New York, 2003), p. 63.

4. **Isomeric states in proton-unbound ^{187,189}Bi isotopes**
A. Hürstel, M. Rejmund, E. Bouchez, P.T. Greenlees, K. Hauschild, S. Juutinen, H. Kettunen, W. Korten, Y. Le Coz, P. Nieminen, Ch. Theisen, A.N. Andreyev, F. Becker, T. Enqvist, P.M. Jones, R. Julin, H. Kankaanpää, A. Keenan, P. Kuusiniemi, M. Leino, A.-P. Leppänen, M. Muikku, J. Pakarinen, P. Rahkila and J. Uusitalo, Eur. Phys. J. A **15**, 329 (2002).

5. **First observation of excited states in ^{197}At: the onset of deformation in neutron-deficient astatine nuclei**
M.B. Smith, R. Chapman, J.F.C. Cocks, O. Dorvaux, K. Helariutta, P.M. Jones, R. Julin, S. Juutinen, H. Kankaanpää, H. Kettunen, P. Kuusiniemi, Y. Le Coz, M. Leino, D.J. Middleton, M. Muikku, P. Nieminen, P. Rahkila, A. Savelius and K.-M. Spohr, Eur. Phys. J. A **5**, 43 (1999).

6. **Evidence of Multiple Shape-Coexistence in ^{188}Pb**
Y. Le Coz, F. Becker, H. Kankaanpää, W. Korten, E. Mergel, P.A. Butler, J.F.C. Cocks, O. Dorvaux, D. Hawcroft, K. Helariutta, R.-D. Herzberg, M. Houry, H. Hübel, P. Jones, R. Julin, S. Juutinen, H. Kettunen, P. Kuusiniemi, M. Leino, R. Lucas, M. Muikku, P. Nieminen, P. Rahkila, D. Rossbach, A. Savelius and Ch. Theisen, EPJdirect **A3**, 1 (1999).

7. **Microsecond isomers in ^{187}Tl and ^{188}Pb**
A.P. Byrne, A.M. Baxter, G.D. Dracoulis, S.M. Mullins, T. Kibédi, T.R. McGoram, K. Helariutta, J.F.C. Cocks, P. Jones, R. Julin, S. Juutinen, H. Kankaanpää, H. Kettunen, P. Kuusiniemi, M. Leino, M. Muikku, P. Nieminen, P. Rahkila and A. Savelius, Eur. Phys. J. A **7**, 41 (2000).

8. **Identification of the $13/2^+$ isomer in ^{199}At**
M. Lach, P. Bednarczyk, P.T. Greenlees, K. Helariutta, P. Jones, R. Julin, S. Juutinen, H. Kankaanpää, H. Kettunen, P. Kuusiniemi, M. Leino, W. Meszyński, M. Muikku, P. Nieminen, P. Rahkila, J. Styczeń and J. Uusitalo, Eur. Phys. J. A **9**, 307 (2000).

9. **First Observation of excited states in ^{182}Pb**
D.G. Jenkins, M. Muikku, P.T. Greenlees, K. Hauschild, K. Helariutta, P.M. Jones, R. Julin, S. Juutinen, H. Kankaanpää, N.S. Kelsall, H. Kettunen, P. Kuusiniemi, M. Leino, C.J. Moore, P. Nieminen, C.D. O'Leary, R.D. Page, P. Rahkila, W. Reviol, M.J. Taylor, J. Uusitalo and B. Wadsworth, Phys. Rev. C **62**, 021302(R) (2000).

10. **Shape coexistence in ^{183}Tl**
M. Muikku, P.T. Greenlees, K. Hauschild, K. Helariutta, D.G. Jenkins, P. Jones, R. Julin, S. Juutinen, H. Kankaanpää, N.S. Kelsall, H. Kettunen, P. Kuusiniemi, M. Leino, C. J. Moore, P. Nieminen, C.D. O'Leary, R.D. Page, P. Rahkila, W. Reviol, M.J. Taylor, J. Uusitalo and R. Wadsworth, Phys. Rev. C **64**, 044308 (2001).

11. **Identification of low-lying proton-based intruder states in $^{189-193}$Pb**
K. Van de Vel, A.N. Andreyev, M. Huyse, P. Van Duppen, J.F.C. Cocks, O. Dorvaux, P.T. Greenlees, K. Helariutta, P. Jones, R. Julin, S. Juutinen, H. Kettunen, P. Kuusiniemi, M. Leino, M. Muikku, P. Nieminen, K. Eskola and R. Wyss, Phys. Rev. C **65**, 064301 (2002).

12. **In-beam and α-decay spectroscopy of ^{191}Po and evidence for triple shape coexistence at low energy in the daughter nucleus ^{187}Pb**
A.N. Andreyev, M. Huyse, K. Van de Vel, P. Van Duppen, O. Dorvaux, P. Greenlees, K. Helariutta, P. Jones, R. Julin, S. Juutinen, H. Kettunen, P. Kuusiniemi, M. Leino, M. Muikku, P. Nieminen, P. Rahkila, J. Uusitalo, R. Wyss, K. Hauschild and Y. Le Coz, Phys. Rev. C **66**, 014313 (2002).

13. **Confirmation of triple shape coexistence in ^{179}Hg: Focal plane spectroscopy of the α decay of ^{183}Pb**
D.G. Jenkins, A.N. Andreyev, R.D. Page, M.P. Carpenter, R.V.F. Janssens, C.J. Lister, F.G. Kondev, T. Enqvist, P.T. Greenlees, P.M. Jones, R. Julin, S. Juutinen, H. Kettunen, P. Kuusiniemi, M. Leino, A.-P. Leppänen, P. Nieminen, J. Pakarinen, P. Rahkila, J. Uusitalo, C.D. O'Leary, P. Raddon, A. Simons, R. Wadsworth and D.T. Joss, Phys. Rev. C **66**, 011301(R) (2002).

14. **First observation of gamma-rays from the proton emitter ^{171}Au**
T. Bäck, B. Cederwall, K. Lagergren, R. Wyss, A. Johnson, D. Karlgren, P. Greenlees, D. Jenkins, P. Jones, D.T. Joss, R. Julin, S. Juutinen, A. Keenen, H. Kettunen, P. Kuusiniemi, M. Leino, A.-P. Leppänen, M. Muikku, P. Nieminen, J. Pakarinen, P. Rahkila and J. Uusitalo, Eur. Phys. J. A **16**, 489 (2003).

15. **Spectroscopy of the neutron-deficient nuclide ^{171}Pt**
T. Bäck, B. Cederwall, K. Lagergren, R. Wyss, A. Johnson, P. Greenlees, D. Jenkins, P. Jones, D.T. Joss, R. Julin, S. Juutinen, A. Keenan, H. Kettunen, P. Kuusiniemi, M. Leino, A.-P. Leppänen, M. Muikku, P. Nieminen, J. Pakarinen, P. Rahkila and J. Uusitalo, Eur. Phys. J. A **17**, 1 (2003).

16. **In-beam γ-ray spectroscopy of ^{190}Po: First observation of a low-lying prolate band in Po isotopes**
K. Van de Vel, A.N. Andreyev, R.D. Page, H. Kettunen, P.T. Greenlees, P. Jones, R. Julin, S. Juutinen, H. Kankaanpää, A. Keenan, P. Kuusiniemi, M. Leino, M. Muikku, P. Nieminen, P. Rahkila, J. Uusitalo, K. Eskola, A. Hürstel, M. Huyse, Y. Le Coz, M.B. Smith, P. Van Duppen and R. Wyss, Eur. Phys. J. A **17**, 167 (2003).

17. **Shape isomerism and spectroscopy of ^{177}Hg**
A. Melerangi, D. Appelbe, R.D. Page, H.J. Boardman, P.T. Greenlees, P. Jones, D.T. Joss, R. Julin, S. Juutinen, H. Kettunen, P. Kuusiniemi, M. Leino, M.H. Muikku, P. Nieminen, J. Pakarinen, P. Rahkila and J. Simpson, Phys. Rev. C **68**, 041301(R) (2003).

2 Experimental methods and instrumentation

Apart from the traditional heavy-ion induced fusion-evaporation reactions, the very neutron-deficient nuclei in the lead region may be accessed via for example high-energy proton-induced spallation reactions [And02a]. However, this method is only suited for decay studies as the immense hostility of the target area does not allow any in-beam spectroscopic measurements. The complete fusion reactions provide a more selective method to produce the nuclei of interest in their excited states and naturally lead to the neutron-deficient region since the valley of β-stability curves towards larger neutron numbers with increasing proton number. However, when approaching the proton drip line, production cross sections of these nuclei rapidly decrease being typically below a hundred nanobarns for the last known isotope of a given element in the $Z = 82$ region. The dominating decay mode in this region is α-particle emission with properties that are usually studied by implanting the separated fusion-evaporation residues into a particle detector and observing the subsequent characteristic decay. The identification of new α activities is normally based on the observation of α-decay chains leading to known nuclei.

In α-decay studies, the low production cross sections can, at least in principle, be compensated by extending the time of the measurement and by increasing the beam current. However, when studying a nucleus via in-beam γ-ray detection, the situation is different. The total counting rate of prompt γ rays following all reactions occurring in the target is in the present work roughly 10^5 times larger than that of the γ rays belonging to the nucleus of interest. Since a γ ray does not possess any characteristic property directly identifying its nucleus of origin, an efficient method to isolate the γ rays of interest from the background radiation is required. In the present work, the separation is achieved by using an experimental apparatus which combines a recoil separator and Ge-detector arrays with special analysis methods. In the recoil-decay tagging (RDT) technique, recoil implantations observed in the focal-plane silicon detector are identified according to their characteristic α decay, whereas in the recoil gating method, γ rays associated with all observed recoils are accepted. In the isomer tagging analysis, γ rays de-exciting an isomer are used to distinguish prompt γ-ray transitions feeding the isomeric state. Similar methods can be used when, instead of γ rays, conversion electrons are measured at the target position.

The dynamics of fusion-evaporation reactions are discussed in the first part of this chapter. A review of the detector arrangements employed at the target position, the

recoil separator RITU and the focal-plane detector system is followed by an introduction to the signal processing electronics and data acquisition system. The chapter is concluded by assessing the performance of the system for studies of nuclear states with various halflives.

2.1 Heavy-ion induced fusion-evaporation reactions

In order to fuse the beam and target nuclei, the kinetic energy of the incident beam particle has to be high enough (typically $\sim$ 5 MeV per nucleon) to overcome the Coulomb barrier. The excitation energy of the compound system is the sum of the kinetic energy of the collision in the centre of mass frame and the reaction Q value. The upper limit for the energy which can be brought into a compound nucleus in the mass region studied in the present work is set by fission, whose probability rapidly increases with increasing excitation energy. The angular momentum transferred into the system increases as the velocity of the beam is increased, or when heavier projectiles are used. If the compound nucleus finally holds together, the excitation energy is evenly distributed among the nucleons within about 10^{-16} s and thermodynamical equilibrium occurs. However, as the total energy and angular momentum are conserved, the de-excitation of a compound system at a given excitation energy and angular momentum is independent of its formation.

The de-excitation proceeds via the evaporation of a combination of neutrons, protons and heavier charged particles (mainly α particles in this mass region). Neutron evaporation dominates as Z increases and when the compound nucleus lies far away from the proton drip line. When approaching the drip line, the probability to evaporate charged particles increases due to increased Coulomb repulsion. When the excitation energy above the yrast line is less than any of the particle binding energies ($\sim$ 8 MeV), the remaining energy is released by γ-ray emission. At excitation energies just below the particle evaporation limit, the level density is high and the feeding is fragmented, hence distinct γ rays cannot be measured. In contrast, the energy levels at low excitation energies near the yrast line are clearly separated from each other and as a major part of the feeding finally populates these states, discrete γ-ray transitions can be observed.

Since the angular momentum brought into the compound system also depends on the mass of the beam particle, the choice of the beam-target combination effects the feeding of various states in the residual nucleus. The bombardment with heavy projectiles preferentially populates high-spin states near the yrast line, whereas lighter beams, to some extent, allow the feeding of non-yrast states at low spin. Thus, the most efficient method to study the low-lying non-collective states in a nucleus would be a light-ion induced reaction, for example of the type (α,2n). However, such reactions are

beyond the scope of the present work since the candidate target nuclei are radioactive with halflives of the order of minutes (or shorter).

As the recoils are to be separated in flight after their formation, thin targets must be used. Therefore, the Ge-detector setup which is employed to measure the emitted prompt radiation has to be located in such a way that γ rays originating from the flying recoils are emitted in the field of vision of the detectors. The natural assumption would be to place the detectors facing the target and this turns out to be a correct choice when considering the time scale of the de-excitation process. A typical velocity of the recoiling nuclei of interest in the present work was $\sim$2% of the speed of light, corresponding to 6 mm/ns. If there are no isomeric states along the de-excitation path, the process typically occurs faster than in 10^{-10} s. Thus, the recoiling nucleus reaches its ground state within a distance of less than one millimeter from the point where it was formed and the emitted radiation is well covered by the detectors.

Another requirement for the reactions used in the present work is set by the angular acceptance of the recoil separator. The cone of the recoil distribution must be sufficiently narrow so that the magnetic field of the separating device catches the maximum possible number of nuclei recoiling from the target. The acceptance of the gas-filled recoil separator RITU has been measured to be 8 msr using an α source [Uus03]. This has proved to be adequate to accommodate the forward-peaking distribution of the fusion-evaporation residues. In addition, the narrow recoil cone makes it possible to define the angle between the recoil direction and the Ge detectors, thereby allowing Doppler shift corrections to be determined for the measured γ-ray energies. Moreover, the kinetic energy received by the recoil has to be large enough to overcome the stopping it experiences in the helium filling-gas and multiwire proportional avalanche counter on the way to the separator focal-plane. This requirement limits the mass asymmetry between the reaction partners.

2.2 Gamma-ray detectors and the Jurosphere II array

Germanium detectors provide the essential benefit of good energy resolution in γ-ray detection compared to the formerly widely used scintillator detectors. The energies of the γ rays following the de-excitation of an excited state in an $A \sim 200$ nucleus usually range from 100 keV to 1.5 MeV. In this region, the energy resolution of a Ge detector typically falls between 1.5 and 3 keV (FWHM), whereas for example a bismuth germanate (BGO) scintillator can only reach a resolution of $\sim$20% of the transition energy.

On the other hand, Ge detectors suffer from poorer detection efficiency compared to the most efficient scintillator materials. In a standard calibration procedure, the absolute efficiency of a Ge detector to observe a 1332 keV γ ray is given as a percentage of the value of 1.2×10^{-3} obtained for a cylindrical NaI(Tl) scintillator (diameter 76 mm, height 76 mm, active volume $\sim$340 cm^3). The measurement is made by using a calibrated ^{60}Co source positioned on the symmetry axis of the detector at a distance of 25 cm. The efficiencies of the various types of Ge detectors used in the present work, either measured locally or extracted from manufacturer specifications, are given in Table 2.1. Taking into account the active detection volumes, the difference between the Ge and NaI(Tl) crystals is rather small but the efficiency of a BGO crystal is roughly five times larger than that of an equal-size NaI(Tl) detector [Kno89].

Table 2.1: Active volumes and measured efficiencies of various types of Ge detectors used in the present work.

Detector Type	Reference	Crystal volume (cm^3)	Efficiency (%)
TESSA	[Nol85]	100-120	20-25
Nordball	[Mos89]	150-200	30-45
Eurogam Phase I	[Bea92]	250-300	50-75

Besides the better detection efficiency, the other advantage scintillators have over the Ge detectors is their fast signal output and therefore better time resolution. Modern Ge-detector modules, like the Eurogam Phase I-type shown in Figure 2.1 are designed to use the best properties of each type of detector. Thermal noise is suppressed by mounting the Ge crystal inside a cryostat and cooling it down to liquid nitrogen temperature. The interactions of photons with Ge ($Z = 32$) are dominated by Compton scattering at γ-ray energies from 150 keV to 8 MeV. As the size of a Ge crystal is finite, an energetic γ ray does not necessarily deposit all of its energy into the active detection volume but part of the scattered γ rays can escape from the detector. These events are observed in the BGO anti-Compton shield surrounding the Ge crystal and the signals are amplified using the photomultiplier tubes. By using the coincident events in the BGO shield to veto the observed γ rays, the Compton background in the γ-ray energy spectrum is reduced so that during the calibration procedure, peak-to-total (P/T) ratios of up to 50% for single detectors can be achieved. The heavy-metal collimator is mounted in front of the BGO crystal to prevent γ rays from directly hitting the shield and it also defines the focus point of the Ge detector.

To attain sufficient detection efficiency and to observe γ-γ coincidences, several Ge-detector units were mounted in a frame surrounding the target. The Jurosphere II Ge-detector array in its full composition holds 15 Eurogam Phase I-, five Nordball- and seven TESSA-type Compton-suppressed Ge detectors. The Eurogam detectors were installed at angles of 133.6° and 157.6° and the TESSA and Nordball detectors

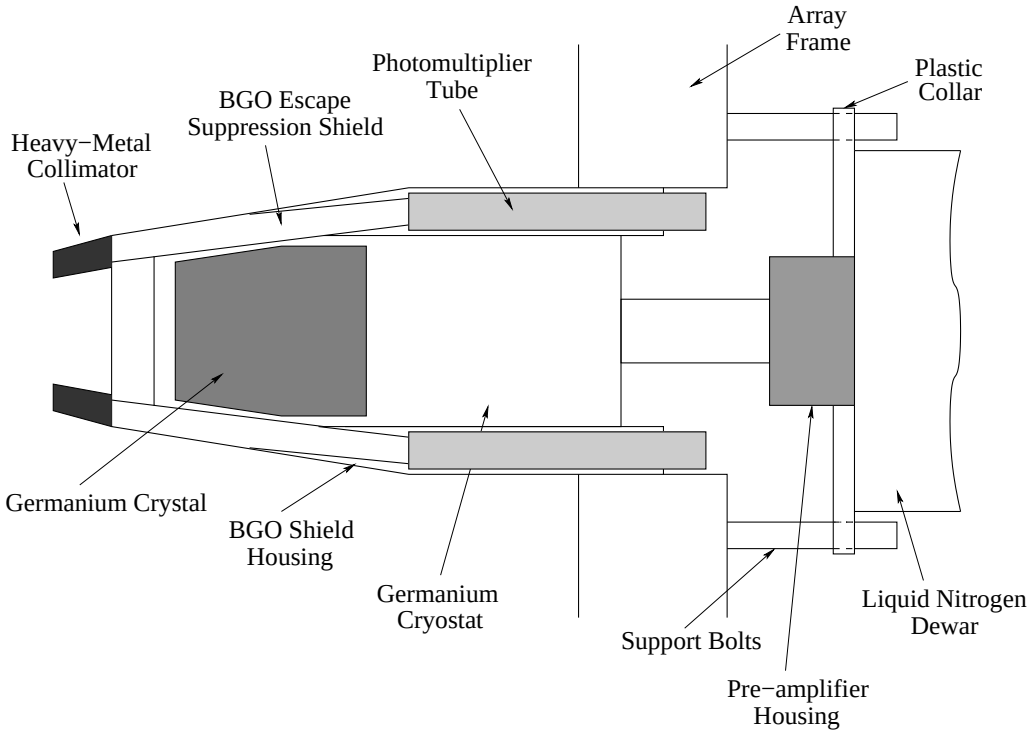

Figure 2.1: Eurogam Phase I detector module composed of a Ge detector and a BGO escape suppression shield [Bea92].

at angles of 63°, 79.0° and 101.0° with respect to the beam direction. The Eurogam detectors were at a distance of 20.5 cm, the Nordball detectors and five of the TESSA detectors at 20 cm and the remaining two TESSA units at 22 cm from the target. Absorbers, consisting of a 0.25 mm thick layer of tin and a 0.5 mm thick layer of copper, were positioned in front of each detector to reduce the counting rate due to X rays. A schematic drawing of the experimental setup, including the RITU separator and four of the focal-plane Ge detectors is shown in Figure 2.2. The fifth detector was placed facing the back of the focal-plane chamber.

Internal conversion competes with γ-ray emission in the de-excitation process of a nucleus with increasing probability as Z increases and as the transition energy decreases, hence providing a complementary method to obtain experimental information on its excited states. Electron-spectroscopic measurements for mainly the superheavy elements have been realised at JYFL using the redesigned [Kan03] electron spectrometer SACRED (Solenoid and Array for ConveRsion Electron Detection) [But96] which was employed at the RITU recoil separator. In the bismuth isotopes, internal conversion dominates for E2, M1 and M2 transitions with energies below 160, 230, and 360 keV, respectively [Ros78]. Since the conversion probabilities for transitions having different multipolarities vary significantly from each other, electron spectroscopy could be used to determine the character of the observed transitions. It would be also very interest-

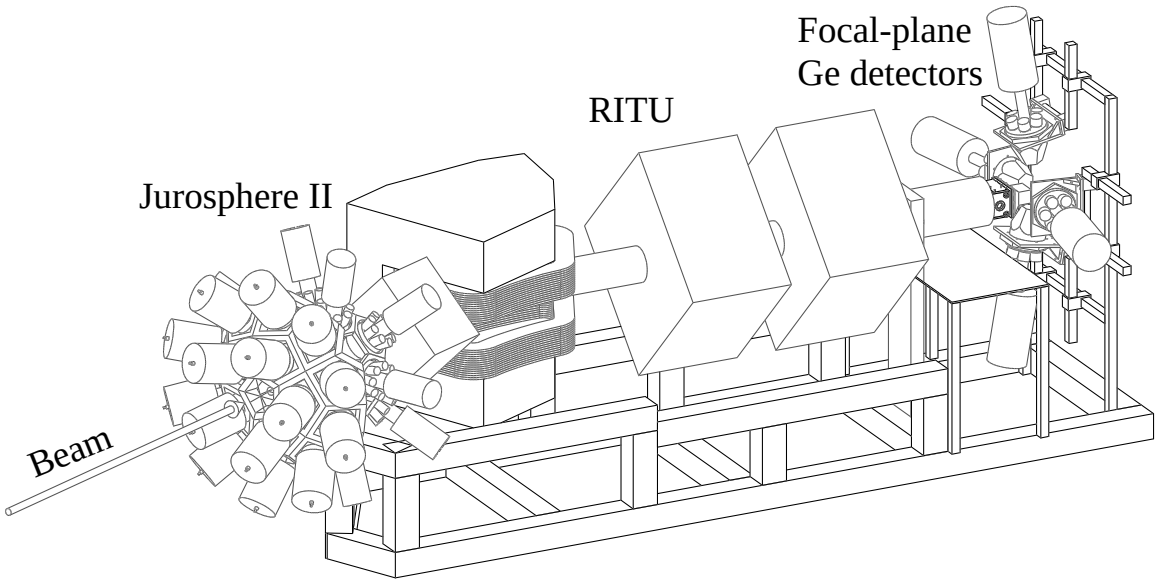

Figure 2.2: The Jurosphere II Ge-detector array at the target position and an array of Ge detectors at the focal plane of the RITU gas-filled separator.

ing to measure conversion electrons from low-energy transitions which usually remain unobserved in the in-beam γ-ray measurements. However, in the nuclei studied in the present work, these transitions are in many cases connected to isomeric states and due to the half-life cannot be observed with the SACRED setup at the target position. Moreover, the practical lower limit of the observable electron energy is typically 40 keV.

2.3 Gas-filled recoil separator RITU

The gas-filled recoil separator RITU (Recoil Ion Transport Unit) [Lei95a, Lei95b] provides the required separation of the recoiling nuclei from the primary beam and fission fragments. The separator is a combination of a separating dipole (D) magnet and focusing quadrupole (Q) magnets arranged as QDQQ (see Figure 2.3), in contrast to the standard DQQ design. The placement of the target in front of the dipole provides better suppression of the primary beam, whereas the additional quadrupole better matches the recoil distribution into the dipole magnet acceptance.

The volume of the separator is filled with dilute gas, in this case helium, to achieve better recoil transmission compared to the vacuum-mode devices. The working principle of a gas-filled separator is based on collisions of the reaction products with the filling gas atoms which results in an average charge state q_{ave} for the ions. Thus, the transmission efficiency is remarkably increased when the initially broad charge-state

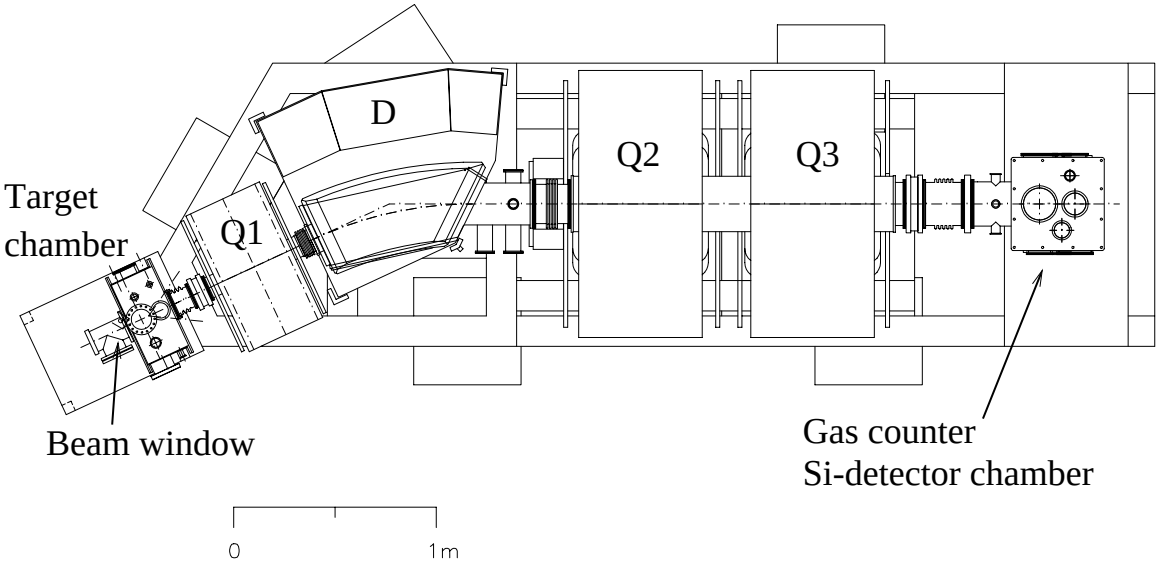

Figure 2.3: Scheme of the gas-filled recoil separator RITU. The target and detector chambers illustrated are as used in stand-alone decay experiments, when Ge-detector arrays are present, small chambers are installed.

distribution is suppressed to the average value which is then focused at the focal plane of the separator. The gas volume is separated from the beam line vacuum with a thin window of either nickel or carbon, in the present experiments a carbon window of 50 μg/cm^2 thickness was used. An estimate for the average charge state of an ion moving with velocity v can be derived from the Thomas-Fermi model of the atom [Boh41], giving

$$q_{ave} \approx \frac{v}{v_0} Z^{1/3}, \tag{2.1}$$

where v_0 is the Bohr velocity 2.19×10^6 m/s. This approximation is valid in the range of $1 < v/v_0 < Z^{2/3}$. In this work, the bismuth ($Z = 83$) nuclei gained a velocity of $\sim$2% of the speed of light giving $v/v_0 \sim 2.7$ which is well below the value $Z^{2/3} \sim 19$. Thus, the magnetic rigidity $B\rho$ for an ion (A,Z) moving in a homogeneous dipole field with momentum mv can be written as [Ghi88]

$$B\rho \approx \frac{mv}{q_{ave}} \approx \frac{mv_0}{Z^{1/3}} \approx 0.0227 \frac{A}{Z^{1/3}} \text{ [Tm]}. \tag{2.2}$$

As seen from Equation 2.2, the bending radius at a given magnetic field depends only on the atomic and mass number of the recoil and hence, a gas-filled recoil separator can be considered as a mass separator. However, the $B\rho$ resolution is rather poor, typically of the order of 10% for RITU [Lei95b]. This level of separation is sufficient to suppress the full-energy primary beam from non-symmetric reactions, as in the present work. However it is not enough to provide sole mass selection of the fusion-evaporation products and furthermore, scattered target atoms and beam particles may also be transported to the focal plane.

During an experiment, the performance of the combined system of the RITU separator and a target-position Ge-detector array can be optimised by selecting a suitable filling-gas pressure. It has to be sufficiently high to achieve charge-state focusing and low enough so that multiple scattering does not spread the recoil distribution so that its optical size exceeds that of the focal-plane detector. Concerning the detection of γ rays, counting rates in the Ge detectors increase significantly as gas pressure increases. These effects are illustrated in Figure 2.4 where the yield of ^{202}Rn α particles from the ^{40}Ar $+^{166}$ Er $\rightarrow^{206}$ Rn* reaction and the total singles counting rate in one of the Ge detectors are plotted as a function of the RITU filling-gas pressure [Uus03]. The α-particle yield reaches its maximum value at a pressure of 0.6 mbar and remains constant to the last measurement point at 1.6 mbar. A decrease of the separator transmission due to multiple scattering would be expected at gas pressures higher than roughly 5 mbar [Arm71]. The total counting rate in the Ge detector comprises γ rays originating from the interaction of the beam with the target, beam window and filling gas together with a random background component. The counting rate from the target may be further divided into the contributions of the target material itself and that of the frame. As multiple scattering in the filling gas also spreads the distribution of the primary beam, an increasing portion of the projectiles may hit the frame as the gas pressure increases, thereby resulting in higher γ-ray background. However, this effect is presumably small compared to the background resulting from all interactions with the filling-gas atoms, which are assigned to be the main source of the increased counting rate at high gas pressures.

2.4 Focal-plane setup

On their way to the RITU focal plane, the separated particles pass through a multi-wire proportional avalanche counter (MWPAC). The electrodes of this in-house built [Ket03a] device are confined between two 100 μg/cm^2 Mylar foils and the detector volume is filled with isobutane gas of approximately 3 mbar in pressure. The positive voltage that is applied to the central electrode creates very strong electric fields around the thin wires. In flight, the separated particles ionise the filling gas atoms producing free electrons which are accelerated towards the electrode, further ionising the gas atoms and resulting in an avalanche of electrons to the central electrode. The collected charge is roughly proportional to the energy loss of the particle within the gas volume and hence, the identification of heavier recoils from the background of lighter scattered beam particles is possible. However, the more important application for the gas counter in the present work is to distinguish between α-decay events and separated particles which are detected in the focal-plane Si detector. This is achieved by requiring an anti-coincidence between a signal from the gas counter and an observed α decay.

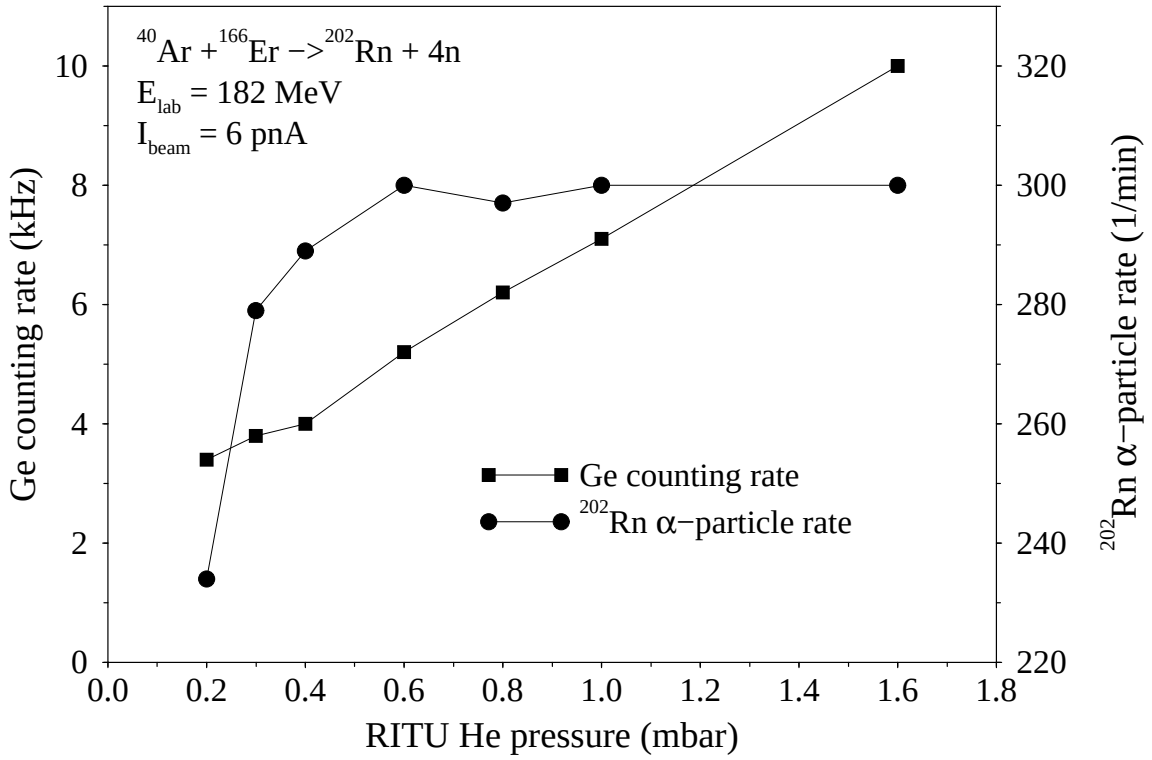

Figure 2.4: The yield of ^{202}Rn α particles from the ^{40}Ar $+^{166}$ Er $\rightarrow^{206}$ Rn* reaction (filled circles) together with the total singles counting rate in one of the Ge detectors (filled squares) [Uus03].

The 300 μm thick Si detector with an area of 80 mm (horizontal) $\times$ 35 mm (vertical) was used for the observation of both recoil implantations and α decays. The detector is divided into 16 strips, each being 5 mm wide and position sensitive in the vertical direction. Position sensitivity is achieved by coating the detector surface with a resistive layer. The amplitude of the outcoming energy signal from one end of a strip is proportional to the distance between the interaction point and the edge of the strip. Thus, the vertical position and the energy of the observed event can be reconstructed by combining the signals received from both ends.

The average position resolution in the Si-detector strips was $\sim$450 μm in the ^{191}Bi experiment (see Figure 3.1, Section 3.2.1), thereby dividing a single strip into approximately 80 separate pixels. Having 16 strips, the total number of pixels in the whole detector is then roughly 1300. In order to correlate the observed α decay with the preceding recoil implantation in both position and time, the implantation rate has to be low enough so that the time interval between successive recoil events within one pixel is longer than typically three times the α-decay half-life. This constraint allows the correlation of a recoil with 87.5% of the α-decays of interest while the remaining 12.5% are compromised due to the increased probability of chance correlations. As

the maximum recoil rate allowed per pixel is known, the maximum total counting rate of recoils in the Si detector can be obtained by multiplying the value for a single pixel with the total number of pixels in the detector. However, since the implantation events are not evenly distributed over the detector surface but concentrate in the central part, the calculated value of 1300 for the number of pixels is an overestimation in experimental conditions. Instead, an effective value of about 200 has proved to be satisfactory.

The Ge-detector array employed at the focal plane for the observation of isomeric γ rays consisted of 3 Nordball- and 2 TESSA-type Compton-suppressed detectors, mounted in close geometry around the Si-detector chamber. Unlike the detectors in the Jurosphere II array, no collimators or absorbers were used in front of the focal-plane Ge detectors. The absorbers were discarded to allow the observation of low-energy γ rays and the collimators were removed to gain a larger acceptance for γ rays emitted from all over the Si-detector surface.

2.5 Electronics and data acquisition

The experimental information collected during a measurement is embedded in the analogue signals which are received from the outputs of all of the detectors in the setup. The two most important parameters are the energy of the observed radiation and a timing signal for the interaction. These signals are processed using standard NIM electronics, digitised and fed into the acquisition system to be finally written onto a magnetic tape for an off-line analysis.

2.5.1 Si strip detector and gas counter

The signals from the focal-plane Si detector are read out from both ends of each strip using charge-sensitive preamplifiers. As the amplitude of each of these signals is proportional to the vertical distance between the interaction point and the edge of the detector, the total energy of an event can be reconstructed by summing the two signals. The so-called top and bottom signals together with the total-energy information are amplified using linear amplifiers. Since the energy deposited into the detector may be significantly higher for recoils than for decay events, two amplification channels are available. The usage of low amplification for implantations and high amplification for the observed decays then results in a high-resolution α-particle energy spectrum.

Since each strip provides six output signals (top position, bottom position and sum energy for both high and low amplification), multiplexers are used in order to reduce

the number of analogue-to-digital converters (ADC's) required. To determine the horizontal position of the interaction, *i.e.* the number of the active strip, the sum energy of the observed event is fed from the linear amplifier into a pattern trigger unit. The logic output from the pattern trigger carries the information on the strip number and is used to strobe the corresponding channel in all of the multiplexers. Therefore, signals from a single strip at a time are read out and the next event in the Si detector can be recorded only after ∼50 μs which is the time required for the readout stage and data processing. However, this dead time was acceptable since the total processing time of one event is small compared with the maximum counting rate (∼300 Hz in the ^{193}Bi experiment)

Like the Si detector, the gas counter also has two amplification channels, one with low and the other with high gain. The energy signals from both channels are fed into the acquisition system through an ADC. Timing information is also extracted.

2.5.2 Ge detectors

A block diagram of the measurement electronics used for the Ge detectors in the Jurosphere II array is illustrated in Figure 2.5. This scheme also presents the feeding of the aforementioned Si-and gas-detector signals into the acquisition system. A Ge-detector preamplifier has two identical outputs, one of which is used for obtaining the energy of an event while the other provides the timing information. The energy signal is fed into a linear amplifier (AMP) from which the unipolar output is taken to an ADC. To validate the energy information and feed it into the acquisition system, a timing signal is required in the 'adc gate' input of the ADC. This time gate is present only if the measured photon energy has not been observed to be in coincidence with a signal from the anti-Compton shield or shifted by pile-up.

Following the scheme for the Eurogam detector modules (Ge 11-25 and BGO 11-25 in Figure 2.5), the timing signal from the Ge detector is fed into a timing filter amplifier (TFA) where it is amplified and reshaped for the input of a constant fraction discriminator (CFD). In principle, the CFD should eliminate time walk due to the γ-ray energy but in practice fluctuations are observed especially for low-energy γ rays. The logic output from the CFD is taken into a coincidence unit (COIN("veto")). A timing signal from the BGO shield is amplified and shaped to be fed into its own CFD unit, whose output is in turn used as a veto in the COIN("veto") unit thus excluding the Compton-scattered events.

The linear amplifier gives out a 'busy' signal which indicates that the processing of energy information is ongoing. This signal is inverted (TTL TO NIM) and also fed into the COIN("veto") unit. In setting up the system, the temporal overlap between the output from the Ge CFD and the busy signal is adjusted so that the timing

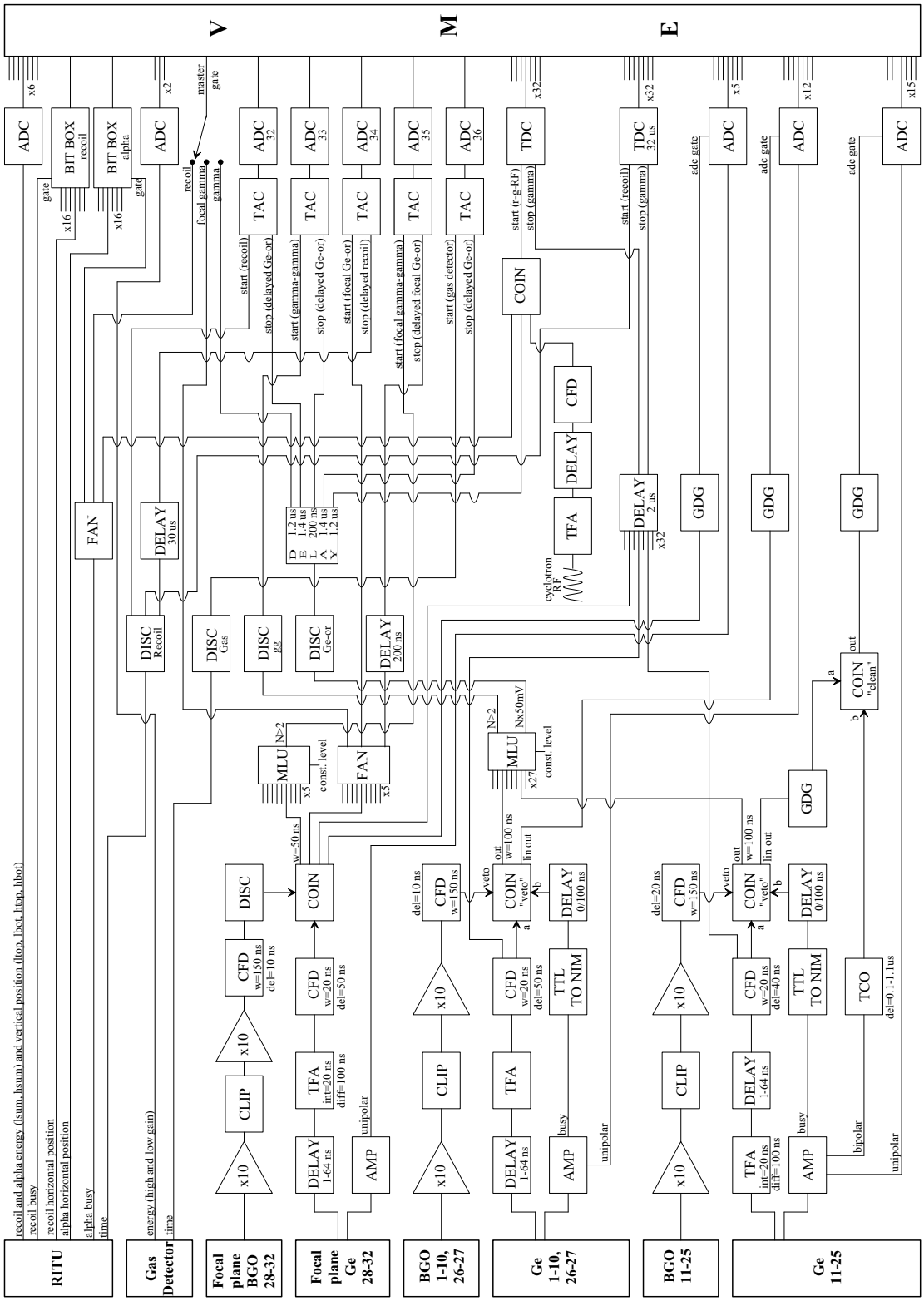

Figure 2.5: A block diagram of measurement electronics used for the Jurosphere II + RITU setup.

signal corresponding to the first event arrives just prior to the busy signal. A further requirement to validate the timing signal for an event is that there are no other CFD signals following the first one before the linear amplifier is free again. To achieve this, two steps are required. A timing signal which arrives from the CFD while the amplifier is busy is automatically rejected. However, the energy of this piled-up event is associated with the first time gate and has to be discarded in the next stage.

The logic output from the COIN("veto") unit is stretched in a gate and delay generator (GDG) and fed into a second coincidence unit (COIN("clean")). A signal from the bipolar output of the linear amplifier is taken to the input of a single-channel analyser where the energy window is set wide open and which is operating in the cross-over mode (TCO). The outcoming logic signal from the TCO corresponds to the zero crossing point of the bipolar energy signal and it is fed to the COIN("clean") unit. In the case of pile-up, the duration of the energy signal is longer than for an event from a single interaction and the delay for it to reach the zero crossing generates a delay in the TCO output. This signal in turn is in anti-coincidence with that from the COIN("veto") unit and no output from the COIN("clean") unit is received. The energy of an observed γ ray, which is not associated with pile-up or Compton scattering out of the detector, is validated by a logic output from the COIN("clean") unit. This signal is modified in a GDG and finally used to gate the ADC.

For the Nordball and TESSA detectors (Ge 1-10, 26-27 and BGO 1-10, 26-27 in Figure 2.5), only the first step of the pile-up rejection is performed due to the limited availability of electronics units. The choice to instrument the Eurogam detectors for the whole two-step procedure is justified by the fact that they have the highest counting rates and thus the largest probabilities for observing two or more γ rays closely spaced in time. For the Ge detectors at the focal plane (Ge 28-32 and BGO 28-32 in Figure 2.5), only Compton-scattered events are suppressed.

To facilitate the analysis, some further timing relations between the separate detectors are constructed in the hardware. The coincidence of two or more γ rays (Ge-AND) within ~ 200 ns is recorded using a multiplicity logic unit (MLU). The Ge-AND signal for prompt (or delayed) events is fed into the start input of a time-to-amplitude converter (TAC) unit for which the stop signal is provided by the time of the observation of a prompt (or delayed) single γ ray (Ge-OR). The amplitude of the analogue pulse received from the TAC output corresponds to the time difference between the start and stop inputs and this signal is digitised in an ADC. The Ge-OR signal for prompt γ rays is obtained from the MLU unit while the corresponding information for delayed γ rays is created in a linear fan in/fan out (FAN) unit. Apart from the mutual timing of γ rays, the time difference between the implantation of a recoil and the observation of a prompt or delayed γ ray (Ge-OR) is recorded by using a TAC unit. Moreover, the same time differences are recorded individually for each prompt or delayed γ ray using a time-to-digital converter (TDC). A further requirement is to distinguish prompt γ

rays associated with the beam pulse from random background events. This is realised by creating a time stamp for the cyclotron radio frequency (RF) with a combination of TFA and CFD units and by extracting the time difference between the RF and the observation of each γ ray using another TDC unit. In addition, the time between the Ge-OR signal for prompt γ rays and an event in the gas detector is extracted.

2.5.3 Data acquisition

The TARDIS data acquisition system comprises a set of VME crates with integrated electronics together with a control workstation [Jon95]. All the collected data are divided into events. Each event is initiated by a 'master trigger' which in the present experiments is a signal from the Si-strip detector, *i.e.* the time stamp for a recoil implantation or an α decay. In practice, the gate signal is exported from a common output in the pattern trigger unit for the high amplification channels. While the master gate is open, the information read in by all of the ADC's passes through a read-out controller and is temporarily stored in the memory of an event builder. The separate events are then gathered into blocks of events which, when completed, are converted to Eurogam data format [Cre91] and sent out to the tape server to be finally written onto a magnetic tape. In addition to storing data on tape, online spectra are required in the setting-up process of the various detectors, optimising the performance of the RITU separator and monitoring the incoming data during the experiment. These conditions are met by sorting the event data on a real-time basis and by examining the singles spectra generated by an on-board histogramming memory.

As the signals from the Ge-detector array at the target position and the gas counter actually arrive prior to the focal-plane trigger (see Figure 2.6 (a)), they are delayed in such a way that an overlap with the master gate is obtained in the acquisition system. The master gate is open for 32 μs thus setting the maximum time for recording signals from various detectors into a single event. However, the full time window is employed only for the detection of isomeric γ rays at the focal plane while the other signals are restricted inside shorter time intervals, as sketched out in Figure 2.6 (b). The limit of 1 μs for collecting prompt γ rays settles around the time of the beam pulse hitting the target, determined by the cyclotron RF. The stage when the data are processed and written onto the tape extends the total time elapsed for one event up to 50 μs, after which the system is ready again to accept a new master gate and read in new data.

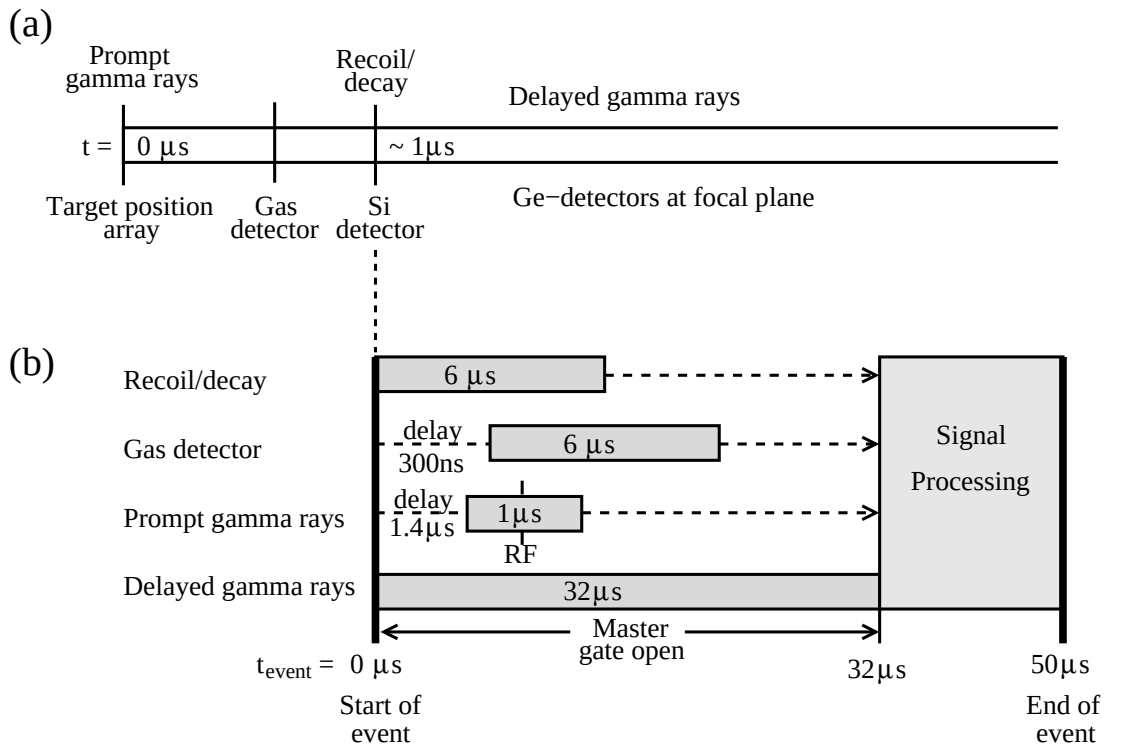

Figure 2.6: (a) Time order of signals from various detectors in the present experimental setup. (b) Time windows for data collection into a single event.

2.6 Performance of the system - suitable halflives

In the present system, the basic requirement for studying the structure of a nucleus by making use of the observation of its α decay, is a half-life which is long enough so that the residue survives the flight through the separator until it is implanted into the focal-plane Si detector. This condition is fulfilled in the present work since the α-decay halflives in the very neutron-deficient lead region typically range from milliseconds up to seconds, whereas the flight time of the recoils is of the order of 1 μs. In the RDT method, the upper limit for the decay half-life can be derived from the conditions for a successful correlation procedure. The nucleus of interest has to be so short-lived that the implantation rate (adjusted as described in Section 2.4) produces sufficient statistics for the analysis. The ^{191,193}Bi nuclei studied in the present work are close to or even partly above this limit. Therefore, the cleanness of the correlation analysis linking the observed α decays to the preceding recoils cannot be guaranteed for all the α-decaying states and other methods may have to be used. In this sense, the correlation techniques are more feasible in the study of even lighter bismuth isotopes as the halflives become shorter. However, the counting statistics are then hampered by decreasing production cross sections.

Isomeric states that de-excite via γ-ray emission typically have much shorter halflives than α-decaying states. For example, the measured values for the observed isomers in the core nuclei ^{192}Pb [Lag91] and ^{190}Pb [Dra98] for the ^{193}Bi and ^{191}Bi isotopes, respectively, range from tens of nanoseconds up to tens of microseconds. In experiments of the present type, prompt γ-ray transitions feeding an isomeric state are observed at the target position while the de-exciting γ rays can be detected either in the target-position array or at the focal plane. The major disadvantage of the present setup derives from the fact that all γ rays emitted during the flight of the recoils through the separator down to its focal plane remain unobserved.

Even though γ rays de-exciting a nanosecond isomer may be detected at the target position, it is very difficult to distinguish these transitions from the genuinely prompt events. In principle, the only possible method in the present system to extract a half-life of the order of a nanosecond would be an observation of a centroid shift in the spectrum of time differences between the cyclotron RF and the time of the observation of the γ ray. The centroid shift method has successfully been applied for example in a backed-target experiment for the stable nucleus ^{110}Cd [Juu94]. In this measurement, the reference was set by a cascade of truly prompt transitions and the halflives of sub-nanosecond isomers were determined with an accuracy of around 25% and for a 3.5 ns isomer, an error of 15% was given. However, in order to reliably identify this minor effect in the present experiments, statistics of orders of magnitude higher than ever available for these very neutron-deficient nuclei would be required. Moreover, the RF signal does not provide an exact time stamp for the interaction between the beam particle and target atom since the cyclotron beam pulses have a time spread of a few nanoseconds. As thin targets are used, the observation of γ rays de-exciting isomeric states with halflives of a few nanoseconds is further limited by the fact that the flying recoils escape from the centre of the target-position array. One possibility to infer the presence of a nanosecond isomer would be an intensity imbalance of γ rays feeding and depopulating an excited state. However, even if this effect was observed, the properties of the isomeric state cannot be determined. For example, an isomer with $t_{1/2} \approx 20$ ns was observed in ^{190}Pb using pulsed beams and backed targets [Dra98] while a study of the same nucleus using the setup described in the present work only revealed the de-exciting transition as having very low intensity [Jon99].

The determination of the properties of an isomer in practice requires the measurement of the de-exciting γ rays in the focal-plane Ge detectors. The lower limit for the observable half-life naturally depends on the number of recoils which reach the focal plane in the isomeric state, mainly dictated by the exponential decay law. In practice, the only method to possibly enhance the rate of recoil implantations in their short-lived excited states would be to select the heaviest beam available, which then would result in higher velocity and shorter flight time for the recoils. The upper limit for an appropriate half-life is set by the maximum time window of 32 μs for the observation of delayed γ rays in the acquisition system. In the analysis, the half-life is extracted from

the distribution of time differences between the implantation of a recoil in the focal-plane Si detector and the observation of the γ-ray of interest. However, this procedure requires the observation of these time differences over several half-life periods, which reduces the practical upper limit for a measurable half-life to a few microseconds.

3 Data Analysis

Although it is possible to examine the incoming data during the experiment, the complete analysis is always performed off-line. As described in Chapter 2, the data which are stored on tape have already been selected by applying various hardware gates. However, this is insufficient to extract the final experimental results for the nucleus of interest. The collected raw data must be calibrated and corrected against some well-known experimental effects and the recorded events have to be singled out using various analysis techniques. These procedures and the principles behind them will be reviewed in this chapter.

3.1 Data format

First of all, the analysis of the collected data requires a knowledge of the parameters which can be recorded into a single event. In the present work, the data words available in the ^{191}Bi experiment are

- total energy of a recoil or an α particle,
- vertical position (top and/or bottom) of a recoil or an α particle,
- number of the active strip in the Si detector,
- energies of prompt (at target position) and delayed (at focal plane) γ rays,
- time difference between the first and the second prompt or delayed γ ray,
- time of a prompt γ ray relative to the cyclotron RF,
- time difference between the observation of a recoil and detection of a prompt or delayed γ ray individually for each Ge detector,
- time difference between the observation of a recoil and detection of a prompt or delayed γ ray in any of the Ge detectors,
- energy of a signal observed in the gas counter (high and low gain),

- time difference between the detection of any delayed γ ray and a signal from the gas counter and
- a clock word (1 MHz, scale $0 - 72$ minutes).

The set of the recorded parameters may slightly vary between separate experiments according to the composition of the detector setup. A major part of the analysis was carried out by using the data in its original format and exploiting Eurogam-type sort programs based on the MTSort language. When necessary, a transformation to other formats (mainly for use in the RadWare software package [Rad95]) was performed.

3.2 Calibrations

3.2.1 Si-strip detector

The observed energy of an α particle has to be corrected against its dependency on the position of the interaction and the energy spectra collected from the individual Si-detector strips have to be gainmatched. In addition, if separate amplification channels are used to register the recoil implantations and emitted α particles, the position information of both type of events has to be unified. In the present work, where the properties of the α decay of interest are well-known, the main goal of these procedures is to ensure the cleanest possible gating conditions for the analysis of the γ-ray data.

Energy-position correction

The total energy of an α-decay event observed in the Si detector is constructed by summing up the signals received from the top and bottom ends of the active strip. Since the amplification channels used for these partial signals are not identical, the measured energy depends on the vertical position of the interaction. This effect is demonstrated in the left panel of Figure 3.1 (a) for a single strip in the ^{191}Bi experiment. The vertical line, which refers to the ideal case of position-independence, is drawn through a group of events corresponding to the α decay of the $1/2^+$ state in ^{191}Bi. The correction factor for the measured decay energies in this strip is extracted from the slope of a line, which is fitted to the α-decay energies in a transposed matrix of that shown in the left panel of Figure 3.1 (a). For comparison, a matrix generated using the corrected α-decay energies is presented in the right panel of Figure 3.1 (a). To better illustrate the effect of the performed correction, α-particle energy spectra, as obtained before and after the energy-position correction are created by projecting

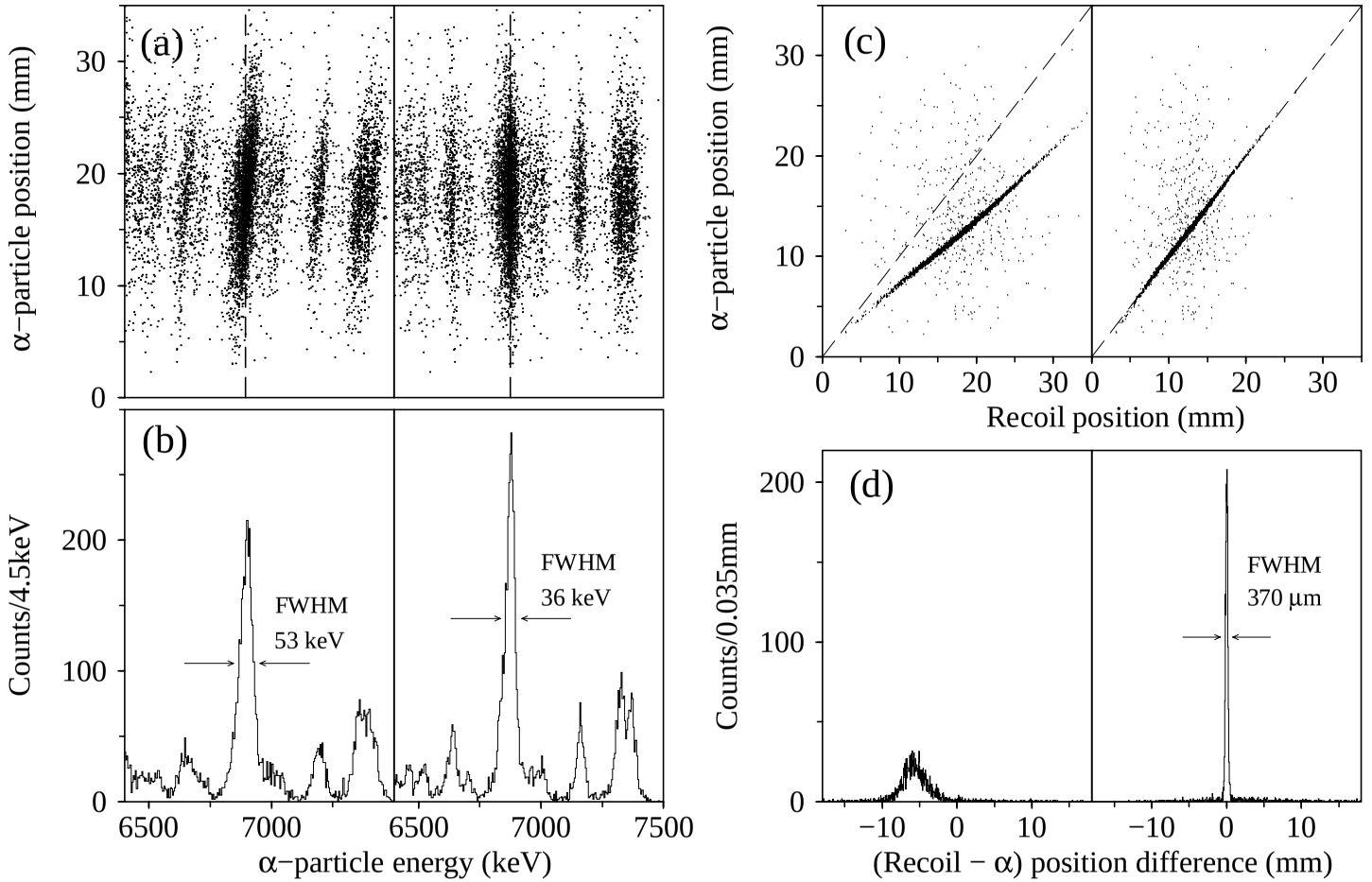

Figure 3.1: Corrections for strip 4 of the Si detector in the ^{191}Bi experiment. (a) Dependence of the observed α-particle energy on the vertical position of the interaction before (left panel) and after (right panel) the energy-position correction. The long-dashed vertical line corresponds to position-independence. (b) Projections of the matrices shown in (a) onto the α-particle energy axis. (c) Positions of observed α particles from the α decay of the $1/2^+$ state against the positions of the correlated recoils before (left panel) and after (right panel) the position-position correction. A maximum search time of 450 ms has been used. (d) Distribution of position differences between the correlated recoil and the α particle before (left panel) and after (right panel) the position-position correction.

the energy-position matrices onto the x-axis and shown in the left and right panel of Figure 3.1 (b), respectively. An inspection of these spectra shows an improvement of $\sim$ 30% in energy resolution for the peak corresponding to the α decay of the $1/2^+$ state in ^{191}Bi.

The energy-position correction is required only for α-decay events as there is no need to exactly know the recoil energies. In fact, the procedure would not even be feasible for recoil implantations since it is not possible to distinguish whether the observed distinction between the energies of two recoil events is due to the position dependence or a true difference in their energy.

Position-position correction

Since the α-tagging technique used in the present work is based not only on temporal but also on spatial correlations of an observed α decay and the preceding recoil implantation, the position information of both type of events has to be matched if two sets of amplification channels are used. The correction between the two scales is determined by generating for each strip a matrix where the measured position of a short-lived α decay is plotted on one axis and that of the preceding recoil event in the same strip on the other. In order to accept the spatial correlation, it is also required that the two events are observed within a time interval of typically three times the α-decay half-life. A sample correlation matrix, again for a single strip in the ^{191}Bi experiment is shown in the left panel of Figure 3.1 (c). The banana-shaped distribution representing the correlations made with the α decay of the $1/2^+$ state in ^{191}Bi is clearly distinguished from the low background due to its relatively short half-life ($\sim$150 ms) compared to the implantation rate. However, the correlated events lie well away from the diagonal line corresponding to the ideal situation where both events in a correlated α-recoil pair carry the same position information. The correction coefficients are extracted from a quadratic fit to the distribution, which after the correction is observed to follow the diagonal reference as illustrated in the right panel of Figure 3.1 (c). The distribution of position differences between the correlated events from the raw and corrected data are shown in the left and right panels of Figure 3.1 (d), respectively. It is evident that the very wide distribution has significantly narrowed in the correction procedure and is now centered around zero with a vertical position resolution of 370 μm for this strip.

Energy calibration

After the energy-position and position-position corrections, the final step is to perform an energy calibration for the α spectra collected from the individual Si-detector strips.

Since the measured α decays are well known in this case, the calibration is obtained by gainmatching the spectra using literature values for the energies of the observed α decays.

3.2.2 Ge detectors

As the main emphasis in the present work is on the study of γ rays, the spectra collected with individual Ge detectors have to be carefully gainmatched and calibrated in energy. Since the interpretation of γ-γ coincidence data strongly depends on the relative intensities of γ rays having different transition energies, a calibration for relative efficiency is performed. The overall capability of a Ge-detector array to observe the emitted photons is determined by its absolute efficiency which also is measured during the calibration procedure.

Energy calibration

The energy calibration for γ rays is performed using a mixed ^{133}Ba $+^{152}$ Eu source which covers an energy range from 81 to 1408 keV and hence is able to provide a reliable calibration for the transitions observed in the present work. Since thin targets are used, γ rays observed in the target-position array are emitted from forward-focused recoils and the measured transition energies are distorted due to Doppler shift. The measured γ-ray energies E and actual energies E_0 are related as

$$E = E_0\,(1 + \frac{v}{c}\,cos\,\theta), \tag{3.1}$$

where θ is the angle of the centre of the Ge detector relative to the beam axis and v is the recoil velocity. As the γ rays observed at the focal plane are emitted after the implantation of the recoil into the Si detector, the real transition energies for these events are directly obtained from the source-calibrated data.

Efficiency calibration

The single-step photoelectric effect dominates the interactions of γ rays with Ge at energies below 150 keV and the kinetic energy of the resulting single photoelectron is with high probability entirely absorbed into the active detector volume. At higher γ-ray energies, Compton scattering becomes dominant and photons initiated in this process are able to escape from the crystal. As the energy of the incident γ ray increases, the average energy received by the scattered photon also increases resulting in a larger probability for escape events. Moreover, the intrinsic efficiency of a single

Ge crystal to observe a γ ray with its full energy naturally depends on its active volume. All these effects combine to dictate the relative efficiency of a Ge-detector array. The efficiency is measured as a function of γ-ray energy by comparing the observed intensities of the transitions from the ^{133}Ba $+^{152}$ Eu source to their well-known actual intensities. This calibration was performed using the program 'effit' of the RadWare package [Rad95] and the resulting efficiency curves for the Jurosphere II array at the time of the ^{193}Bi experiment are illustrated in Figure 3.2. In addition to the total efficiency curve, separate curves for the Eurogam and for Nordball and TESSA type detectors are shown. Generally, very low-energy γ rays are blocked by the tin (0.25 mm) and copper (0.5 mm) absorbers mounted in front of the Ge detectors and by the thresholds set in the measurement electronics. The maximum efficiency is reached between 150 and 200 keV and as the γ-ray energy still increases, multi-step processes begin to dominate and a rapid decrease in efficiency is observed.

The efficiency curves shown in Figure 3.2 for the Jurosphere II array have been scaled to represent the absolute photopeak efficiency with which the emitted γ rays are

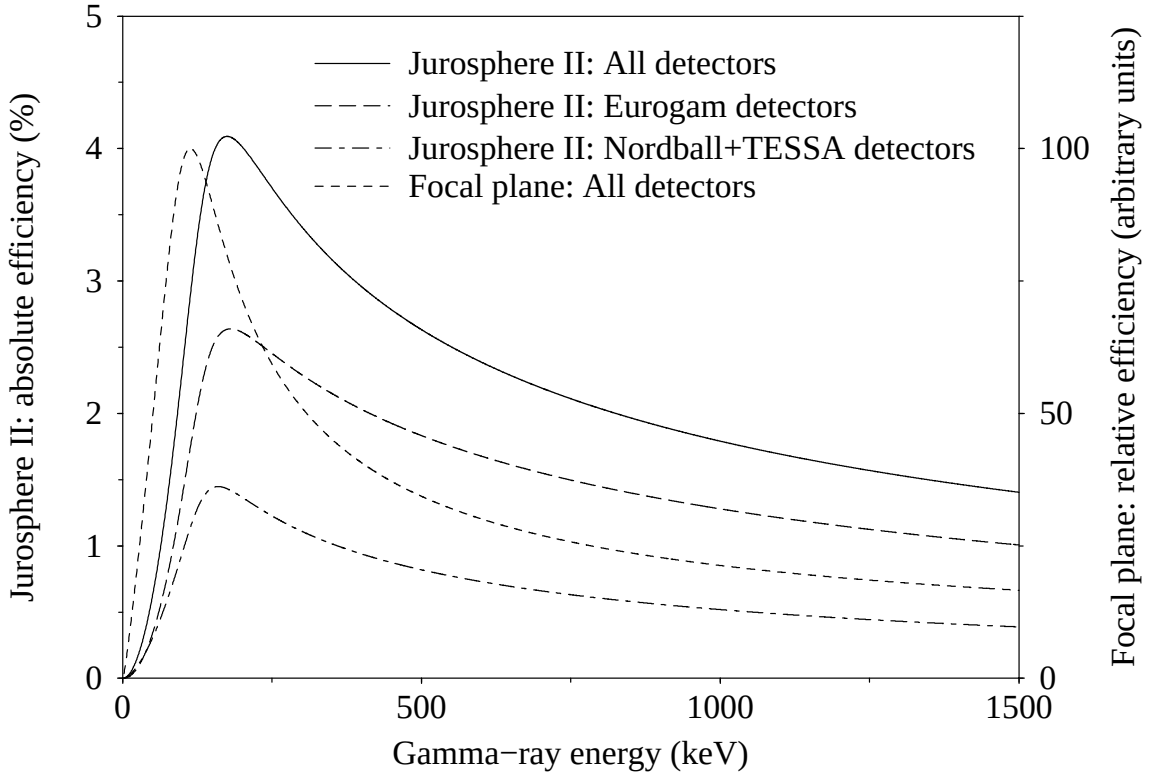

Figure 3.2: Absolute efficiency curves for all detectors in the Jurosphere II array (solid line) and separately for the Eurogam (long-dashed line) and Nordball and TESSA detectors (dot-dashed line) in the ^{191}Bi experiment. The relative efficiency curve for the focal-plane setup is also shown (dashed line).

measured. As the shape of the curve has been determined, the vertical scale is now fixed by measuring the absolute efficiency at one transition energy. The standard calibration procedure, also applied here, is to replace the target with a calibrated ^{60}Co source and measure the intensity of the 1332 keV γ-ray peak collected within a certain time interval. The absolute photopeak efficiency was measured to be $\sim$1.6% in the ^{193}Bi experiment when one of the Eurogam detectors was missing from the complete setup. In the ^{191}Bi experiment, the measured efficiency was $\sim$1.4% in the absence of three detectors and in the presence of background activities which resulted in a very strong 511 keV peak in the calibration spectrum.

In contrast, the curve for the five focal-plane detectors, also shown in Figure 3.2, represents the relative efficiency of the array in the ^{193}Bi experiment but is not scaled to the absolute value due to complications during the calibration procedure. As the implanted particles are distributed over the Si-detector area while the calibration source is point-like, the simulation of the experimental conditions is also in general more difficult at the focal plane than for the target-position array. The measured absolute photopeak efficiency for the data collected at the focal plane in the ^{191}Bi experiment was $\sim$0.9% using the source, but the actual efficiency realised in experimental conditions would probably be lower. This is due to the fact that γ rays emitted by the implanted recoils meet the Ge crystal at a variety of angles and the effective area of the front end of the detector decreases as the point of origin of the γ rays is not on the symmetry axis of the detector. The enhanced efficiency of the focal-plane array at low γ-ray energies compared to Jurosphere II results from the placement of one of the Nordball detectors facing the back of the Si-detector chamber at a very short distance and from the absence of absorbers.

3.3 Analysis methods

Analysis methods based on the selection of γ rays according to their correlation with various events observed at the focal plane of the RITU separator have proved to be a powerful tool in the study of very neutron-deficient nuclei. The recoil gating principle is used to select γ rays associated with any recoil whereas their identification to a specific nuclide is provided via a further correlation with a characteristic α decay (the recoil-decay tagging method). In the isomer tagging method, prompt γ rays feeding an isomeric state are linked with delayed γ rays depopulating the isomer. However, these procedures alone are not adequate to provide the optimal spectra and additional timing constraints are required to validate the γ rays. If the correlation techniques are not entirely applicable, other approaches to the experiment can be adopted.

3.3.1 Recoil gating

A recoil is identified by demanding that the measured energy of an implantation event in the Si detector is in a certain range, known as a gate, like that marked in the total singles energy spectrum collected in the ^{191}Bi experiment (Figure 3.3 (a)). This spectrum also illustrates the need of higher amplification for the measurement of α-particle energies as they appear compressed in the scale required for the recoil events. If the recoil distribution were to overlap with the α-particle energy peaks, a single set of amplification channels with suitably adjusted gains could be used and a coincidence with a gas-detector signal could then distinguish the recoil events. It can also be noted that some components of the chromium beam are not completely suppressed as the saturated energy signals originating from high-energy events are visible in this spectrum.

Recoil-gated γ rays, recorded into the same event with the recoil implantation, are further selected by applying three types of timing conditions. Firstly, prompt γ rays must be associated with the presence of a cyclotron beam pulse which is ensured by a gate on the spectrum of time differences between the cyclotron RF and the time of the γ ray, as shown in Figure 3.3 (b). The total time scale of 1 μs represents the time window set in the data acquisition system for collecting prompt γ rays (see Figure 2.6). To increment this spectrum, the presence of a recoil signal from the Si detector is also required. Secondly, the timing of each γ ray is separately checked against the time of the observation of the recoil, as shown in Figure 3.3 (c). The time scale of this spectrum represents a difference between a set delay and the actual flight time of the recoils from the target to the focal plane. As the recoils formed in fusion-evaporation reactions have similar masses, their flight times also are roughly the same resulting in a clear peak in the TAC spectrum. A third timing constraint is required in the investigation of γ-γ coincidences where the time difference between the first and the second γ ray within an event has to be in the peak of the TAC spectrum, as shown in Figure 3.3 (d). In this spectrum, the prompt peak at $\Delta t \sim 0$ represents higher-energy γ rays with good timing properties, whereas the additional structure originates from low-energy γ rays with a poorer time resolution. For γ-ray transitions observed at the focal plane, the appropriate timing requirements depend more on the physics case. For example, in order to examine transitions de-exciting an isomeric state having a half-life of the order of microseconds, the time window between the observation of a recoil and the delayed γ ray should be set to the maximum of 32 μs.

The recoil gating method is of great value when studying nuclei produced via relatively strong exit channels compared to the total cross section of the reaction. If this is the case, the selection of γ rays with only a minimum number of gating conditions can result in clean spectra with the best possible statistics, especially for the analysis of γ-γ coincidences. However, this technique does not provide a unique identification of recoils or γ rays, for which other methods, like recoil-decay tagging have to be used.

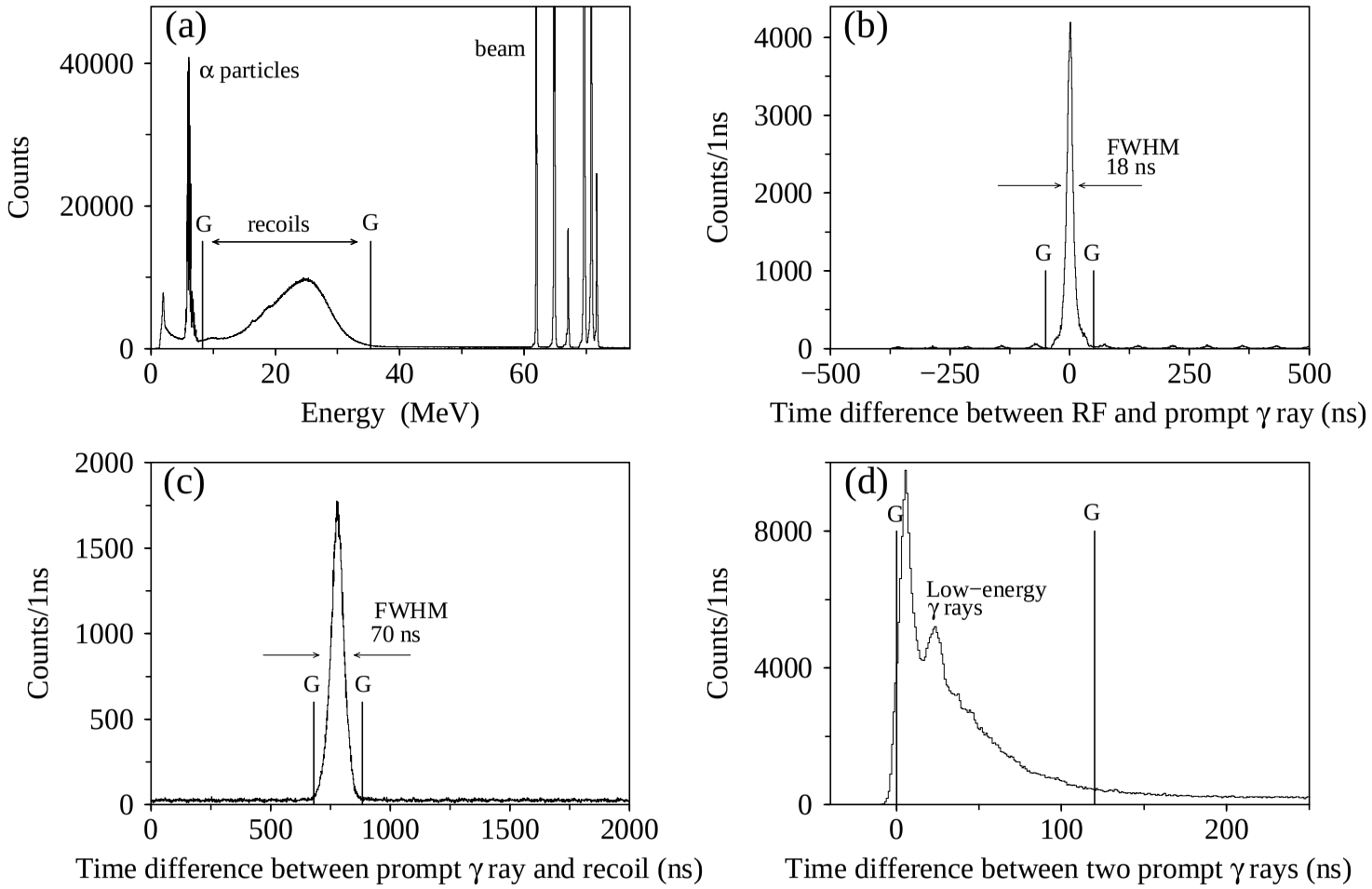

Figure 3.3: Applied gates (vertical lines marked with G) used in the selection of γ rays in the ^{191}Bi experiment. (a) Total singles energy spectrum observed in the Si detector. (b) Spectrum of time differences between the cyclotron RF and the observation of a prompt γ ray in Ge detector 18 (also requires the presence of a recoil implant). (c) Spectrum of time differences between the observation of a prompt γ ray in Ge detector 18 and the observation of a recoil. The horizontal scale indicates a difference between a constant delay and the flight time of the recoils to the focal plane. (d) Spectrum of time differences between the first and second prompt γ ray recorded into the same event.

3.3.2 Recoil-decay tagging (RDT)

The decay of the bismuth nuclei studied in the present work at least partly proceeds via the emission of an α particle having an energy and a half-life characteristic of the α-decaying state. In the light lead region, the α-decay energies typically fall between 6 and 8 MeV which results in a range of less than 0.05 mm for the emitted particle in the silicon material of the implantation detector. In the analysis, each Si-detector strip is divided into 1024 position bins which are 5 mm wide and 0.034 mm high. Thus, it can be assumed that the recoil which has emitted the observed α particle has been implanted in the same position bin or in either of the neighbouring bins in the vertical direction. However, as the resolution in measuring the position difference between the correlated α particle and recoil is of the order of 0.5 mm (see the right-hand panel of Figure 3.1 (d)), a vertical position window which is roughly 1 mm wide and centered in the position of the observed α particle is allowed in the analysis.

The first step in the recoil-decay tagging (RDT) [Sim86, Pau95] procedure is to select the valid recoil events using the same principles as described above for the recoil gating method. In addition, a valid clock stamp and position information for the event are now required. Instead of directly incrementing the γ-ray spectra, the energy and timing information for the recoil and the correlated γ rays are stored in a table according to the position where the implantation was observed. An α-decay event in the Si detector is identified and accepted for the correlation procedure if it passes an energy gate, has valid position information and a clock stamp and is in anti-coincidence with a signal from the gas counter. The correlation algorithm then proceeds by scanning through the position bins starting from that where the α particle was observed and looking for stored recoils at the same location. After going through the whole position window, the implant which is closest in time is taken as a candidate for the correlated recoil.

The final requirement in order to accept the correlation arises from the temporal spacing of the two events. Typically, the maximum time difference allowed between the observation of the recoil implantation and the α decay (*i.e.* search time) is chosen to be three α-decay halflives which covers 87.5% of the observed decays. To be able to rely on the recoil identification, the average time interval between successive recoil implantations within a single detector pixel should be much longer than the search time. Thus, the feasibility of an RDT analysis to study γ rays feeding a state which has a relatively long α-decay half-life is in the end determined by the interplay between sufficient statistics and low enough implantation rate. One method to confirm the origin of γ rays appearing in the energy spectrum of correlated events is to examine the behaviour of their intensities as a function of the search time. The number of accidentally correlated recoil-α pairs (N_{acc}) can be estimated as [Sch84, Lei83]

$$N_{acc} = T r_R \{1 - e^{r_\alpha t}\}, \tag{3.2}$$

where T is the duration of the experiment, r_R and r_α are the mean counting rates of

recoils and α-particles, respectively and t is the search time. If $r_\alpha t \ll 1$, Equation 3.2 simplifies to a form

$$N_{acc} = T r_R r_\alpha t \tag{3.3}$$

which indicates a linear increase for the intensities of γ rays originating from background activities with increasing search time. On the other hand, the intensities of transitions linked with the α decay follow an exponential behaviour like $1 - 2^{-t/t_{1/2}}$, where $t_{1/2}$ is the α-decay half-life. When the recoil-α correlation has finally been accepted, the γ rays in coincidence with the recoil are associated with the nucleus of interest and the spectra are incremented after applying similar timing conditions as described above for the recoil gating method.

Concerning the focal-plane data, practice has shown that even if the α-decay half-life is too long for RDT analysis of prompt γ rays, it may be possible to obtain a clean energy spectrum of delayed γ rays. This is due to the fact that not all of the recoils reach the focal plane in an excited state.

3.3.3 Isomer tagging

A natural requirement for isomer tagging analysis is that the recoil reaches the focal plane in an excited state which after the implantation de-excites via γ-ray emission. When the transition depopulating the isomer is identified, prompt γ rays recorded in the same event can be evaluated to establish the feeding of the isomeric state. As discussed in Section 2.6, the present experimental system introduces limits for halflives which are feasible for this type of study. If the isomer is strongly populated, prompt γ rays feeding this state may be resolved even if only a small portion of the recoils of interest which were formed in the target, preserve the excitation during their flight through the separator. In the present work, this was the case for the $13/2^+$ state in ^{193}Bi with a half-life of 153 ns which allows the observation of only 1% of the de-excitations at the focal plane. Nevertheless, the analysis of a prompt-delayed γ-γ matrix was able to reveal prompt γ-ray transitions feeding the isomeric state.

3.3.4 Excitation function measurements

As indicated above, recoil-decay tagging is the only one of the correlation methods which is able to provide the first identification of γ rays belonging to an α-decaying nucleus. If the decay half-life is unsuitably long for RDT analysis, the experiment can be performed at different beam energies in order to measure excitation functions. Provided that the separation between the adjacent bombarding energies is sufficient (a few MeV in the present mass region), the variation of γ-ray intensities as a function

of beam energy will be able to distinguish transitions belonging to the nucleus of interest from those originating from the neighbouring nuclei. For delayed γ rays, the identification of the element may be further ensured by coincidences of the observed transitions with the characteristic X-rays. Compared to an RDT measurement, this method does not set any upper limit on the implantation rate but rather requires a high beam current and thereby the best possible statistics can be achieved. On the other hand, the measured excitation functions do not link the observed transitions to any specific state in the nucleus of interest and hence, some additional information is required to initiate the construction of the level scheme. Excitation function curves were successfully measured in the ^{193}Bi experiment where a clear distinction between γ rays of interest and those from background activities was observed when using a step of 5 MeV in the beam energy.

4 Results

In the present work, the structure of the very neutron-deficient isotopes ^{191,193}Bi has been investigated for the first time using in-beam γ-ray spectroscopic methods. The experiments were performed at the Accelerator laboratory of the University of Jyväskylä (JYFL) where the heavy-ion beams were produced in an ECR ion source and accelerated in the K = 130 MeV cyclotron. The fusion-evaporation residues recoiling out of the thin target were separated from the primary beam and fission fragments using the gas-filled recoil separator RITU and implanted into the focal-plane Si detector where their subsequent α decays were measured. Prompt γ rays were recorded at the target position using the Jurosphere II Ge-detector array and those following the de-excitation of isomeric states were detected with five Ge detectors close to the Si-detector chamber.

In experiments of the present type, the observed quantities which directly relate to the structure of a nucleus are the energies of γ-ray transitions and α particles, the relative intensities of γ rays, the α-decay branches and the halflives of isomeric and α-decaying states. All the other measured parameters, for example the position information of the implantation events or the timing properties of prompt γ rays, are connected to the details of the experiment and can only be utilised in the selection of recoils and γ rays. The observed α decays are in the present analysis exploited in the identification of γ rays via the RDT method or excitation function measurements, whereas the level schemes of the nuclei of interest are based on the observed γ-γ coincidences and γ-ray energies and intensities. The spins of the deduced energy levels are extracted from the properties of γ-ray transitions connecting the states, such as their angular distributions. As the electric or magnetic character of the γ rays could not be distinguished, the parity assignments are based on theoretical expectations and comparison with systematics.

4.1 Introduction to odd-A bismuth isotopes

The ground states of the neutron-deficient odd-A bismuth isotopes with $199 \leq A \leq 209$ have been firmly attributed a spin and parity of $I^\pi = 9/2^-$ [Fir96] in accordance with the spherical shell model. In the lighter isotopes, the same assignment down to ^{187}Bi is supported mainly by the observation of unhindered α decays in the At $\rightarrow$ Bi $\rightarrow$ Tl decay chains [Fir96, Coe85, Coe86, Ket03b, Ket03c]. This state, having a single

proton in the $h_{9/2}$ orbital above the $Z = 82$ shell gap, decays entirely via β emission in bismuth isotopes with $197 \leq A < 209$ whereas in the lighter isotopes, α decay becomes competitive and finally dominant in ^{191}Bi [Fir96].

The $1/2^+$ state, observed over the whole range of known neutron-deficient odd-A Bi isotopes lies at 2443 keV in the stable nucleus ^{209}Bi and is observed to become lowered in excitation energy as the neutron number decreases [Hey83, Coe85, Ket03a, Ket03b]. This state is associated with a $2p - 1h$ shell-model intruder configuration where a proton is elevated across the $Z = 82$ shell thereby leaving a hole in the $s_{1/2}$ orbital [Alp69]. The excitation energies of the $3/2^+$ and $5/2^+$ states observed down to ^{199}Bi exhibit a similar behaviour and are tentatively assigned to configurations with a proton hole in the $d_{3/2}$ and $d_{5/2}$ orbitals, respectively [Alp69, Bra80]. The trend of decreasing excitation energy of proton intruder states with decreasing N is a combined effect of pairing interactions and proton-neutron interaction between the proton particle-hole configurations and valence neutrons [Hey87, Hey88]. The term valence includes both the particles and hole states. The de-excitation of the $3/2^+$ and $5/2^+$ states proceeds through γ-ray emission to other excited states and the same is observed for the $1/2^+$ state in isotopes with $203 \leq A \leq 209$ [Fir96]. As the $1/2^+$ state becomes the lowest excited state in ^{201}Bi, β- and α-decay begin to successfully compete in its de-excitation against the very slow M4 γ-ray transition to the $9/2^-$ ground state [Coe85, Bra80]. In ^{197}Bi, α decay becomes the main decay mode of the $1/2^+$ state and continues to dominate down to ^{187}Bi. In ^{185}Bi, the decay data have revealed proton- and α-decay branches from the $1/2^+$ state while the $9/2^-$ state remains unobserved [Dav96, Pol01, And03]. This may well imply that the $1/2^+$ state has become the ground state in ^{185}Bi [Pol01].

Isomeric $13/2^+$ states, assigned to have a single-particle character with the odd proton in the $i_{13/2}$ orbital, have been observed in the bismuth isotopes with $195 \leq A \leq 209$ and found to become lowered in excitation energy with decreasing neutron number [Fir96]. The depopulation of this state proceeds via γ-ray transitions to the $9/2^-$ ground state and to the $11/2^-$ and $13/2^-$ states which in the odd-A $^{197-207}$Bi have been established at around 1 MeV in excitation energy. An M2 transition to the ground state constitutes the sole de-excitation path of the $13/2^+$ state in ^{195}Bi and given the downward excitation energy trend of this state, the same is also expected for the lighter bismuth isotopes. In recent experiments, the transitions de-exciting the $13/2^+$ isomeric state in ^{189}Bi [And01] and ^{187}Bi [Hür02] have been observed.

In the present study, the focal-plane detector system allows the α decays of the $1/2^+$ and $9/2^-$ states and the de-excitation of the isomeric $13/2^+$ state to be measured in ^{193}Bi and ^{191}Bi. The sophisticated correlation methods used in the analysis will provide a unique identification of prompt γ rays feeding these characteristic structures. In the odd-A isotopes down to ^{195}Bi, the observed excited states have been successfully interpreted as the odd proton coupled to spherical structures in the even-even Pb core

[Lon86, Cha86, Pie85, Hüb78, Lon82]. This approach is based on the principles of the weak-coupling scheme [Sha61] and level energy systematics providing a qualitative and in some cases a quantitative description of the spherical structures. Compared with the heavier isotopes, new features in the structure of ^{191,193}Bi might be expected since low-lying collective bands associated with oblate- and prolate-deformed intruder states have been found to dominate the structure of neighbouring nuclei near the neutron mid-shell (see [Jul01] for a review). However, as collective effects have not been observed in ^{195}Bi, some structures corresponding to those found in the heavier isotopes may still persist in ^{193}Bi and ^{191}Bi.

4.2 ^{193}Bi

The experiment to study ^{193}Bi was realised by bombarding a 350 μg/cm^2 thick ^{165}Ho target with a ^{32}S beam at energies from 142 to 157 MeV (in the centre of the target) in 5 MeV steps. The effective beam time was 110 hours.

4.2.1 Production rates and α spectra

Although the $9/2^-$ ground state in ^{193}Bi has an α-decay branch of only $b_\alpha = 3.5(15)\%$ [Art98], in total approximately 265000 α decays from this state were observed. The decay proceeds via two channels, one having $E_\alpha = 5899(5)$ keV with an intensity of $I_\alpha = 95.8(5)\%$ of the total number of decays and the other $E_\alpha = 6174(5)$ keV with $I_\alpha = 4.2(5)\%$ [Fir96]. Since the half-life of 67(3) s [Art98] of this state is far too long for obtaining clean recoil-α correlations, the identification of γ rays feeding this state is based on their excitation functions. The beam energies were selected around the calculated optimum value for the $4n$ channel leading to ^{193}Bi. As the counting rate in the Si detector was not a limiting factor, a major part of the experiment was performed using an average beam current of 25 pnA which was the maximum allowed by the Ge singles counting rate.

The $1/2^+$ intruder state in ^{193}Bi lies at an excitation energy of 307(7) keV [Fir96] having a total α-decay branch of $b_\alpha = 90^{+10}_{-20}\%$ [Art98] and an α-decay half-life of $t_{1/2} = 3.2(6)$ s [Art98]. From this state, approximately 180000 α decays ($E_\alpha = 6475(5)$ keV [Fir96]) were detected during the experiment. In order to make the first unambiguous identification of γ rays feeding this state, about 13500 of the observed α particles were collected using an average beam current of 3 pnA at a beam energy of 152 MeV. The resulting recoil rate in the Si detector was low enough to allow clean recoil-α correlations and thereby the selection of γ rays using the RDT method.

The energy spectra of α particles collected in the focal-plane Si detector of the RITU separator are shown in Figures 4.1 (a)-(d) separately for each of the beam energies. Since the recoils and α particles are observed via the same amplification channels, an anti-coincidence with a signal from the gas counter is required in order to validate the α-decay events. As evident from the spectra, ^{193}Bi is the main α-decaying reaction product at the three lowest bombarding energies, whereas at 157 MeV, the $5n$ channel leading to ^{192}Bi gains intensity. The other open exit channels in the fusion-evaporation reactions mainly lead to various Pb isotopes which decay via β emission. The measured spectra also indicate the preferred population of the high-spin $9/2^-$ state compared to the low-spin $1/2^+$ state as the average excitation energy and angular momentum of the residual ^{193}Bi nucleus increase with increasing beam energy. However, when taking into account the α-decay branches, the effect is not as clear as the apparent change in the observed intensities. At the lowest beam energy of 142 MeV, the $9/2^-$ ground state collects $\sim$96% of the total feeding while $\sim$4% populates the $1/2^+$ intruder state. At the beam energy of 157 MeV, the population of the ground state has increased to $\sim$98%, leaving $\sim$2% for the low-spin intruder configuration.

The total production cross-section of ^{193}Bi is estimated by considering the features of the present experimental setup. Approximately 80% of the ^{193}Bi recoil distribution was covered by the Si detector and the probability to observe the α decay with its full energy was assumed to be 50%. A transmission of 20% for the recoils of interest through the RITU separator was assumed and the effect of the deterioration of the target observed during the experiment was also estimated. Taking into account the α-decay branching ratios, a cross section of about 3 mb for the ^{165}Ho(^{32}S,$4n$)^{193}Bi reaction at 152 MeV can finally be deduced.

4.2.2 Identification of the $13/2^+ \rightarrow 9/2^-$ transition

The isomeric $13/2^+$ state lies at an excitation energy of 1196 and 888 keV in ^{197}Bi [Cha86] and ^{195}Bi [Lon86], respectively, and de-excites via an isomeric M2 γ-ray transition to the $9/2^-$ ground state. Lonnroth *et al.* [Lon86] predict the excitation energy of the $13/2^+$ state in ^{193}Bi to be 460(50) keV, corresponding to a half-life of 0.5 μs. Their estimate of the lowering of the excitation energy of this state is based on the interaction of the $i_{13/2}$ proton with the increasing number of $i_{13/2}$ neutron holes as the $\nu i_{13/2}$ orbital opens up at $A = 197$ and becomes more depleted in going to lighter isotopes. Considering the present experiment, a half-life of 0.5 μs would be long enough so that a large number of the recoils would survive the 1-μs flight to the separator focal plane in the excited state, especially as the production cross section is relatively high. In addition, the presumed downward trend of the excitation energy as a function of decreasing neutron number would reinforce the yrast character of this state and thus enhance its feeding compared to that in the heavier bismuth isotopes.

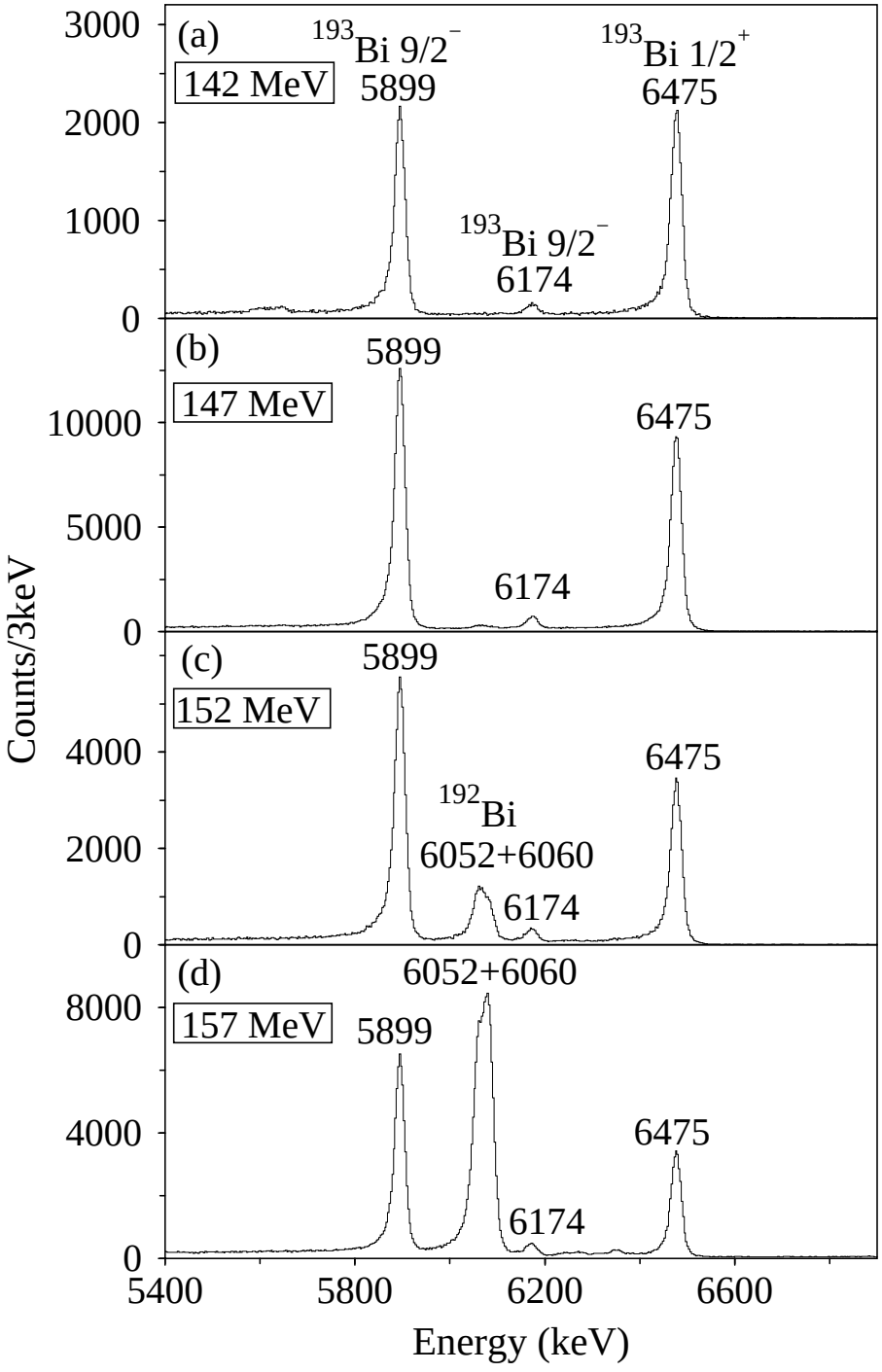

Figure 4.1: Energy spectra of α particles observed in the focal-plane Si detector from the ^{32}S + ^{165}Ho $\rightarrow$ ^{197}Bi* reactions at a beam energy of (a) 142 MeV, (b) 147 MeV, (c) 152 MeV and (d) 157 MeV in the centre of the target. The gas counter signal was used as a veto.

The total spectrum of recoil-gated singles γ rays observed in the focal-plane Ge detectors up to 30 μs after the implantation of a recoil is shown in Figure 4.2 (a). The known transitions originating from ^{192}Pb [Lag91, Plo93a] and ^{194}Pb [Fan91] are indicated with symbols and those which in the course of the present work have been assigned to ^{193}Bi are marked with their energy. There are several previously unknown lines in the energy range from 400 to 650 keV and the identification of the $13/2^+ \rightarrow 9/2^-$ transition from this spectrum alone is not possible. As the predicted half-life for the $13/2^+$ state is much shorter than the 30 μs time window, a spectrum of delayed γ rays observed within 220 ns after a recoil implantation was generated and is shown in Figure 4.2 (b). To create this spectrum, the data collected at a beam energy of 147 MeV were chosen as they have the best statistics. The effect of the shorter time window is to enhance the observed intensity of γ rays following the de-excitation of short-lived isomeric states relative to those depopulating isomers with longer halflives.

However, in the spectrum shown in Figure 4.2 (b) there are no candidates for the $13/2^+ \rightarrow 9/2^-$ transition in the predicted energy range of 400 to 500 keV while there are several unknown lines in the range of 500 to 650 keV. In this spectrum, the 605 keV peak is much more prominent compared to the other observed transitions than in the case of the longer time window (Figure 4.2 (a)) thus indicating a state with a relatively short half-life. The half-life associated with each of these transitions is deduced from the distribution of time differences between the implantation of a recoil into the Si detector and the observation of the γ ray of interest. The 550, 597, 620, 624 and 634 keV transitions exhibit halflives of $t_{1/2} \gtrsim 3$ μs which are far too long to agree with the prediction for the $13/2^+ \rightarrow 9/2^-$ transition. Moreover, they are in coincidence with each other and thus excluded from the presumed single-step de-excitation of the $13/2^+$ state. On the other hand, the half-life of 153(10) ns associated with the 605 keV transition (see Figure 4.3 (a)) is closer to the prediction given for the $13/2^+$ state in ^{193}Bi. The Weisskopf estimate for the strength of this transition was calculated assuming that the de-excitation of a level at 605 keV proceeds only via the 605 keV γ ray. The obtained value of $B(M2) = 0.062(10)$ W.u. is in very good agreement with that for the predicted transition energy of 460 keV having a half-life of 0.5 μs ($B(M2) \sim 0.06$ W.u.). The corresponding hindrance factor of 16 is of the same order of magnitude as the value of ~ 45 for the $13/2^+ \rightarrow 9/2^-$ spin-flip transition in ^{197}At [Smi99]. Therefore, the 605 keV transition is a strong candidate for the $13/2^+ \rightarrow 9/2^-$ transition in ^{193}Bi.

4.2.3 Excitation functions

Since the examination of the recoil-gated spectra does not provide a unique identification of γ rays, excitation functions were measured to confirm the assignment of γ-ray transitions to ^{193}Bi. In this procedure, the number of the observed α decays of

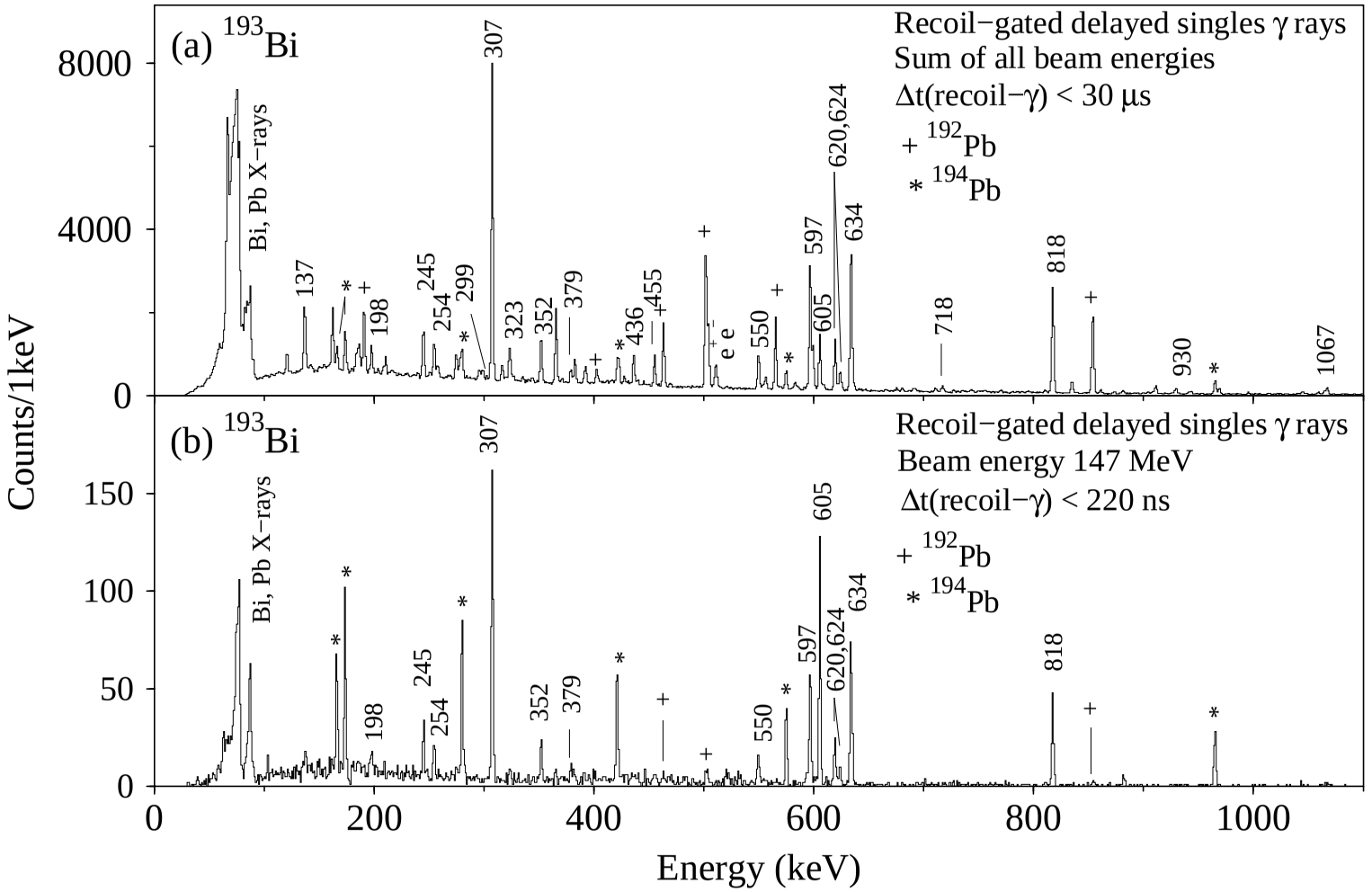

Figure 4.2: Energy spectra of recoil-gated singles γ rays from ^{32}S + ^{165}Ho reactions observed at the focal plane within (a) 30 μs and (b) 220 ns after the implantation of a recoil. In (a), a sum of spectra obtained at all beam energies is shown, in (b) a beam energy of 147 MeV was used. Transitions assigned to ^{193}Bi are marked with their energy, those belonging to ^{192}Pb and ^{194}Pb are indicated with plus-signs and asterisks, respectively.

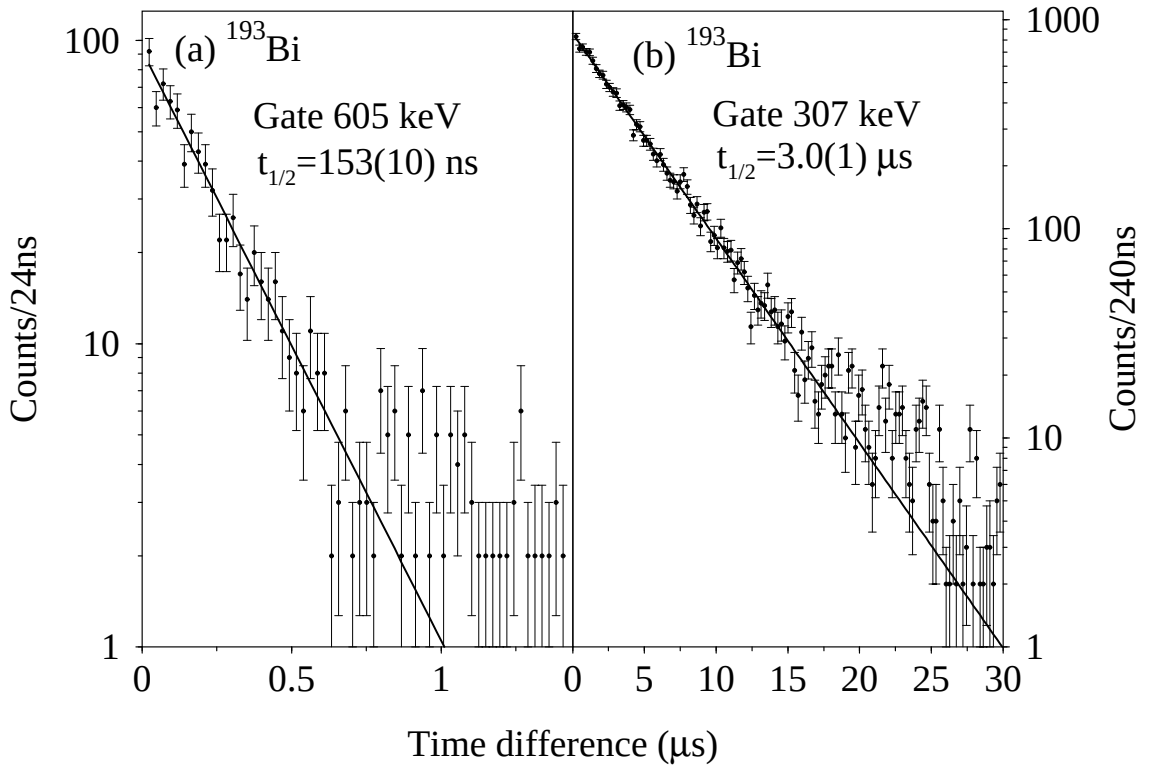

Figure 4.3: Spectrum of time differences between the implantation of a recoil and the observation of a (a) 605 keV and (b) 307 keV γ ray in the focal-plane Ge detectors.

the $9/2^-$ ground state at each beam energy was taken as a reference to which the intensities of the observed γ rays were then normalised. The resulting excitation function curves for selected delayed (137, 307 and 605 keV) and also prompt (279, 299 and 323 keV) γ rays are illustrated in Figure 4.4. As evident, the intensities of these transitions follow a consistent trend which is clearly different from the behaviour of the corresponding curves for the 854 (^{192}Pb) [Lag91, Plo93a], 882 (^{193}Pb) [Lag91] and 965 keV (^{194}Pb) [Fan91] transitions. Therefore, all these γ rays are associated with ^{193}Bi. The discussion presented in Section 4.2.2 supports the assignment of the 605 keV transition as de-exciting the $13/2^+$ isomeric state in ^{193}Bi.

Figure 4.4 shows that the relative intensities of the γ rays now associated with ^{193}Bi are not constant but first increase with increasing beam energy, reach a maximum at 152 MeV and then slightly decrease towards 157 MeV. The upward-sloping behaviour is partly due to the enhanced population of high-spin states as the average excitation energy and angular momentum brought into the compound nucleus increase with increasing beam energy.

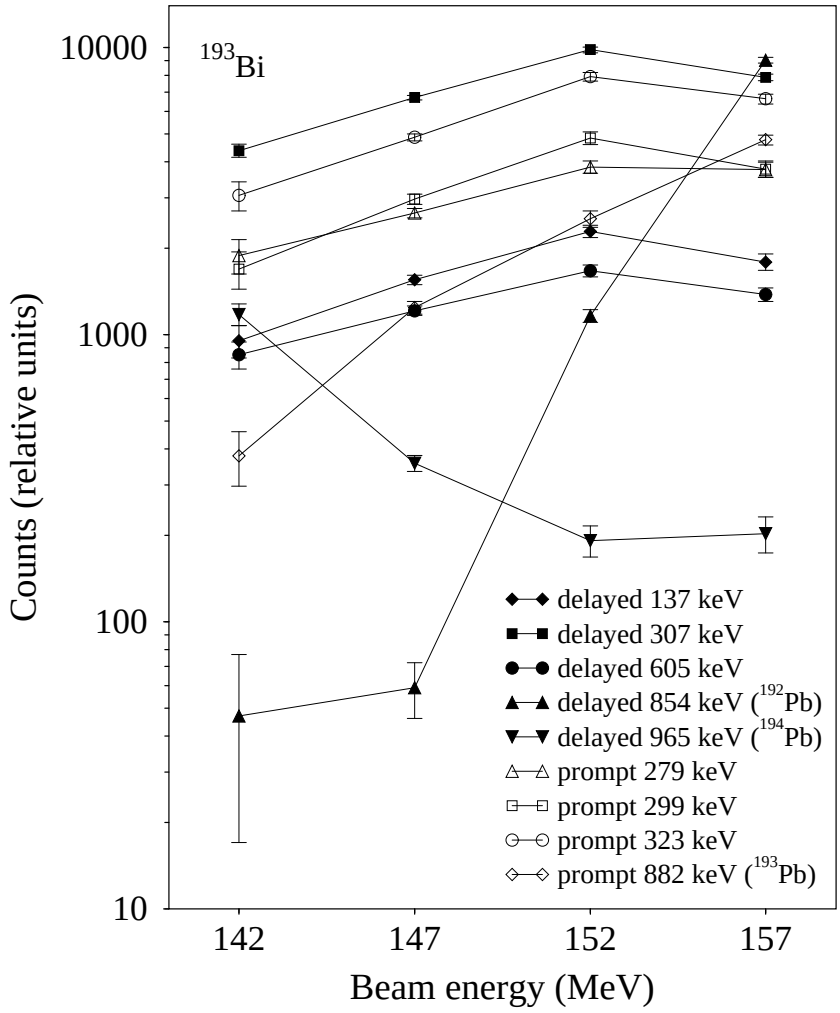

Figure 4.4: Relative intensities of the 137, 307 and 605 keV delayed (filled symbols) and 279, 299 and 323 keV prompt (open symbols) γ rays as a function of beam energy normalised to the number of observed α decays of the $9/2^-$ state in ^{193}Bi. For comparison, intensities of the delayed 854 (^{192}Pb) and 965 keV (^{194}Pb) transitions together with the prompt 882 keV (^{193}Pb) γ ray are also shown.

4.2.4 Band feeding the $13/2^+$ state

The energy spectrum of recoil-gated prompt singles γ rays is presented in Figure 4.5 (a) showing several previously unidentified lines together with some known transitions from the Pb isotopes. In order to select the γ rays feeding the $13/2^+$ isomeric state in ^{193}Bi, a recoil-gated delayed-prompt γ-γ matrix was created. In this matrix, a gate set on the delayed 605 keV transition provides a spectrum of correlated prompt γ rays with a clear peak at 323 keV, as shown in Figure 4.5 (b). The low statistics in this spectrum is due to the short half-life of the $13/2^+$ state (153 ns) compared to

the flight time of the ^{193}Bi recoils through the RITU separator ($\sim$1 μs). The 323 keV transition, also appearing in the recoil-gated singles γ-ray spectrum (Figure 4.5 (a)), is placed directly feeding the $13/2^+$ isomeric state. The coincident prompt γ rays were studied by analysing a recoil-gated γ-γ matrix using the RadWare software package [Rad95]. A sample coincidence spectrum gated by the prompt 323 keV transition is illustrated in Figure 4.5 (c) showing two groups of transitions, one at $\sim$ 300 keV and the other at $\sim$ 600 keV which usually suggests the observation of a strongly coupled band. The deduced band structure feeding the $13/2^+$ state (Band 1) is shown in the level scheme of ^{193}Bi (Figure 4.6) and the assignment of two of the band members (323 and 299 keV) to ^{193}Bi is further confirmed by their measured excitation functions (see Figure 4.4).

Angular distributions for γ rays were determined from their observed intensities in recoil-gated spectra which were measured at a beam energy of 147 MeV with detectors at angles of 158° and 79° with respect to the beam direction. The extracted efficiency-corrected intensity ratios $R_{exp} = I(158°)/I(79°)$, together with γ-ray energies and intensities of transitions assigned to ^{193}Bi, are listed in Table 4.1. Theoretical predictions for the values of angular distributions (R_{th}) can be extracted from simplified formulations and tabulated coefficients such as those presented by Yamazaki [Yam67]. For example, the calculations yield $R_{th} = 0.69$ and $R_{th} = 1.62$ for a stretched (*i.e.* pure) dipole and quadrupole transition de-exciting a state with spin 21/2, respectively. These values are in agreement with the value of $R_{exp} = 0.74(8)$ for the $21/2^+ \rightarrow 19/2^+$ (319.9 keV) transition and that of $R_{exp} = 1.54(11)$ for the $21/2^+ \rightarrow 17/2^+$ (647.1 keV) transition deduced in the present experiment. For initial states with low spin, the difference in R_{th} between dipole and quadrupole transitions is smaller compared with that for high-spin states and the measurements are further complicated by mixing of transition multipoles. These mixtures, which tend to shift the measured angular distribution values towards unity, cannot usually be resolved in experiments for exotic nuclei due to low statistics.

For the band feeding the $13/2^+$ state, the obtained values of R_{exp} are in accordance with its suggested strongly coupled nature. The 323, 299, 327, 320, 346 and 315 keV transitions are assigned to be dipoles, probably M1 in character and the same assignment is tentatively made also for the 220 and 204 keV transitions although their low intensities do not permit angular distribution measurements. The R_{exp} values for the 647, 665 and 661 keV transitions are comparable with that of 1.43(10) measured for the 882 keV $17/2^+ \rightarrow 13/2^+$ E2 transition in ^{193}Pb and they are assigned to have quadrupole character. Their placement as crossover transitions in the band feeding the $13/2^+$ state yields E2 multipolarity for these three γ rays. The E2 assignment has also been made to the 623 and 627 keV transitions despite the lack of angular distribution information due to strong contamination from nearby lines, and for the 536 keV transition which is too weak for meaningful angular distribution measurements.

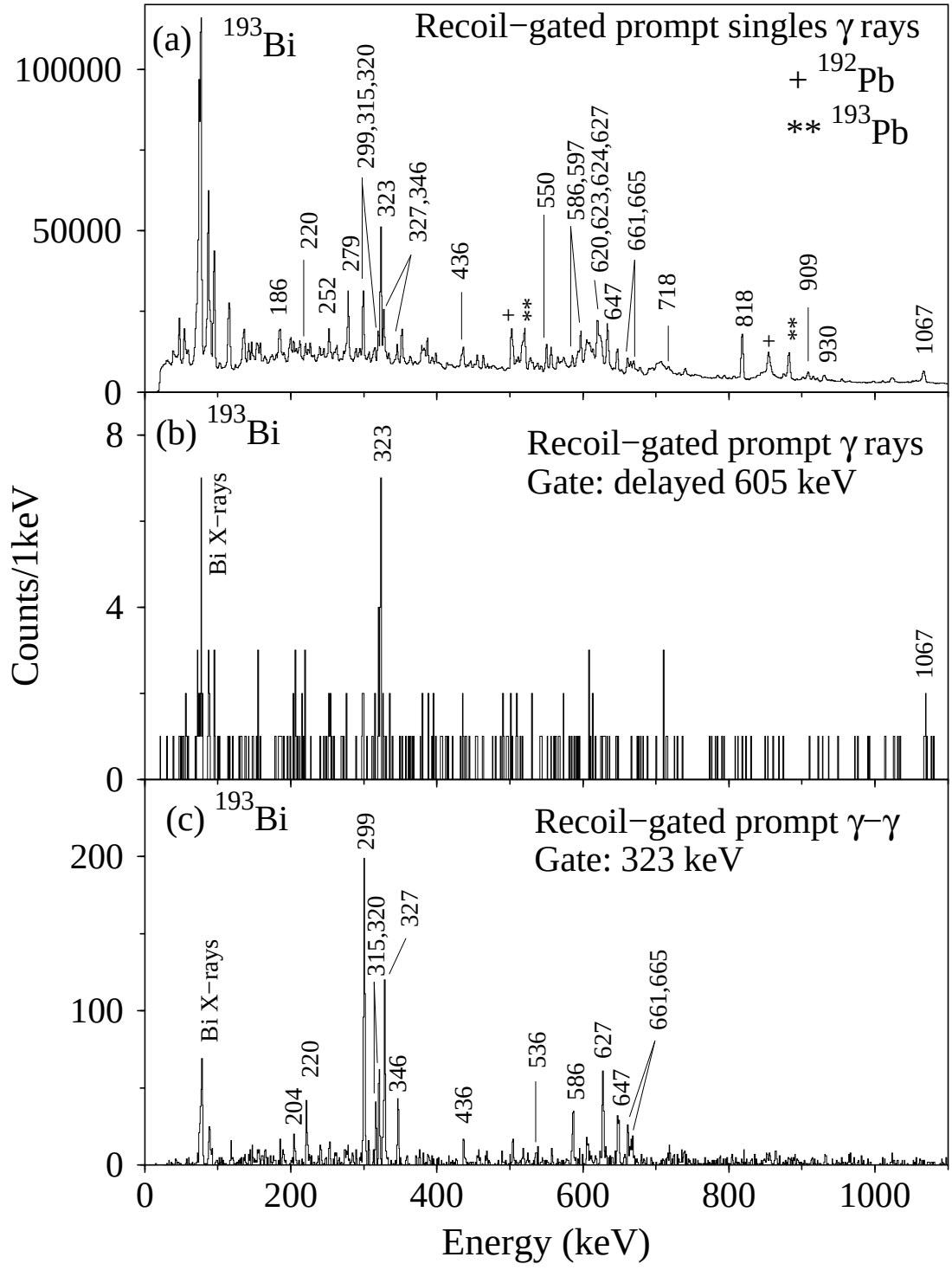

Figure 4.5: (a) Recoil-gated singles spectrum of prompt γ rays from ^{32}S + ^{165}Ho reactions where transitions assigned to ^{193}Bi are marked with their energy. (b) Energy spectrum of recoil-gated prompt γ rays gated by the 605 keV delayed transition. (c) Recoil-gated spectrum of prompt γ rays gated by the 323 keV prompt transition.

The 586 keV transition is observed to be in coincidence with the 323 keV $15/2^+ \rightarrow 13/2^+$ transition (Figure 4.5 (c)) and assigned to be of dipole character indicating a $(17/2^+)$ state at 1514 keV. The 436 keV dipole transition is placed to feed this 1514 keV level and the coincident 909 keV transition to de-excite it and populate the $13/2^+$ band head.

Table 4.1: The γ-ray energies, intensities and angular distribution ratios for transitions assigned to ^{193}Bi.

E_γ (keV)	I_γ (%)	E_i (keV)	I_i^π	I_f^π	$R_{exp} = I(158°)/I(79°)$
137.0(5)[1]	1.8(6)	1672	$(17/2^+)$	$(15/2^+)$	
185.7(5)	7.7(10)		(j+3)	(j+2)	
198.0(5)	7.3(6)	818	$13/2^-$	$11/2^-$	0.9(2)
199.9(5)	9.0(5)	507	$(3/2^+)$	$1/2^+$	1.0(3)
204(1)	3.0(5)	2961	$(29/2^+)$	$(27/2^+)$	
220(1)	12.7(5)	2757	$(27/2^+)$	$25/2^+$	
229.5(5)	2.3(10)	736	$(5/2^+)$	$(3/2^+)$	
245.2(5)	6.4(8)	1415	$17/2^-$	$15/2^-$	0.8(2)
252.3(5)	10.4(10)		(j+4)	(j+3)	0.7(2)
254.0(5)	5.5(6)	2050	$21/2^-$	$19/2^-$	0.7(4)
278.8(3)	45(1)		(j+2)	j	1.15(7)
279.2(5)	1.7(6)	1015	$(7/2^+)$	$(5/2^+)$	
289.2(5)	4.1(6)	$3401 + \Delta$	$(35/2^-)$	$(33/2^-)$	0.6(3)
295.7(5)	5.5(7)		(j+6)	(j+5)	
298.8(5)	5.5(8)		(j+5)	(j+4)	
299.3(5)	61(4)	1228	$17/2^+$	$15/2^+$	0.82(7)
307.0(5)	10.5(9)	2357	$(25/2^-)$	$21/2^-$	1.2(2)
315.2(5)	11.4(8)	2536	$25/2^+$	$23/2^+$	0.71(15)
319.9(5)	23.6(14)	1875	$21/2^+$	$19/2^+$	0.74(8)
323.4(3)	100(6)	928	$15/2^+$	$13/2^+$	0.90(6)
327.3(3)	47(3)	1555	$19/2^+$	$17/2^+$	0.84(7)
345.8(5)	18.6(11)	2221	$23/2^+$	$21/2^+$	0.67(11)
351.9(3)	36(3)	1170	$15/2^-$	$13/2^-$	0.86(9)
355.3(7)	1.8(7)				
356(1)	5.2(11)	$3112 + \Delta$	$(33/2^-)$	$(31/2^-)$	0.6(3)
379.3(5)	13.6(14)	1795	$19/2^-$	$17/2^-$	0.71(14)
384(1)	10.9(13)			(j+2)	
398.8(5)	9.0(5)	$2756 + \Delta$	$(31/2^-)$	$(29/2^-)$	0.8(2)
415.2(5)	2.3(6)	2464	$(23/2^-)$	$21/2^-$	
432(1)	2.9(9)				
436.0(5)	9(2)	1950	$(19/2^+)$	$(17/2^+)$	0.92(11)
436(1)	3.1(12)	2108		$(17/2^+)$	
455.0(5)	3.6(14)	2127		$(17/2^+)$	
458.5(7)	1.8(7)				
468.8(7)	2.4(8)				

Table 4.1: The γ-ray energies, intensities and angular distribution ratios for transitions assigned to ^{193}Bi (continued).

E_γ (keV)	I_γ (%)	E_i (keV)	I_i^π	I_f^π	$R_{exp} = I(158°)/I(79°)$
479(1)	6.0(13)	$(3235 + \Delta)$		$(31/2^-)$	
504.5(5)	4.3(7)	1520	$(11/2^+)$	$(7/2^+)$	
508.9(5)	5.0(16)	1015	$(7/2^+)$	$(3/2^+)$	
536(1)	2.7(8)	2757	$(27/2^+)$	$23/2^+$	
538(1)	9.1(8)	2588	$(25/2^-)$	$21/2^-$	
550.0(3)	37(3)	1170	$15/2^-$	$11/2^-$	1.30(10)
551.1(5)	6.1(9)		(j+5)	(j+3)	
585.9(5)	19(3)	1514	$(17/2^+)$	$15/2^+$	1.0(2)
595(1)	1.5(8)		(j+6)	(j+4)	
597.0(3)	56(4)	1415	$17/2^-$	$13/2^-$	
605.0(5)		605	$13/2^+$	$9/2^-$	
620.0(5)	68(1)	620	$11/2^-$	$9/2^-$	
622.7(5)	32(3)	1228	$17/2^+$	$13/2^+$	
624.5(5)	34(3)	1795	$19/2^-$	$15/2^-$	
626.6(5)	29(3)	1555	$19/2^+$	$15/2^+$	
634.4(5)	34(3)	2050	$21/2^-$	$17/2^-$	1.17(8)
634(1)	8.2(11)			(j+3)	
638(1)	5.5(13)			(j+2)	
647.1(5)	26(2)	1875	$21/2^+$	$17/2^+$	1.54(11)
648(1)	4.5(9)			(j+4)	
661.2(5)	18.6(11)	2536	$25/2^+$	$21/2^+$	1.36(11)
665.2(5)	15.9(12)	2221	$23/2^+$	$19/2^+$	1.46(14)
670.0(5)	12.3(12)	2464	$(23/2^-)$	$19/2^-$	1.5(2)
718.5(5)	8.6(14)	1535	$(15/2^+)$	$13/2^-$	
754(1)	4.5(5)	$3112 + \Delta$	$(33/2^-)$	$(29/2^-)$	
818.2(3)	85(9)	818	$13/2^-$	$9/2^-$	1.34(7)
909.2(9)	20(9)	1514	$(17/2^+)$	$13/2^+$	1.2(2)
930.0(5)	14.5(15)	1535	$(15/2^+)$	$13/2^+$	1.0(2)
1067(1)	29.5(13)	1672	$(17/2^+)$	$13/2^+$	1.50(11)

[1] Has two components in data collected at focal plane.

4.2.5 Negative-parity states

As presented in Figure 4.4, the measured excitation functions confirm the assignment of the 307 keV γ ray to ^{193}Bi. Figure 4.7 (a) shows a spectrum generated by summing coincidences with the 307, 597, 634 and 818 keV transitions in a recoil-gated delayed γ-γ matrix. Due to intensity arguments, the 307 keV transition is placed to be the topmost in a cascade populated by the de-excitation of an isomeric state with a half-life

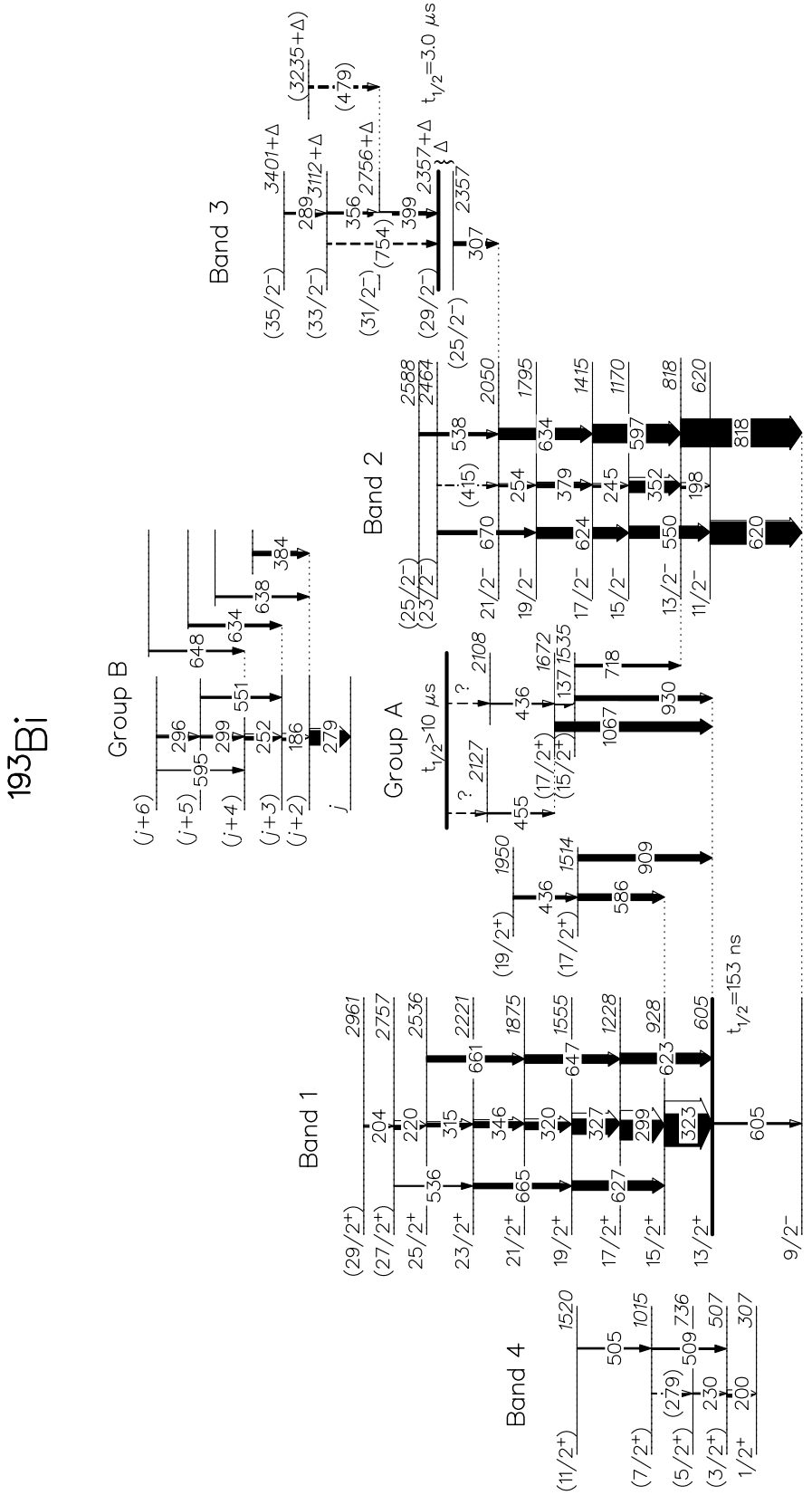

Figure 4.6: Level scheme of ^{193}Bi.

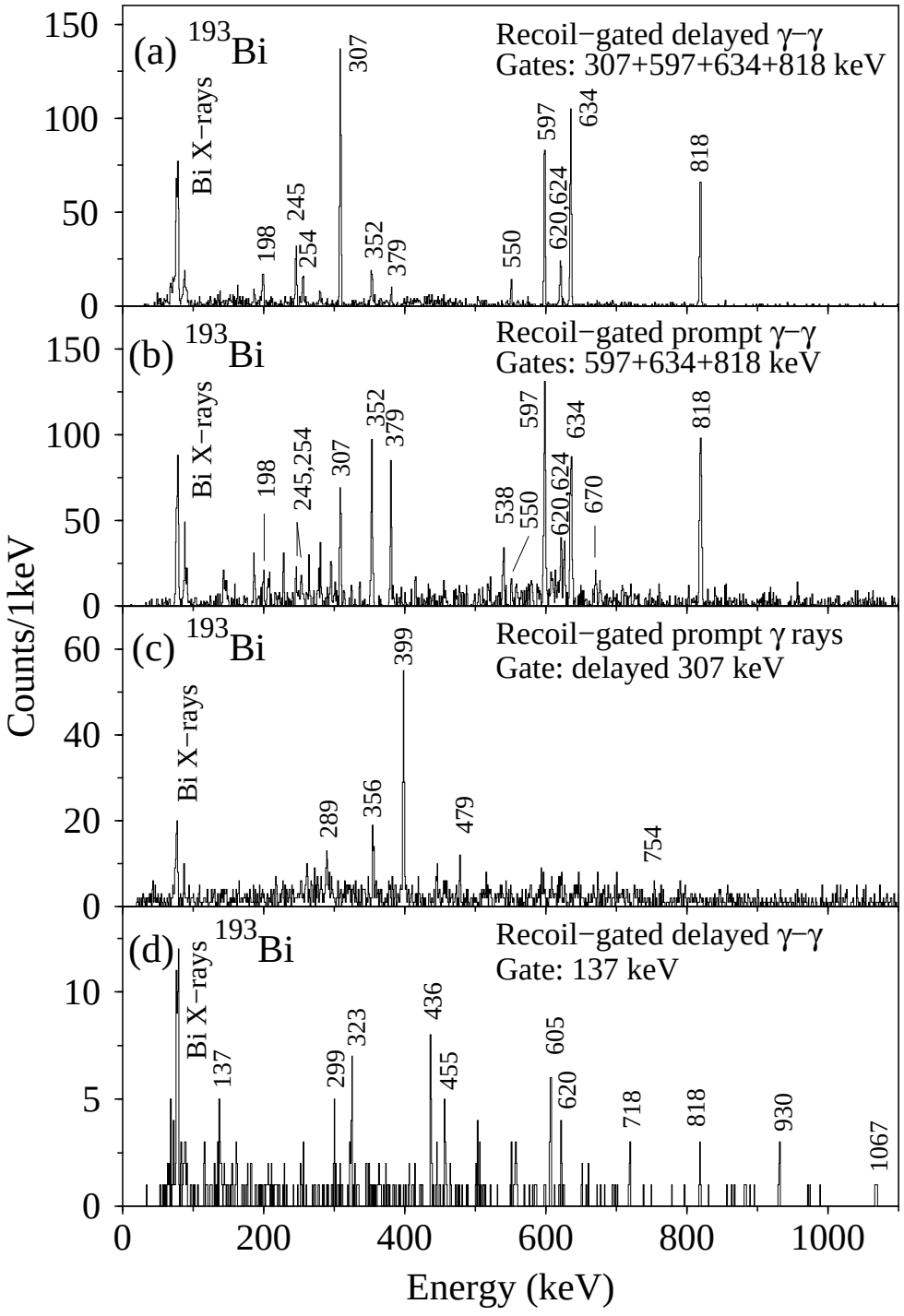

Figure 4.7: Energy spectra of recoil-gated γ rays from the ^{32}S + ^{165}Ho reactions. (a) Sum of spectra of delayed γ rays gated by the delayed 307, 597, 634 and 818 keV transitions. (b) Sum of spectra of prompt γ rays gated by the prompt 597, 634 and 818 keV transitions. (c) Spectrum of prompt γ rays gated by the 307 keV delayed transition. (d) Spectrum of delayed γ rays gated by the delayed 137 keV transition.

of 3.0(1) μs (see Figure 4.3 (b)). As illustrated in Figure 4.7 (b), the same cascade of γ rays is observed also in the target-position array which indicates prompt feeding into the band and enables the determination of angular distributions as defined above. The negative-parity band (Band 2) in the level scheme shown in Figure 4.6 is constructed based on γ-γ coincidences of both prompt and delayed γ rays and placed to feed the $9/2^-$ ground state. The angular distributions R_{exp} suggest quadrupole character for the 818, 634, 550 and 307 keV transitions for which the E2 multipolarity is again more probable. Although the values of R_{exp} for the 597, 620 and 624 keV transitions could not be extracted, they are also assigned an E2 character, resulting in a spin and parity of $I^\pi = (25/2^-)$ for the state at 2357 keV. The 198, 352, 245, 379 and 254 keV γ rays are measured to have dipole character and given the assigned E2 character of the crossover transitions they most likely have M1 multipolarity. On the basis of weak coincidences, the 670 and 538 keV transitions observed in the gated spectrum of prompt γ rays (Figure 4.7 (b)) are placed to feed the $(19/2^-)$ and $(21/2^-)$ levels at 1795 and 2050 keV, respectively.

The presence of the 307 keV line in the spectrum of prompt γ rays gated by other strong transitions in the cascade (Figure 4.7 (b)) implies that the microsecond isomer lies above the 2357 keV level and that the de-exciting transitions from this isomeric state remain unobserved. This non-observation is most probably due to the very low energy of these transitions, closely resembling the presumed de-excitation of the 12^+ isomeric state in the ^{192}Pb core [Lag91]. This suggested coupling of the $h_{9/2}$ proton to the 12^+ core state would yield a spin and parity of $I^\pi = (29/2^-)$ for the isomeric state in ^{193}Bi. In order to study γ rays feeding the $(29/2^-)$ state or the 2357 keV level directly, a spectrum of prompt γ rays gated by the delayed 307 keV transition was generated and is shown in Figure 4.7 (c). The 399, 356 and 289 keV lines are tentatively assigned to be M1 in character and placed to feed the isomeric level at $2357 + \Delta$ keV (Band 3 in Figure 4.6).

4.2.6 Non-collective structures

The energy spectrum of delayed γ rays gated by the 137 keV delayed transition is shown in Figure 4.7 (d) and the deduced irregular level structure is illustrated in Figure 4.6 (Group A). The assignment of these transitions to ^{193}Bi is based on the measured excitation function for the 137 keV transition (see Figure 4.4). The 1067 keV transition is present in the spectrum of recoil-gated prompt singles γ rays (Figure 4.5 (a)) and also in the spectrum of prompt γ rays gated by the delayed 605 keV $13/2^+ \rightarrow 9/2^-$ transition (Figure 4.5 (b)). Consequently, the 1067 keV γ ray is placed to feed the $13/2^+$ isomeric state and assigned to have an E2 character based on the measured angular distributions. The 436 and 455 keV transitions are in coincidence with the 1067 keV transition in both prompt and delayed γ-γ matrices and placed parallel to

each other feeding the $(17/2^+)$ state at 1672 keV. Inspection of the delayed γ-γ matrix reveals the presence of a 137 keV self-coincident doublet (Figure 4.7 (d)). On the basis of coincidences and energy sum arguments, one component of the 137 keV doublet together with the 930 keV transition is placed in the level scheme parallel to the 1067 keV transition. As the self-coincidence of the 137 keV transition or its coincidence with the 1067 keV transition are not observed in the prompt γ-γ matrix, it is likely that the second 137 keV component forms part of the fragmented de-excitation path from the long-lived isomer. The 718 keV transition is placed as a connecting transition to Band 2 from which the low-lying 620 and 818 keV transitions are also observed in Figure 4.7 (d). The 299 and 323 keV transitions present in this spectrum indicate feeding to Band 1 based on the $13/2^+$ state but discrete links could not be established. The half-life of the isomer is too long to be accurately measured in the present experiment where the time window for the observation of delayed γ rays after the implantation of a recoil is limited to 32 μs. The measured distribution of time differences suggests a lower limit of $\sim$10 μs for the half-life associated with the 137 keV transition.

4.2.7 Feeding of the $1/2^+$ intruder state

Prompt γ rays feeding the $1/2^+$ intruder state in ^{193}Bi were studied using the data collected at low beam current. The spectrum of singles γ rays gated by recoils and tagged with the 6475 keV α decay of the $1/2^+$ state using a search time of 9 s is displayed in Figure 4.8. As the structure appears to be irregular, γ-γ coincidences are essential in confirming the level sequence feeding the $1/2^+$ state. Unfortunately, the statistics in the α-tagged data is too low for a reliable coincidence analysis. Furthermore, coincidence spectra generated from recoil-gated data are contaminated due to the low population at the $1/2^+$ state compared with the total fusion cross section of the reaction. Therefore, the band structure feeding this state (Band 4 in Figure 4.6) remains tentative. The 200 keV transition, which is isotropic according to angular distribution measurements, is tentatively assigned to be of M1 character and placed to directly feed the $1/2^+$ state. The 230, (279), 509 and 505 keV transitions are placed into the level scheme on the basis of weak coincidence relations and energy sum arguments, whereas the location of the observed 355, 432, 459 and 469 keV transitions could not be resolved.

4.2.8 Other transitions

The 279 keV transition which is clearly observed in the spectrum of recoil-gated prompt singles γ rays (Figure 4.5 (a)) is firmly assigned to ^{193}Bi based on its measured excitation function (Figure 4.4). The analysis of the prompt γ-γ matrix revealed transitions with energies of 186, 252, 296, 299, 384, 551, 595, 634, 638 and 648 keV which

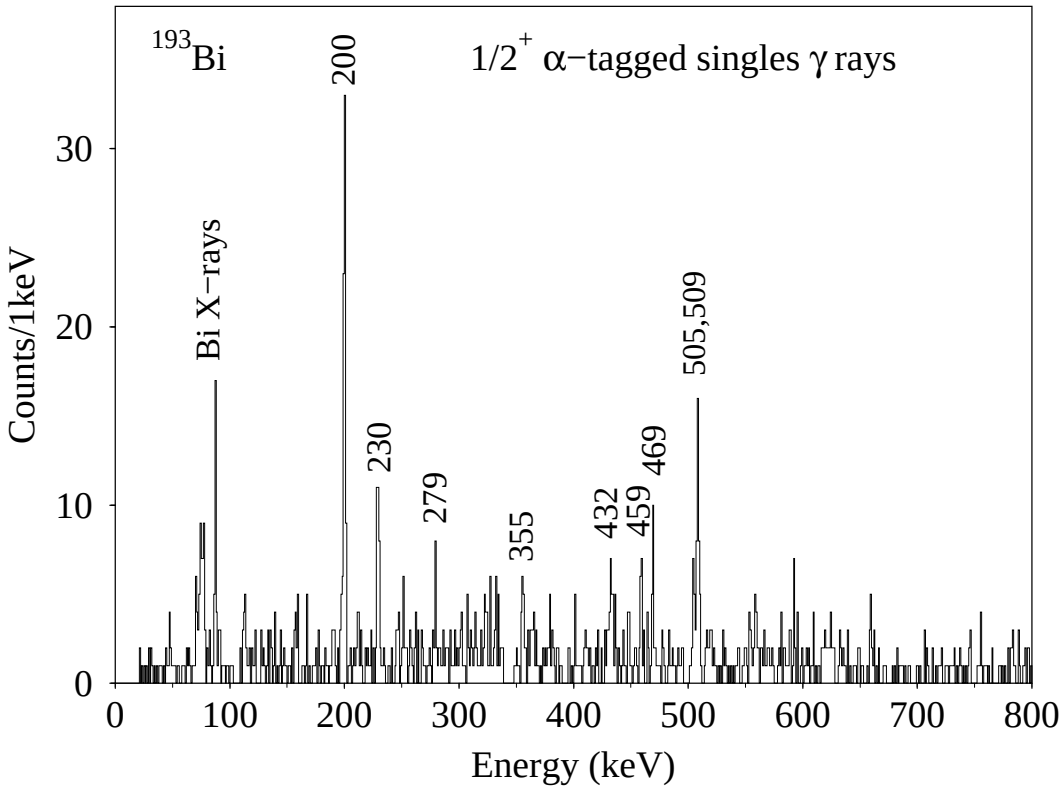

Figure 4.8: Energy spectrum prompt singles γ rays gated by recoils and tagged with the 6475 keV α decay of the $1/2^+$ intruder state in ^{193}Bi.

are all associated with ^{193}Bi. Angular distribution measurements imply quadrupole character for the 279 keV transition while values of R_{exp} for the other members of the group could not be extracted due to strong overlapping lines. The link between this group (Group B in Figure 4.6) and the rest of the level scheme could not be established from the present data. As prompt feeding to the band head (spin j in Figure 4.6) is strong, the non-observation of the de-exciting transitions suggests an isomeric character of this state. The associated half-life would then be such that the depopulation proceeds while the ^{193}Bi recoils travel through the separator. In this scenario, the lower limit for the half-life would be close to the $\sim$20 ns of the 12^+ state in ^{190}Pb from which the de-exciting transitions appear to have very low intensity in data collected with the present experimental system (see Section 2.6, [Jon99]). The observed intensity of prompt feeding to this state is roughly 30% of that of the $13/2^+$ isomeric state which having a half-life of $t_{1/2} = 153$ ns turned out to be close to the performance limit of the isomer tagging technique. Thus, if the assumption of an unobserved isomeric state is correct, its half-life will probably be shorter than 150 ns.

4.3 ^{191}Bi

The ^{191}Bi nuclei were produced in the ^{142}Nd(^{52}Cr,$p2n$) reaction at a beam energy of 235 MeV in the centre of the 470 μg/cm^2 thick ^{142}Nd target (99.8% enrichment). The target was evaporated onto a carbon backing of 50 μg/cm^2 thickness and covered with a 10 μg/cm^2 thick layer of carbon. The approximate average beam current during the 130 hours of bombardment was limited to 12 pnA by the singles counting rate in the Ge detectors.

4.3.1 Production rates and α spectrum

For the bismuth isotopes with $N < 110$, the properties of α-decaying states become more suited to exploitation by tagging techniques. The α-decay branches gain dominance over β decay and the decay halflives become shorter allowing the use of higher beam currents which partly compensates the lower production cross sections in the lighter isotopes.

The α-decay properties of ^{191}Bi are mainly adopted from the work of Kettunen *et al.* [Ket03b]. The total α-decay branch from the $9/2^-$ ground state is $b_\alpha = 51(10)\%$ but the measured half-life of $t_{1/2} = 12.4(4)$ s is too long for an unambiguous identification of prompt γ rays based on recoil-α correlations. During the experiment, the two α-decay channels from this state, having $E_\alpha = 6308(3)$ keV with an intensity of $I_\alpha = 97.1(3)\%$ [Fir96] and $E_\alpha = 6639(5)$ keV [Fir96] with $I_\alpha = 2.9(3)\%$ [Fir96] yielded approximately 380000 full-energy events in the singles α-particle energy spectrum shown in Figure 4.9. The Po isotopes with $A \geq 193$ are produced in the fusion of the ^{52}Cr beam with the heavier Nd isotopes contaminating the target.

The $1/2^+$ intruder state lying at an excitation energy of 242 keV [Fir96] has an α-decay branch of $b_\alpha = 68(5)\%$ and a half-life of $t_{1/2} = 121^{+8}_{-7}$ ms which is sufficiently short to allow the use of the RDT method in the identification of γ rays. Approximately 65000 α decays from the $1/2^+$ state with a characteristic energy of $E_\alpha = 6870(3)$ keV were observed during the experiment.

A cross section of ~ 150 μb was extracted for the ^{142}Nd(^{52}Cr,$p2n$)^{191}Bi reaction at 235 MeV by adopting the same detection and transmission efficiencies as in the ^{193}Bi experiment and taking into account the Si-detector coverage of 70% of the ^{191}Bi recoil distribution. Since the excitation energy of the $1/2^+$ intruder state decreases in going from ^{193}Bi to ^{191}Bi, the feeding of this state is increased reaching 12% of the total production cross section for ^{191}Bi, compared with the 2-4% fractions which were measured for ^{193}Bi.

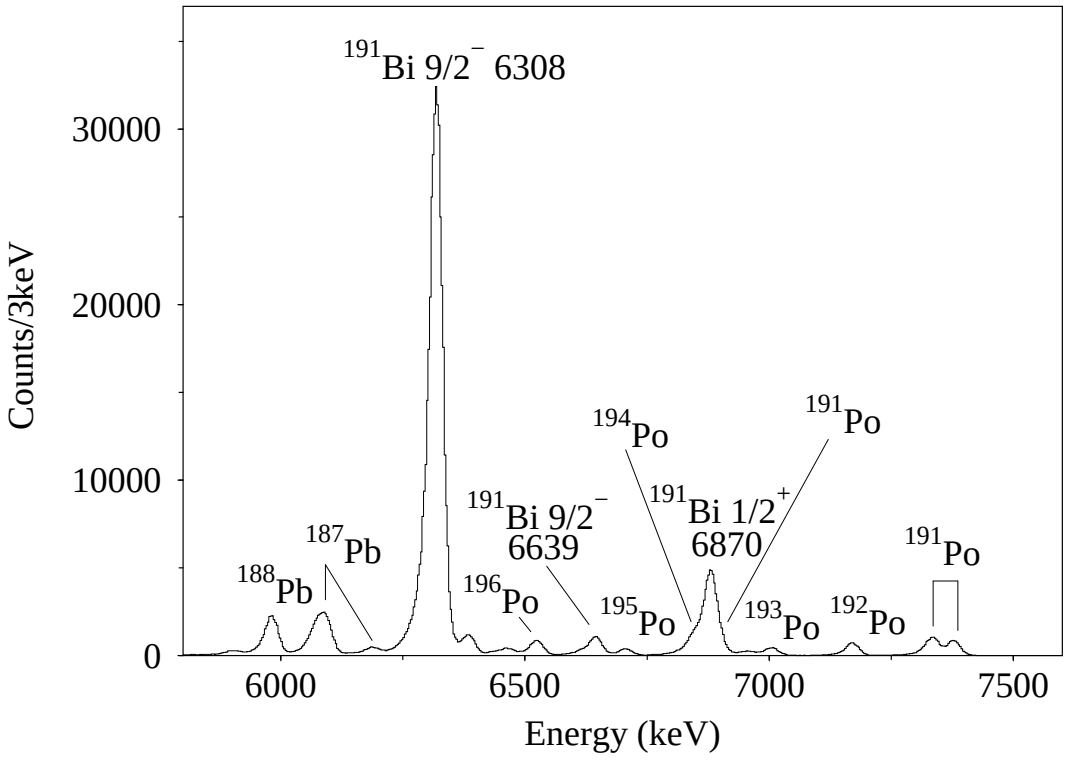

Figure 4.9: Energy spectrum of α particles observed in the focal-plane Si detector from the ^{52}Cr + ^{142}Nd reactions. The gas counter veto is present. The Po isotopes with $A \geq 193$ are produced in reactions with the heavier Nd isotopes contaminating the target.

4.3.2 Identification of the $13/2^+ \rightarrow 9/2^-$ transition

Assuming that the depopulation of the $13/2^+$ isomeric state in ^{191}Bi follows the same de-excitation path as in ^{195}Bi and ^{193}Bi, the first step in the data analysis for ^{191}Bi is again the identification of the $13/2^+ \rightarrow 9/2^-$ transition. Following the systematics for the excitation energy of this isomeric state, it would be expected to lie approximately at 400 keV in ^{191}Bi. If the transition strength is similar to that measured in ^{193}Bi, the decrease in excitation energy would correspond to a longer half-life for the $13/2^+$ state and the de-exciting M2 γ-ray transition is likely to be observed in the focal-plane Ge detectors.

The energy spectrum of delayed γ rays gated by recoils and tagged with the α decay of the $9/2^-$ ground state using a search time of 13 s is shown in Figure 4.10. Despite the long α-decay half-life, the resulting spectrum is clean containing a very strong peak at an energy of 430 keV together with a few weaker lines. The half-life associated with the 430 keV transition was measured to be $t_{1/2} = 562(10)$ ns from the distribution of time differences between the recoil implantation and the observation of a 430 keV γ

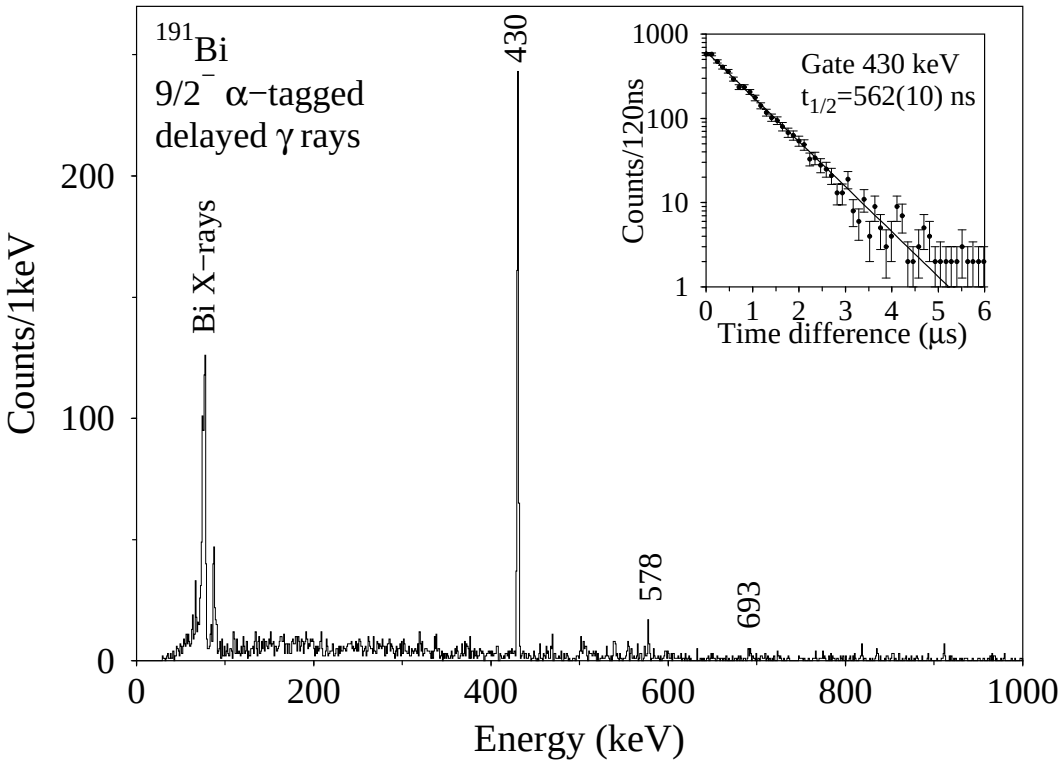

Figure 4.10: Energy spectrum of recoil-gated delayed γ rays tagged with the α decay of the $9/2^-$ ground state in ^{191}Bi. In the inset, spectrum of time differences between the implantation of a recoil and the observation of a 430 keV γ ray in the focal-plane Ge detectors is presented.

ray in the focal-plane Ge detectors (see the inset of Figure 4.10). The corresponding transition strength was calculated assuming that a level at 430 keV de-excites only via the 430 keV transition. The resulting value of $B(M2) = 0.073(5)$ W.u. is comparable with that of the $13/2^+ \rightarrow 9/2^-$ transition in ^{193}Bi ($B(M2) = 0.062(10)$ W.u.). Moreover, the observed intensity of bismuth K X-rays in Figure 4.10 can be accounted for only if M2 character is assumed for the 430 keV γ ray. Excluding the weak lines in the spectrum, the observed γ-ray and bismuth K X-ray intensities yield a conversion coefficient of $\alpha_K = 0.61 \pm 0.10$ for the 430 keV transition while calculations for the two lowest multipoles give $\alpha_K(E1) = 0.013$, $\alpha_K(E2) = 0.030$, $\alpha_K(M1) = 0.15$ and $\alpha_K(M2) = 0.44$ [Ros78]. Therefore, the 430 keV transition is firmly assigned to be the $13/2^+ \rightarrow 9/2^-$ transition in ^{191}Bi.

4.3.3 Band feeding the $13/2^+$ state

In order to examine prompt γ rays feeding the $13/2^+$ isomeric state in ^{191}Bi, a recoil-gated delayed-prompt γ-γ matrix was generated and the isomer tagging method was

applied. In this analysis, a spectrum of prompt γ rays in coincidence with the delayed 430 keV transition was created and is presented in Figure 4.11 (a). This spectrum shows an arrangement of transitions into two groups as in the coincidence spectrum for ^{193}Bi (see Figure 4.5 (c)), again clearly indicating the observation of a strongly coupled band. The 318 keV transition is placed to directly feed the $13/2^+$ isomeric state as it is the most intense peak in the spectrum and similar in energy to the 323 keV $15/2^+ \rightarrow 13/2^+$ transition in ^{193}Bi. The rest of the band feeding the $13/2^+$ level (Band 1 in Figure 4.12) was constructed from a γ-γ coincidence analysis of a recoil-gated prompt γ-γ matrix, from which a sample coincidence spectrum gated by the 318 keV transition is presented in Figure 4.11 (b).

To determine the multipolarities of the observed transitions, their angular distributions were extracted as the intensity ratio $R_{exp} = I(134°, 158°)/I(79°, 101°)$ in spectra of recoil-gated γ rays. The obtained values, listed in Table 4.2 along with γ-ray energies and intensities of transitions assigned to ^{191}Bi, support dipole character for the 318, 279, 325 and 248 keV transitions belonging to the strongly coupled band. An M1 assignment for these four γ rays is again more probable. The angular distribution measurements also indicate quadrupole character for the 573 keV transition, whereas values of R_{exp} for the 597 and 604 keV γ rays could not be extracted due to the many overlapping lines close to 600 keV. However, these three transitions are assigned to be of E2 multipolarity based on their crossover character within the band. The 385 keV dipole transition tentatively defining a $(21/2^+)$ level at 1736 keV, the 710 keV transition linking this state to the $17/2^+$ state of Band 1 and the 509 keV γ ray all are placed in the level scheme based on γ-γ coincidences.

4.3.4 Negative-parity states

A spectrum of recoil-gated prompt γ rays tagged with the α decay of the $9/2^-$ ground state using a search time of 13 s is presented in Figure 4.11 (c). As the recoil rate in the Si detector was high relative to the half-life of 12.4 s of this state, an unambiguous identification of γ rays directly feeding the $9/2^-$ ground state in ^{191}Bi is not possible. However, despite the large number of random recoil-α correlations, some of the observed γ rays can be assigned to ^{191}Bi. The 578 and 693 keV transitions are present also in the spectrum of delayed γ rays (Figure 4.10) where the α-tagging procedure has significantly enhanced their intensity compared to contaminating lines originating from lead isotopes. These two transitions, together with γ rays having energies of 486, 207, 532, 325 and (599) keV are placed in a band feeding the $9/2^-$ ground state (Band 2 in Figure 4.12). Angular distribution measurements indicate dipole and quadrupole character for the 486 and 693 keV transitions, respectively, while the R_{exp} ratios for the other band members could not be determined. This negative-parity structure resembles the band feeding the $9/2^-$ ground state in ^{193}Bi, including an isomeric state

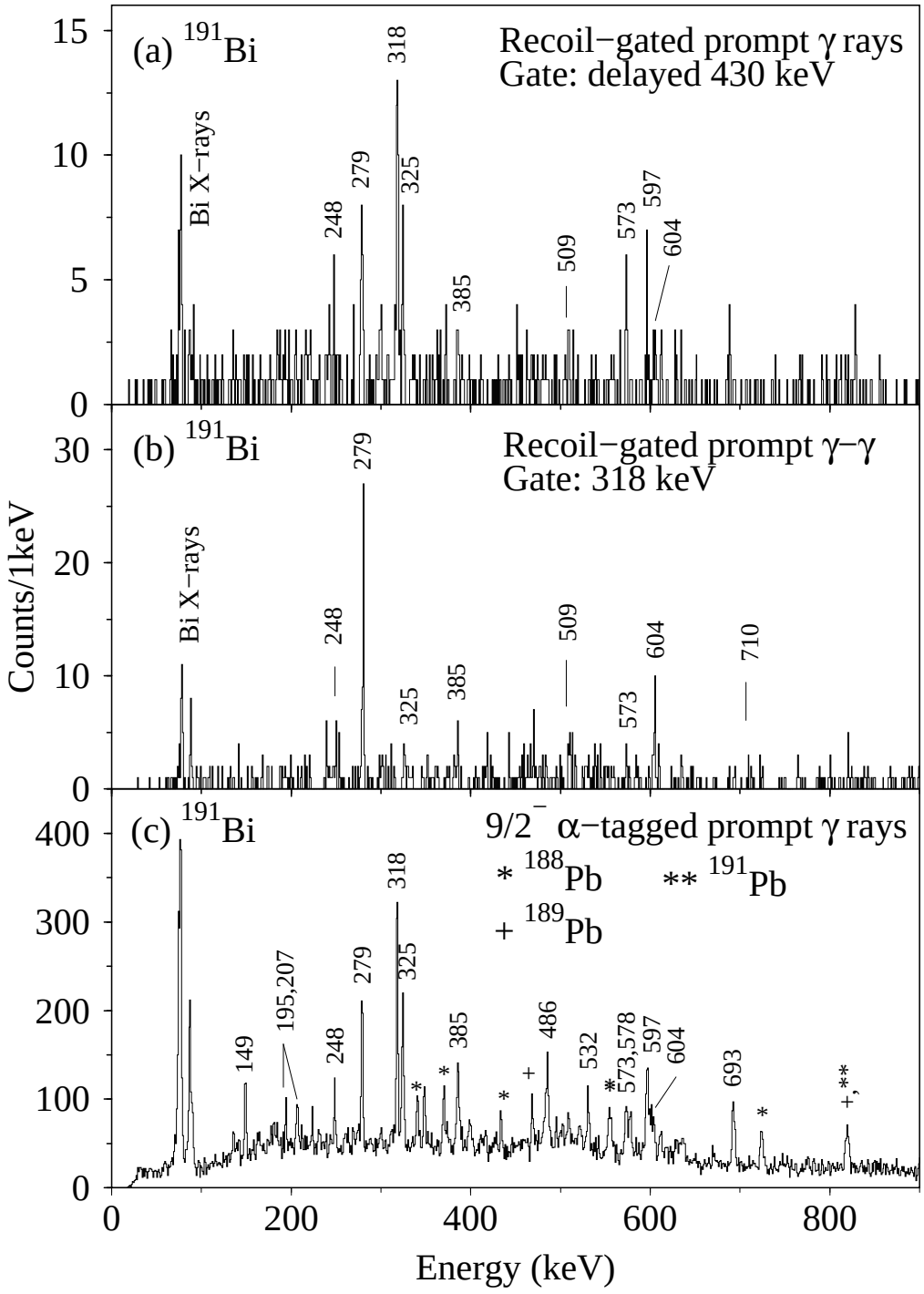

Figure 4.11: (a) Energy spectrum of recoil-gated prompt γ rays from the ^{52}Cr + ^{142}Nd reactions gated by the 430 keV delayed transition. (b) Spectrum of recoil-gated prompt γ rays gated by the 318 keV transition. (c) Spectrum of prompt γ rays gated by recoils and tagged with the 6308 keV α decay of the $9/2^-$ ground state in ^{191}Bi. The identified peaks from background activities are marked with their nucleus of origin.

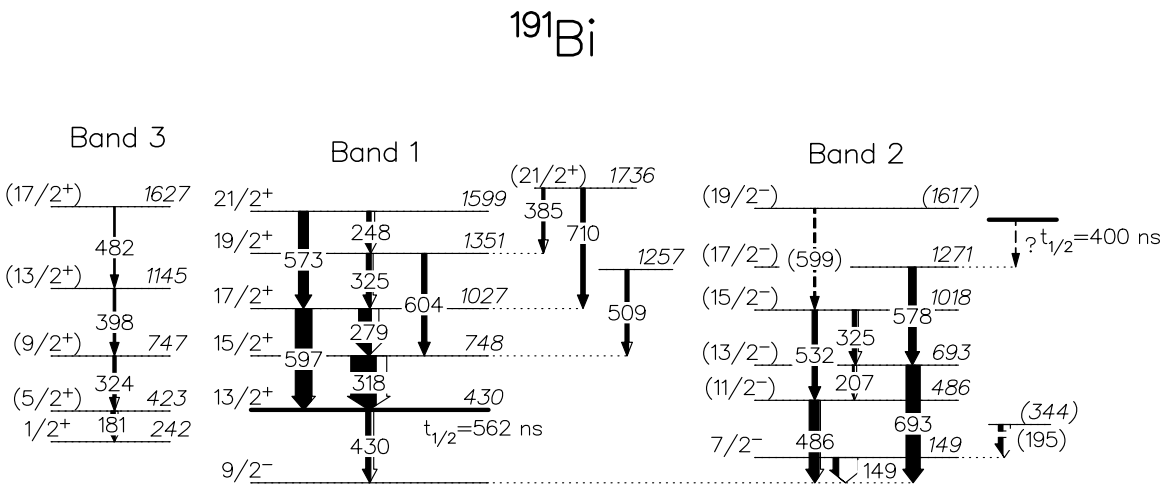

Figure 4.12: Level scheme of ^{191}Bi.

for which a half-life of $t_{1/2} = 400(40)$ ns is extracted using the time differences between the recoil implantation and observation of the 578 keV γ ray. However, the direct de-excitation of the isomeric state is not observed and prompt γ rays feeding this state cannot be resolved as the population intensity is weak and the half-life is short compared to the flight time of the ^{191}Bi recoils through the RITU separator.

The 149 keV transition (Figure 4.11 (c)) is found to follow the α-decay of the mother nucleus ^{195}At [Ket03b] and placed to directly feed the $9/2^-$ ground state in ^{191}Bi. The measured α-decay hindrance factor favours a spin and parity assignment of $I^\pi = 7/2^-$ for the 149 keV level. Furthermore, the absence of a transition from the $13/2^+$ state to the level at 149 keV is in agreement with a spin value less than 9/2. The 195 keV transition is tentatively placed to feed the $7/2^-$ state based on weak γ-γ coincidences.

4.3.5 Feeding of the $1/2^+$ intruder state

Gamma rays feeding the $1/2^+$ intruder state in ^{191}Bi were identified using the RDT method. The 6870 keV α decay of this state has a half-life of 121 ms which is sufficiently short to allow unambiguous recoil-α correlations at the present implantation rate. However, the focal-plane Si detector with its energy resolution of $\sim$30 keV in this experiment could not separate the 6870 keV α decay from the overlapping lines originating from ^{191}Po and ^{194}Po. The α-decay properties and excited states of ^{191}Po were studied in the present experiment and are reported in Reference [And02b]. The half-life of the α-decaying $13/2^+$ state in ^{191}Po is 93(3) ms and the two main decay branches from this state have energies of $E_\alpha = 7376(5)$ keV with an intensity of $I_\alpha = 47.6(1.5)\%$ and $E_\alpha = 6888(5)$ keV with $I_\alpha = 38(8)\%$. The α-decay energy of

Table 4.2: The γ-ray energies, intensities and angular distribution ratios for transitions assigned to ^{191}Bi.

E_γ (keV)	I_γ (%)	E_i (keV)	I_i^π	I_f^π	$R_{exp} = I(134°, 158°)/I(79°, 101°)$
149.0(5)	22(3)	149	$7/2^-$	$9/2^-$	0.91(12)
180.9(7)	17(3)	423	$(5/2^+)$	$1/2^+$	0.9(2)
187.0(7)	6(2)				
194.7(7)	18(5)	(344)		$7/2^-$	0.8(2)
207.1(7)	7(4)	693	$(13/2^-)$	$(11/2^-)$	
248.2(7)	17(5)	1599	$21/2^+$	$19/2^+$	0.8(2)
278.6(5)	50(5)	1027	$17/2^+$	$15/2^+$	0.76(8)
297.2(7)	3(1)				
318.3(5)	100(10)	748	$15/2^+$	$13/2^+$	0.78(7)
324.2(7)	11(3)	747	$(9/2^+)$	$(5/2^+)$	
324.6(7)	17(9)	1018	$(15/2^-)$	$(13/2^-)$	
324.8(5)	19(7)	1351	$19/2^+$	$17/2^+$	0.81(8)
344.0(7)	3(1)				
368.6(7)	5(2)				
385(1)	10(5)	1736	$(21/2^+)$	$19/2^+$	0.92(9)
397.6(7)	9(3)	1145	$(13/2^+)$	$(9/2^+)$	
429.7(5)		430	$13/2^+$	$9/2^-$	
459(1)	3(1)				
482(1)	6(2)	1627	$(17/2^+)$	$(13/2^+)$	
486.0(5)	39(6)	486	$(11/2^-)$	$9/2^-$	0.7(2)
509(1)	14(7)	1257		$15/2^+$	
527(1)	3(1)				
532(1)	20(6)	1018	$(15/2^-)$	$(11/2^-)$	
544(1)	3(1)				
553(1)	3(1)				
572.8(7)	38(11)	1599	$21/2^+$	$17/2^+$	1.1(2)
578.0(7)	29(5)	1271	$(17/2^-)$	$(13/2^-)$	1.9(4)
597.0(7)	63(10)	1027	$17/2^+$	$13/2^+$	
599.1(7)	8(4)	(1617)	$(19/2^-)$	$(15/2^-)$	
603.7(7)	20(6)	1351	$19/2^+$	$15/2^+$	
693.1(7)	55(8)	693	$(13/2^-)$	$9/2^-$	1.1(2)
710(1)	17(8)	1736	$(21/2^+)$	$17/2^+$	

^{194}Po is $E_\alpha = 6842(6)$ keV and the half-life 0.392(4) s [Wau93]. In order to distinguish γ rays originating from ^{191}Bi, a background spectrum of γ rays in ^{191}Po correlated with the 7376 keV α decay was generated. Figure 4.13 shows a spectrum of γ rays tagged with the α decay of the $1/2^+$ state in ^{191}Bi using a search time of 360 ms following the subtraction of the ^{191}Po background spectrum. The lines from the other contaminating isotope ^{194}Po at 320, 367 and 462 keV [Hel99] are just visible.

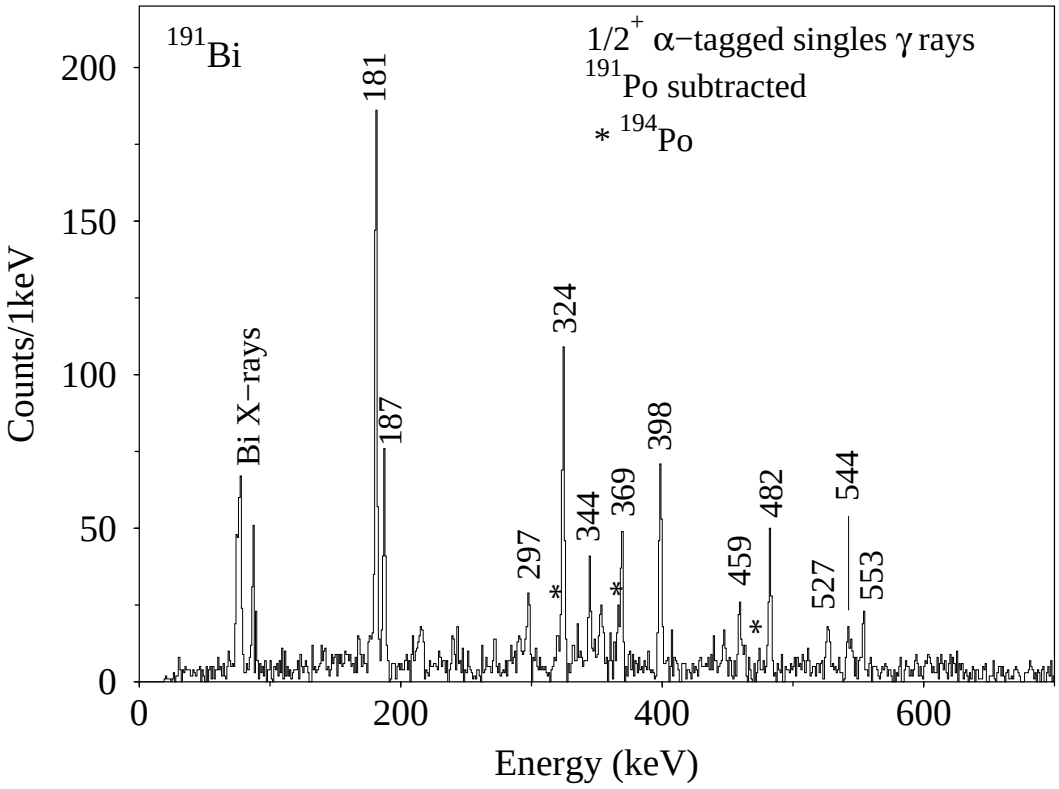

Figure 4.13: Gamma-ray singles spectrum gated by recoils and tagged with the 6870 keV α decay of the $1/2^+$ intruder state in ^{191}Bi. The contaminating γ rays from ^{191}Po have been subtracted and those originating from ^{194}Po are indicated with asterisks.

The 181, 324, 398 and 482 keV transitions are assigned to ^{191}Bi and placed in the level scheme (Band 3 in Figure 4.12) on the basis of weak γ-γ coincidences and intensity arguments. As the angular distributions of γ rays from low-spin states are expected to be rather isotropic and the statistics is low, an R_{exp} value can only be extracted for the 181 keV γ ray. Even if the obtained value of 0.9(2) for this transition weakly favours a $\Delta I = 1$ assignment, the examination of the X rays in Figure 4.13 revealed that a 181 keV M1 transition would exhaust 80-90 % of the observed X-ray intensity which seems an unrealistically large fraction. Therefore, the γ rays placed to feed the $1/2^+$ state are assumed to be of stretched E2 character. The location of the 187, 297, 344, 369, 459, 527, 544 and 553 keV transitions in the level scheme could not be resolved.

5 Discussion

Interpretation of the present data for ^{191,193}Bi is carried out by comparing the obtained experimental results to those for neighbouring nuclei and to theoretical predictions which can be calculated for some observable quantities. The coexistence of various nuclear shapes has been well established in the light Hg, Tl, Pb and Po isotopes via α- and β-decay studies and more recently by the observation of collective bands. These deformed structures are closely related to those found to evolve in the neutron-deficient bismuth nuclei. The first description of the α-decaying $9/2^-$ ground states and $1/2^+$ intruder states in odd-A Bi isotopes derives from their decay properties and similarly, the characteristics of γ-ray transitions de-exciting the $13/2^+$ isomeric states provide information on the intrinsic structure of these isomers. In the present work, these three low-lying configurations in ^{191,193}Bi are discussed in terms of Total Routhian Surface (TRS) calculations which reveal their location in the $\beta_2-\gamma$ deformation plane and also predict other potential minima at higher excitation energies. The nature of the deformed structures is examined by extracting aligned angular momenta and moments of inertia for the collective bands feeding these states. The experimental $B(M1)/B(E2)$ ratios for the observed strongly coupled bands are compared to theoretical predictions in order to confirm the intrinsic configurations. The discussion of level energy systematics of the odd-A bismuth isotopes focuses on the coupling of the odd proton to the even-even lead core and the structure of the observed high-spin isomers. The results of the present work for ^{191,193}Bi have been partly reported in References [Nie01, Nie03a] and will be discussed in more detail in Reference [Nie03b].

5.1 Intruder structures in the light lead region

The bismuth isotopes lie in the lead region where the competition between various nuclear shapes in the neutron-deficient nuclei is initiated by the elevation of one or more protons across the $Z = 82$ shell gap [Hey83, Woo92]. Near the closed $N = 126$ neutron shell, only few of these proton particle-hole configurations have been observed as having high excitation energies since the spherical shell gap in this mass region is of the order of four MeV. In the neutron mid-shell region, the combined effect of pairing interactions and the large energy gain from the residual proton-neutron interaction between the proton particle-hole configurations and valence neutrons can overcome this large energy gap. The resulting structures are deformed and suppressed to low

excitation energies so that they are expected to reach their minimum in energy close to $N = 104$ where the total contribution of the interactions is maximised [Hey87, Hey88]. A parallel interpretation of the deformed structures can be obtained by calculating the single-particle energies in a deformed nuclear potential which results in the disappearance of shell gaps as defined for spherical shape and low excitation energies for the particle-hole configurations [Nil55]. In the following section, the intruder structures in the neutron-deficient even-A Hg, Pb and Po and in the odd-A Tl nuclei, relevant to the discussion of the present work are reviewed.

5.1.1 Even-even nuclei

In even-even nuclei in the light lead region, the observed intruder structures are associated with the excitation of one or more proton pairs across the $Z = 82$ shell gap and hence they all have a spin and parity of $I^\pi = 0^+$. The depopulation of the excited 0^+ states typically proceeds via an E2 transition to a lower-lying 2^+ state or through an E0 transition to lower-lying 0^+ states. As the typical result in a γ-ray spectroscopic measurement for a deformed exotic even-even nucleus is a low-lying collective band having a mixed character, the observation of the 0^+ band heads of the excited component structures is not possible. Besides in-beam electron spectroscopy, the only method to directly access these excited 0^+ states is via α-decay measurements. As the decay of a light even-even nucleus in the lead region typically proceeds via α-particle emission from its 0^+ ground state to the 0^+ ground and intruder states in the daughter nucleus, the fine structure in the α decay reveals the relative energies of the populated states in the decay daughter. The states can be classified according to the hindrance factor (HF) of the connecting α decay [Ras59, Pre47] so that a value of HF < 4 indicates the same spin, parity and in particular, the same intrinsic configuration for the initial and final states. However, more precise information, for example on the degree of deformation, can be derived from the properties of the observed collective band.

Configurations and shapes assigned to states in the light even-even nuclei in the lead region seem to suggest that oblate deformation results when there are two holes in the $Z = 82$ proton shell. This is the case for the $0p-2h$ ground states of the even-even Hg isotopes which have been observed to preserve an oblate shape with decreasing neutron number until beyond the mid-shell, where a transition towards sphericity is predicted [Naz93] and now also experimentally observed [Car97, Mui98]. The properties of the oblate ground-state band remain constant down to ^{188}Hg where it is observed to be crossed by a more-deformed band which is associated with a prolate shape [Woo92] and minimises its energy in ^{182}Hg [Dra88]. In general, prolate deformation is presumably a result from more complex particle-hole configurations with four or more hole states in the $Z = 82$ major shell, in the mercury isotopes a $4p-6h$ configuration is assumed [Woo92, Naz93]. In Pb isotopes, the closed proton shell at $Z = 82$ stabilises the

ground state so that it remains nearly spherical through the whole neutron $82 < N < 126$ shell. An intruder 0^+ state, assigned to an oblate $2p-2h$ configuration has been observed to lie below 2 MeV in excitation energy in lead isotopes with $190 \leq A \leq 200$ (see [Jul01] and references therein). In α-decay studies, two low-lying excited 0^+ states, the oblate and a more-deformed prolate have been observed in ^{188}Pb [All98] and ^{186}Pb [And00]. The identification of prolate band structures in ^{188,186}Pb [Bax93, Hee93] is based on similarities with the prolate-deformed bands established in their corresponding isotones, ^{186,184}Hg. In ^{184}Pb, a candidate for the presumed prolate 0^+ state has been found in α-decay studies [And99] and the observed collective band has been associated with a prolate-deformed shape [Coc98]. When going towards the neutron-deficient even-A polonium isotopes, collective low-lying structures emerge in ^{198,196}Po [Ber95] and the collective bands observed in ^{194,192}Po have been associated with the $4p-2h$ intruder structure [Hel96, Hel99]. The trend of decreasing excitation energy of this oblate-deformed configuration with decreasing N results in an increasing oblate component in the ground state of light polonium isotopes which becomes dominant in ^{192}Po [Hel99]. In ^{190}Po, the oblate ground-state band is crossed at spin $I = 4$ by a prolate band with a presumed $6p-4h$ intruder configuration [Vel03]. In the lighter polonium isotopes, the ground state is predicted to become prolate [Oro99].

5.1.2 Odd-even nuclei

In odd-even nuclei, the de-excitation paths from intruder states are in general more diverse compared to those in the even-even isotopes. The spins and parities of the configurations are dictated by the orbital of the odd proton or hole state and the most favoured decay path depends on the location and nature of other close-lying states. The halflives of excited 0^+ states in heavy neutron-deficient even-even nuclei may well be in the picosecond range whereas due to their versatile properties, intruder states in their odd-Z neighbours may survive for several seconds. The longest of these halflives are usually connected to α-decaying shape isomers and provide favourable conditions for the direct identification of the state by the correlation methods outlined in the present work. Another consequence of the different spins, parities and intrinsic configurations of the intruder states in odd-A nuclei is the observation of separate collective bands rather than a mixed ground-state band as typically measured in the very light even-even isotopes. However, the identification of α-decaying states obeys the same rules as in the even-even nuclei. The spin and parity assignments can be made for structures belonging to a chain of states which are connected via an unhindered α decay and terminate at a state whose spin and parity have been directly measured.

Intruder structures in odd-even nuclei are closely related to states in their neighbouring even-even isotones through a description where the odd proton particle or hole

state is coupled to the core configuration. These similarities may indicate the shape associated with the particle-hole configuration in the odd-A nucleus, provided that the structure of the core is not influenced by the odd particle or the hole state. Moreover, a collective band observed in an odd-A nucleus may reveal information on the contribution of its characteristic orbital in the structure of the deformed minimum of the even-even core, as outlined for the Tl and Hg isotopes in Reference [Lan95].

Experimental mapping of intruder structures in odd-even nuclei is not as comprehensive as for the even-even isotopes. The most extensive data to date in nuclei with $Z > 80$ have been collected for the neutron-deficient odd-A Tl isotopes. Their presumably spherical ground states have been assigned a spin and parity of $1/2^+$ corresponding to a proton in the $s_{1/2}$ orbital (a $0p - 1h$ structure). Isomeric $9/2^-$ states, first found in the $^{193-199}$Tl isotopes by Diamond and Stephens [Dia63], are interpreted as having a $1p - 2h$ intruder configuration with the odd proton in the $h_{9/2}$ orbital above the $Z = 82$ shell gap [New70]. Due to the preferred population of high-spin states in fusion-evaporation reactions, bands characterised by a proton in a high-j orbital are the main features appearing in the level schemes for the neutron-deficient thallium isotopes. In ^{191}Tl, oblate bands from both $h_{9/2}$ and $i_{13/2}$ proton configurations have been established [Rev95]. In ^{189}Tl, low-lying $h_{9/2}$ and $i_{13/2}$ bands from the coupling of the odd proton to the oblate ground state of ^{188}Hg are observed, the latter showing a structural change between spins $17/2^+$ and $21/2^+$. As the level sequence above the $21/2^+$ state resembles the prolate band in ^{188}Hg, this change has been tentatively associated with a crossing of an oblate and a decoupled prolate $\pi i_{13/2}$ band with a presumed $5p - 6h$ configuration [Kre88]. In the lighter isotopes, prolate-deformed bands from the $h_{9/2}$, $i_{13/2}$ and $f_{7/2}$ proton orbitals dominate the structure of ^{187}Tl where the beginnings of the non-yrast oblate $\pi i_{13/2}$ band are also observed. In ^{185}Tl, the prolate $\pi i_{13/2}$ structure is accompanied by a tentatively assigned prolate $\pi h_{9/2}$ band [Lan95] and in ^{183}Tl, a prolate $\pi i_{13/2}$ yrast band and a candidate for the $(11/2^-)$ level from the $\pi(h_{11/2})^{-1}$ configuration have been observed [Mui01].

5.2 Characteristic structures in odd-A bismuth isotopes

The features dominating the level schemes for ^{193}Bi and ^{191}Bi are the collective bands feeding the $13/2^+$ and $9/2^-$ states and the structures based on the $1/2^+$ intruder states. The nature of each band-head configuration is discussed in terms of established systematic trends.

5.2.1 $9/2^-$ ground states

The ground-state spin and parity of an odd-even nucleus are controlled by the orbital which the odd proton occupies. The energies of these single-particle levels as a function of deformation have been calculated for ^{191}Bi using the Woods-Saxon potential with universal parameters and are presented in Figure 5.1. This figure, which also shows the Fermi surface indicating the division between occupied and unoccupied states, suggests an $h_{9/2}$ character for a nearly spherical ground state in this nucleus. The ground-state spin and parity of $9/2^-$ for the neutron-deficient odd-A bismuth isotopes down to ^{187}Bi has been experimentally confirmed by α-decay studies and corresponds to a deformation in the range of $-0.12 \lesssim \beta_2 \lesssim 0.15$ in ^{191}Bi (Figure 5.1).

According to recent shell-model calculations where the ground states of the odd-A Bi isotopes are described by a proton in the potential of the even-even Pb core, the assumption of sphericity appears to be valid down to $A = 193$ [Hür02]. In lighter isotopes, proton binding energies extracted from the mass-measurement data [Rad00, Nov02] deviate from the prediction given by the calculations implying a stronger binding for the proton in the $h_{9/2}$ orbital than expected. This effect is presumed to be due to the onset of deformation [Hür02] thus indicating the influence of the odd proton in polarising the magic lead core. For comparison, the ground states of the odd-A astatine ($Z = 85$) isotopes have $I^\pi = 9/2^-$ down to ^{197}At until in ^{195}At, a change to a slightly oblate-deformed $1/2^+$ state from the intruder $4p-1h$ proton configuration is observed [Ket03b, Ket03c]. This change is manifested as a kink in a plot of proton binding energies calculated in the potential of the even-even core, the behaviour of which is similar to that observed in the very light odd-A bismuth isotopes. This would suggest that even though the ground-state spin and parity remain as $9/2^-$ down to ^{187}Bi, the increased stability in going towards the neutron mid-shell indeed arises from effects of deformation. However, it should be noted that this approach may suffer from systematic errors in mass measurements which for example could originate from the existence of low-lying isomeric states.

In the present work, strong evidence for a deformed configuration involving the $h_{9/2}$ proton in ^{193}Bi and ^{191}Bi was obtained via the observation of a low-lying strongly coupled negative-parity band. It is likely that this band would be based on a particle in a high-Ω orbital and Figure 5.1 suggests an oblate shape. However, the maximum oblate deformation of $\beta_2 \approx -0.12$ which still produces the experimentally deduced spin and parity for the ground state is not sufficiently large to account for the rotational-like level pattern. As oblate-deformed intruder structures are known in the Pb core nuclei, a natural explanation for such a collective band would be a coupling of the odd proton to the oblate 0^+ $2p-2h$ proton excitation of the core, instead of the spherical 0^+ configuration. In that case, the deformed band head would probably lie close above the $9/2^-$ ground state and remain unobserved in the present experiment.

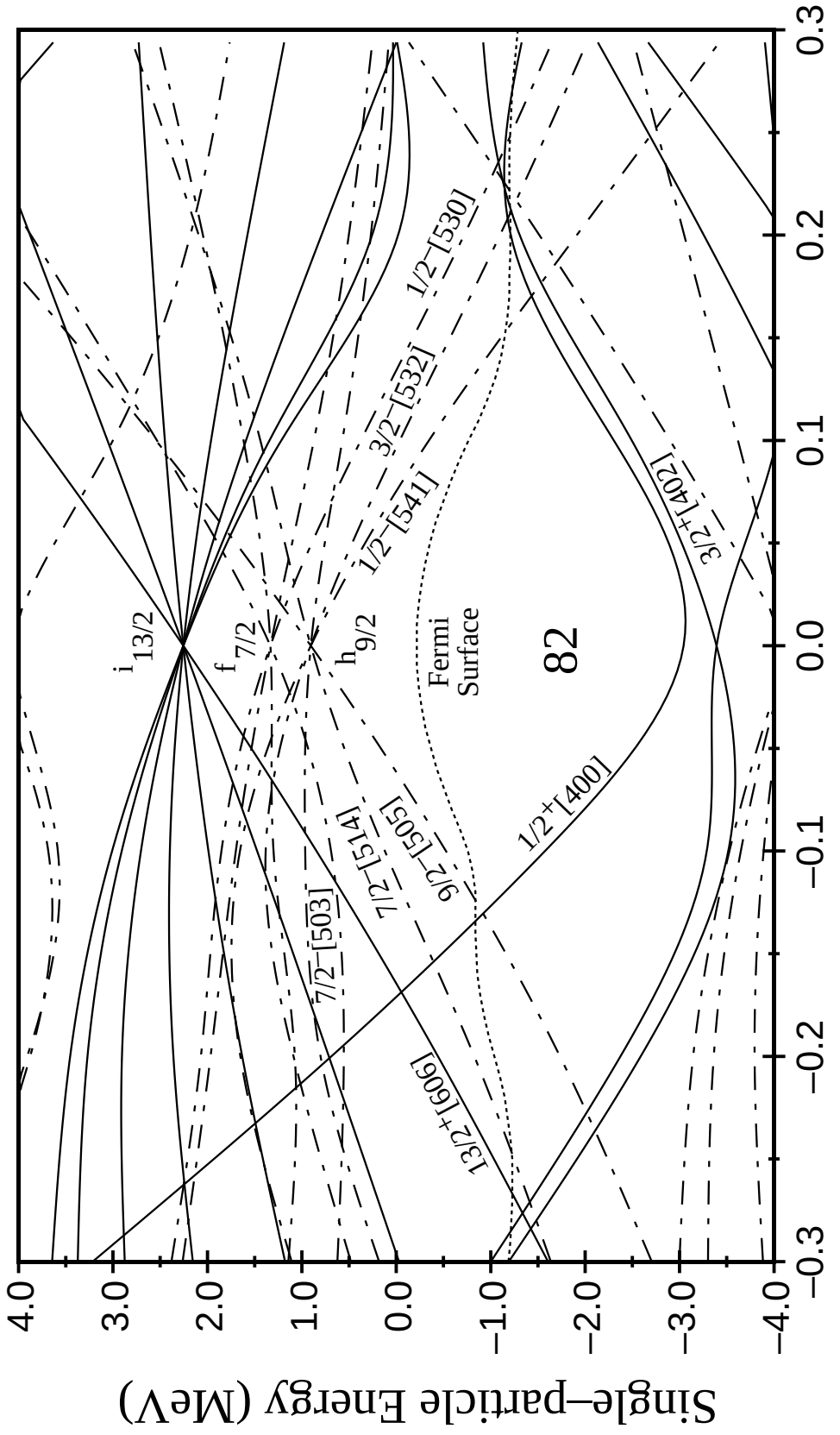

Figure 5.1: Proton single-particle levels in ^{191}Bi calculated using the Woods-Saxon potential. Positive-parity states are drawn with solid lines and negative-parity states with dashed lines. The calculated Fermi Surface is indicated with a dotted line.

5.2.2 $2p-1h$ intruder states

The potential $2p-1h$ excitations in the neutron-deficient odd-A bismuth isotopes are created by elevating a proton across the $Z = 82$ gap and characterised by a hole in the $s_{1/2}$, $d_{3/2}$, $h_{11/2}$, $d_{5/2}$ or $g_{7/2}$ orbital forming the $50 < Z < 82$ shell. Out of these, the $1/2^+$ state is observed down to the last known odd-A isotope ^{185}Bi and low-lying $3/2^+$ and $5/2^+$ states presumably having this intruder character have been established in $^{199-207}$Bi [Hey83, Coe85, Ket03a, Ket03b, Alp69, Bra80]. However, no evidence of the corresponding $11/2^-$ or $7/2^+$ states has been found, even if the former would be expected to lie below the $5/2^+$ state in excitation energy. As illustrated in Figure 5.2, the energies of the $1/2^+$ states in the heavier isotopes show a parabolic behaviour typical for particle-hole excitations. The $3/2^+$ and $5/2^+$ states follow a similar trend. However, the interpretation of the observed $3/2^+$ and $5/2^+$ states in ^{193}Bi (Band 4 in Figure 4.6) and the $5/2^+$ state ^{191}Bi (Band 3 in Figure 4.12) as particle-hole excitations is not likely and they are presumed to belong to a band based on the $1/2^+$ state. Indeed, an intruder character for the $5/2^+$ states is most improbable as the $d_{5/2}$ orbital lies deep below the Fermi surface.

The excitation energies of the oblate $2p-2h$ 0^+ states in the Pb isotopes (see [Fir96], [Vel02] and references therein) and the $9/2^-$ states from the oblate $1p-2h$ configuration in Tl isotopes [Fir96] with respect to the corresponding ground states are also presented in Figure 5.2. Starting from the closed neutron shell at $N = 126$, the trend for the $1/2^+$ states in bismuth isotopes closely resembles that of the oblate 0^+ states in the lead nuclei. Near the neutron mid-shell, the curve for the Pb isotopes shows signs of levelling off and the intruder states in thallium isotopes follow the parabolic trend with a minimum at $N = 108$. In contrast, the behaviour of excitation energies of the $1/2^+$ states in the Bi isotopes shows a steeper downward trend in going from ^{189}Bi to ^{187}Bi. If this tendency remains down to ^{185}Bi with $N = 102$, the $1/2^+$ state comes very close to the $9/2^-$ state and may even become the ground state, as suggested by decay studies [Dav96, Pol01, And03].

Batchelder *et al.* [Bat99] account for the behaviour of the $1/2^+$ states in the light bismuth isotopes by proposing that instead of the oblate configuration of the heavier isotopes, a prolate $1/2^+$ intruder structure is observed close to the neutron mid-shell. They also suggest that this state would originate from the $1/2^+[660]$ Nilsson orbital which is deeply downsloping as prolate deformation increases. However, this orbital with its high-j origin is strongly affected by the Coriolis interaction and the $1/2^+$ member of the band would be pushed higher in excitation energy. Another possibility for a prolate $1/2^+$ state would be the $1/2^+[400]$ configuration from the $s_{1/2}$ orbital. According to the results of a recent experiment, the decay properties of the $(1/2^+)$ ground state in ^{185}Bi clearly indicate a prolate shape, provided that the shape of the $(1/2^+)$ state in the daughter ^{181}Tl nucleus does not change compared to the heavier isotopes [And03]. In the heavier bismuth isotopes down to ^{189}Bi, the properties of the

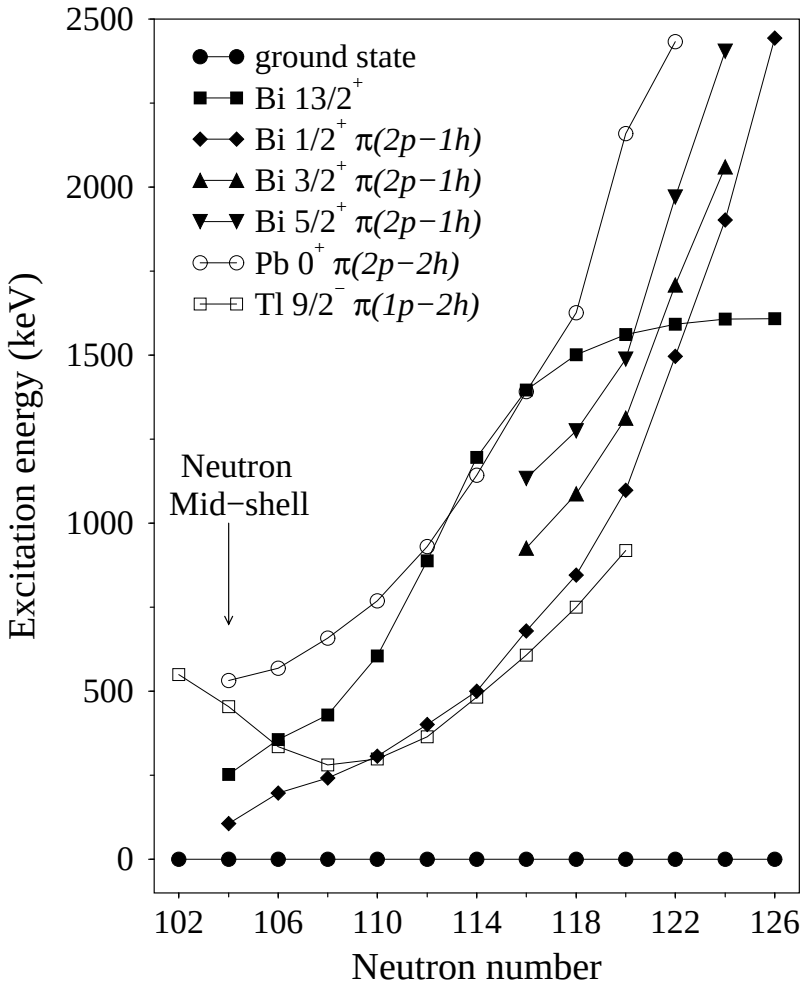

Figure 5.2: Systematic behaviour of the $1/2^+$, $3/2^+$ and $5/2^+$ intruder and the $13/2^+$ isomeric states in odd-A Bi isotopes with respect to the $9/2^-$ ground state. The excitation energies of the oblate intruder $9/2^-$ states in odd-even Tl and 0^+ states in even-even Pb isotopes with respect to the corresponding ground states are also shown.

$1/2^+ \rightarrow 1/2^+$ decays to the ground states of the Tl isotopes are consistent with an oblate deformation, until a slight change is observed in going to ^{187}Bi [And03]. In the present experiments, the low-spin states are weakly populated and the lack of γ-γ coincidences does not allow the band structures feeding the $1/2^+$ states in ^{191,193}Bi to be firmly established. However, the observed γ-ray energy spectrum associated with the $1/2^+$ state in ^{191}Bi (Figure 4.13) appears to have a more regular structure than that in ^{193}Bi (Figure 4.8) which would indicate an increase of collectivity and some change in shape of the $1/2^+$ state between the two isotopes. Furthermore, the tentative level scheme of ^{189}Bi suggests a prolate shape for the $1/2^+$ state in this nucleus [Hür03]. A comparison to its $N = 106$ isotones reveals that three separate prolate bands are observed in ^{187}Tl [Lan95], prolate structures become yrast in ^{188}Pb [Hee93] and the yrast band in ^{190}Po has been associated with prolate deformation

[Vel03]. On this basis, the appearance of prolate bands in ^{189}Bi (or even in ^{191}Bi) would not be unexpected. As the α-decay properties of the $1/2^+$ state do not show any change of configuration in going to ^{189}Bi, one scenario is that the collective structure would be based on a prolate $1/2^+$ state and the link to the α-decaying oblate $1/2^+$ configuration remains unobserved.

5.2.3 $13/2^+$ isomeric states

The behaviour of the excitation energy of the $13/2^+$ isomeric state in the odd-A bismuth isotopes with respect to the $9/2^-$ ground state is also illustrated in Figure 5.2 [Fir96, And01, Hür02]. In contrast to the $2p-1h$ structures, the energy of this state remains roughly constant in isotopes with $118 \leq N \leq 126$ but as the neutron number decreases further, a clear lowering is observed. In the range of $104 \leq N \leq 108$ the trend of the $13/2^+$ state actually resembles that observed for the $1/2^+$ intruder excitations. The $13/2^+$ state is interpreted as having a proton $i_{13/2}$ single-particle structure and its behaviour can at least partly be understood from the $\pi\nu^{-1}$ interaction energies and assuming a spherical shape. The interaction of the $i_{13/2}$ proton with holes in the neutron $i_{13/2}$ orbital is less repulsive than that for the $h_{9/2}$ proton and thus, the $13/2^+$ state is lowered in excitation energy with respect to the $9/2^-$ ground state [Lon86]. The steepening of the downward slope coincides with the opening of the neutron $i_{13/2}$ orbital at $N = 114$. The lowering of this proton high-j $i_{13/2}$ state relative to the $h_{9/2}$ state when going towards the neutron mid-shell is similar to that of the other high-j states close to magic Z, for example the proton $h_{11/2}$ state with respect to the $d_{5/2}$ and $g_{7/2}$ states in $Z \sim 50$ nuclei.

The shell-model calculations described in Reference [Hür02] also consider the $13/2^+$ state in bismuth isotopes as an odd proton in the $i_{13/2}$ orbital interacting with the even-even Pb core. In this approach, a parametrisation like that used for the $9/2^-$ state reproduces the behaviour of the $13/2^+$ states in the range of $203 \leq A \leq 209$. The energy shift occurring in lighter isotopes has been accounted for by modifying the $\pi i_{13/2} \otimes \nu f_{5/2}$ interaction strength and the resulting shell-model calculations are in agreement with the experimental measurements. However, the present results for ^{191,193}Bi with collective band structures feeding the $13/2^+$ states stress the importance of deformation in the reduction of the excitation energy. To be able to explain the observed structures, the description of this state in terms of a single proton outside the closed $Z = 82$ core does not seem to be sufficient. As the spin and parity assignment of $I^\pi = 13/2^+$ is strongly supported by the present experimental data, the collectivity of this state could originate from a deformed core configuration having $I^\pi = 0^+$. As in the case of the observed negative-parity band, the first qualitative description for the $13/2^+$ states in Bi isotopes with $A \leq 193$ could be based on the coupling of a $i_{13/2}$ proton to the oblate $2p-2h$ 0^+ intruder state of the lead core.

5.3 TRS calculations

The properties relevant for a description of a nucleus in the present region of interest are the type and degree of deformation together with the effects of rotation. The influence of a non-spherical shape on the relative energies of various single-particle levels has already been shown (see Figure 5.1 for ^{191}Bi). In the following discussion, rotational effects are examined with Total Routhian Surface (TRS) calculations (performed by Ramon Wyss) which use the deformed Woods-Saxon potential and result in potential energy maps in the $\beta_2 - \gamma$ deformation plane.

5.3.1 Negative-parity configurations

Total Routhian Surfaces for the $(\pi, \alpha) = (-, +1/2)$ configurations in ^{193}Bi, calculated at rotational frequencies of $\hbar\omega = 0.00$, 0.08 and 0.16 MeV are shown in Figures 5.3 (a)-(c) and the corresponding maps for ^{191}Bi in Figures 5.3 (d)-(f). The plots at $\hbar\omega = 0.00$ MeV (Figures 5.3 (a),(d)) already reveal most of the essential minima present in the surfaces. The absolute energy minimum in both nuclei is found with very small deformation of $\beta_2 \approx 0.07$ (marked with a filled circle) while another negative-parity minimum is located close to the collective oblate axis ($\gamma = -60°$) at $\beta_2 \approx 0.18$ and 0.19 in ^{193}Bi and ^{191}Bi, respectively. Even if rotational effects are imposed into the system, these minima remain the main features in both nuclei.

In both ^{193}Bi and ^{191}Bi, the nearly spherical absolute energy minimum corresponds to the $9/2^-$ ground state. The TRS predicted deformations fall into the range consistent with the expected ground-state spin and parity as outlined in Section 5.2.1. The explanation for the observed negative-parity bands is now provided by the more-deformed oblate minima which largely involve the proton $2p - 2h$ excitation where the $s_{1/2}$ orbital is emptied and the two protons are moved to the $9/2^-[505]$ orbital. This structure is most probably characterised by a state with $\Omega = 7/2$ and of mixed $h_{9/2}/f_{7/2}$ origin. At the calculated oblate deformation of $\beta_2 \approx 0.19$ for ^{191}Bi, the first excited configuration above the Fermi surface is the $7/2^-[514]$ state from the $h_{9/2}$ orbital which becomes mixed with the $7/2^-[503]$ state from the $f_{7/2}$ orbital (Figure 5.1). The next possible negative-parity structure would be the other $\Omega = 7/2$ state also involving these two components and lying more than one MeV higher in energy.

The tabular output of the TRS calculations provides for each minimum the total energy together with the total aligned angular momentum and its division to proton and neutron components as a function of rotational frequency. The calculations are also extended up to higher frequencies than to which the plots are available. The calculated features of the surfaces describe quantitatively the properties of the observed bands in ^{193,191}Bi. The separation between the weakly-deformed and more-deformed

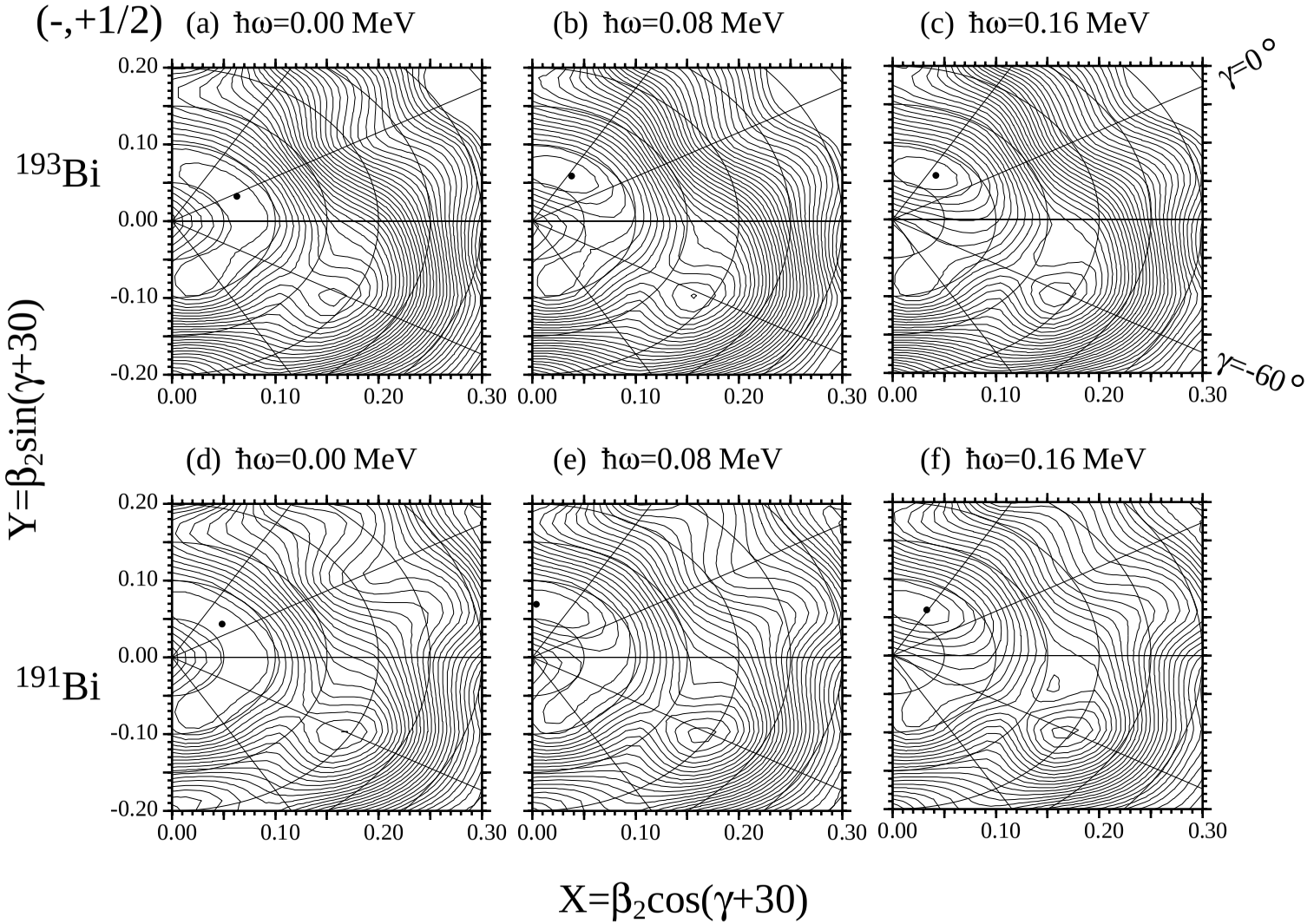

Figure 5.3: Total Routhian Surfaces for the (π,α)=(-,+1/2) configuration in ^{193}Bi at (a) $\hbar\omega = 0.00$ MeV, (b) $\hbar\omega = 0.08$ MeV and (c) $\hbar\omega = 0.16$ MeV and for ^{191}Bi at (d) $\hbar\omega = 0.00$ MeV, (e) $\hbar\omega = 0.08$ MeV and (f) $\hbar\omega = 0.16$ MeV [Wys02]. The energy difference between the contour lines is 100 keV.

oblate minima is calculated to be about 540 keV in ^{193}Bi and decreases to 360 keV in ^{191}Bi. However, a candidate for the $7/2^-$ band head in ^{191}Bi was found at 149 keV (Figure 4.12) which is a somewhat lower energy than the prediction from the theory. This may well be due to general difficulties in calculating zero-point energies of the potential energy minima relative to each other. Despite this problem, the examination of the calculated total energy as a function of spin provides a prediction for the crossing of the bands attributed to the separate potential minima. In the present case, the low-lying oblate band is observed to cross the ground-state band around $I \sim 11/2$ which agrees with the calculations for both nuclei. These results also suggest that the deviation of the binding energy of the ground state compared to the prediction for spherical shape could arise from an oblate component, whose amplitude becomes significant in ^{193}Bi and increases as the neutron number further decreases.

5.3.2 Positive-parity configurations

TRS plots for the $(\pi, \alpha) = (+, +1/2)$ configurations at rotational frequencies of $\hbar\omega =$ 0.00, 0.08 and 0.16 MeV for ^{193}Bi and ^{191}Bi are illustrated in Figures 5.4 (a)-(c) and 5.4 (d)-(f), respectively. At $\hbar\omega = 0.00$ MeV, a minimum close to the oblate $\gamma = -60°$ axis at $\beta_2 \approx 0.13$ is observed in both ^{193}Bi (Figure 5.4 (a)) and ^{191}Bi (Figure 5.4 (d)) and assigned to the $s_{1/2}$ intruder $2p-1h$ proton configuration. Another oblate energy minimum, associated with the $13/2^+[606]$ configuration and involving again the proton $2p-2h$ excitation lies at $\beta_2 \approx 0.21$ (Figure 5.4 (d)) in ^{191}Bi and becomes more apparent as the rotation frequency increases. This minimum is calculated to be located about 700 keV above the ground state as compared to the 430 keV separation between the $13/2^+$ and $9/2^-$ states found experimentally. In ^{193}Bi, the corresponding structure is not so well separated from that at $\beta_2 \approx 0.13$ but develops as rotational effects are superposed into the system becoming more visible at $\hbar\omega = 0.16$ MeV (Figure 5.4 (c)). The calculations for ^{191}Bi also reveal triaxial minima which have $\beta_2 = 0.24 - 0.27$ ($\gamma = +19°$ and $\gamma = -19°$) and are associated with the $1/2^+[660]$ configuration of $\pi i_{13/2}$ origin. In ^{193}Bi, the triaxial configuration is calculated to be higher in energy and develops at larger rotation frequencies as shown in Figure 5.4 (c). The calculated aligned angular momentum for the oblate $i_{13/2}$ band in both ^{193}Bi and ^{191}Bi shows an increase of $\sim 14\hbar$ when the rotational frequency is increased from 0.161 to 0.210 MeV, indicating an alignment of a pair of neutrons in the $i_{13/2}$ orbital. Experimentally, the alignment is found to start at spin 27/2 in ^{193}Bi but is not observed in ^{191}Bi where the $i_{13/2}$ band has been established only up to the $21/2^+$ state.

The prediction of oblate and triaxial, nearly prolate minima from the $i_{13/2}$ proton configuration can be compared to the observed structures in the neighbouring nuclei. The oblate and prolate $i_{13/2}$ bands in ^{189}Tl cross between spins $17/2^+$ and $21/2^+$. This is in good agreement with the calculations for its isotone ^{191}Bi where the separation

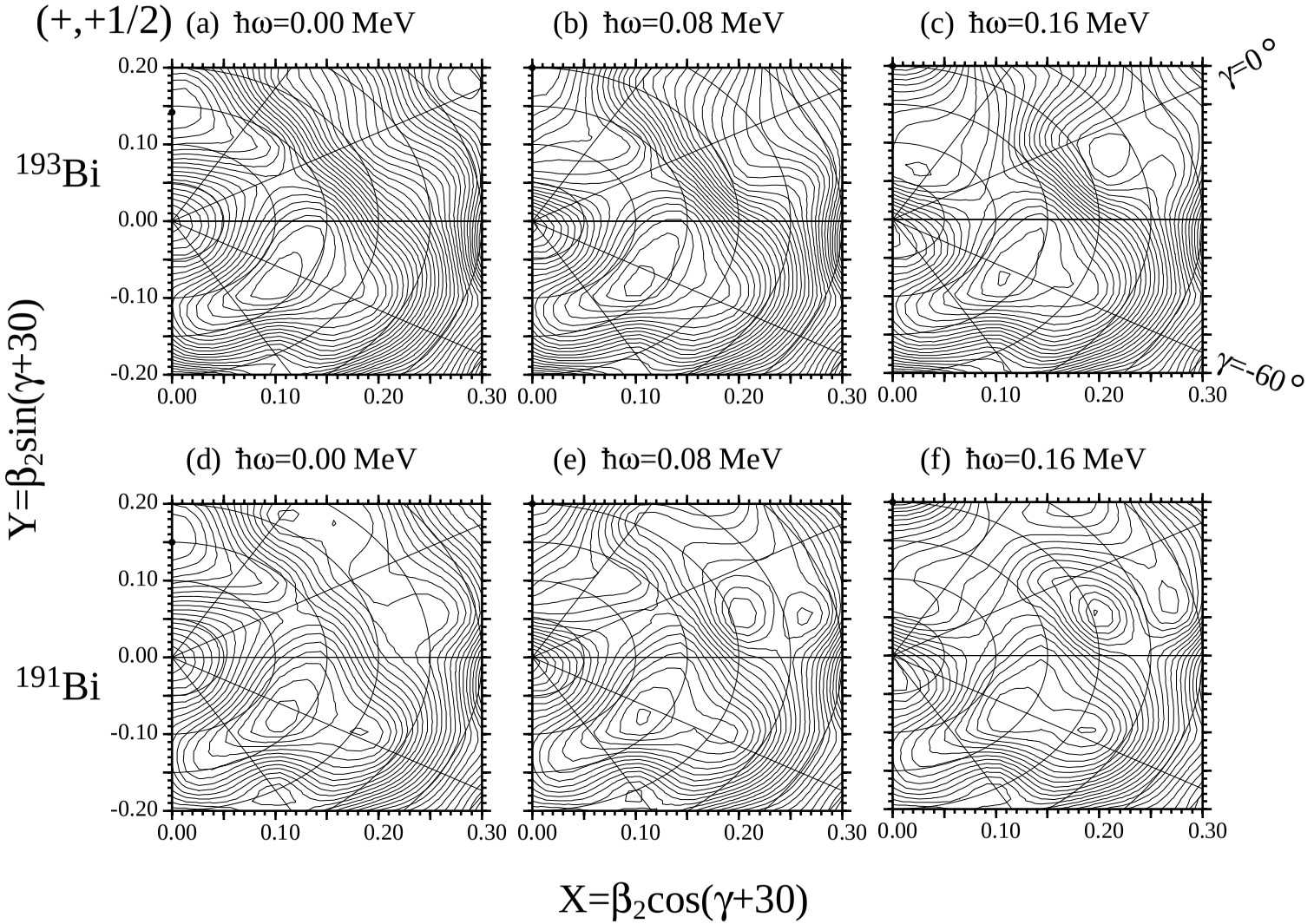

Figure 5.4: Total Routhian Surfaces for the $(\pi,\alpha)=(+,+1/2)$ configuration in ^{193}Bi at (a) $\hbar\omega = 0.00$ MeV, (b) $\hbar\omega = 0.08$ MeV and (c) $\hbar\omega = 0.16$ MeV and for ^{191}Bi at (d) $\hbar\omega = 0.00$ MeV, (e) $\hbar\omega = 0.08$ MeV and (f) $\hbar\omega = 0.16$ MeV [Wys02]. The energy difference between the contour lines is 100 keV.

between the oblate and prolate $i_{13/2}$ minima suggests a crossing of the assigned bands around $I = 10$. It remains to be seen in future experiments, whether the 1736 keV level assigned with $I^\pi = (21/2^+)$ (Figure 4.12) already belongs to the prolate band. In an experiment for ^{189}Bi, the $N = 106$ isotone of the ^{187}Tl, ^{188}Pb and ^{190}Po nuclei which all show prolate-deformed structures, a regular cascade of E2 transitions has been observed and tentatively interpreted as the prolate $i_{13/2}$ band [Hür03].

5.4 Kinematic moments of inertia

A convenient method to examine properties of a nucleus via the observed collective bands is provided by the definition of moments of inertia in terms of the rotational frequency ω and the projection of the angular momentum on the rotation axis (x axis) I_x. The kinematic moment of inertia $\mathcal{J}^{(1)}$ of a nucleus is calculated at the intermediate spin (I_a) of the initial (E_i, I_i) and final (E_f, I_f) states as

$$\mathcal{J}^{(1)} = \frac{I_x(I_a)}{\omega(I_a)}, \tag{5.1}$$

where

$$\omega(I_a) = \frac{E_i - E_f}{I_x(I_i) - I_x(I_f)} \quad \text{and} \tag{5.2}$$

$$I_x(I) = \sqrt{I(I+1) - K^2}. \tag{5.3}$$

The K quantum number is the projection of the total angular momentum I to the symmetry axis (z axis). A natural tendency for $\mathcal{J}^{(1)}$, evident from the corresponding classical definition, would be to increase as deformation increases and be larger for prolate deformation than for an oblate shape. This behaviour is observed in Figure 5.5 where the experimental kinematic moments of inertia for the oblate bands in ^{190}Pb and ^{194}Po are plotted together with those for the prolate band in ^{188}Pb. The magnitude of the values of $\mathcal{J}^{(1)}$ is typically used as one argument in the assignment of a prolate or an oblate deformation to a band and can now serve as a guideline for the interpretation of the established bands in ^{191}Bi and ^{193}Bi.

As illustrated in Figure 5.5, the $i_{13/2}$ band (Band 1) in ^{193}Bi settles between the oblate and prolate configurations of the neighbouring nuclei while the corresponding structure in ^{191}Bi shows values slightly closer to the prolate band in ^{188}Pb. Since the TRS calculations yield the values of I_x as a function of ω for each potential minimum, a theoretical prediction for the kinematic moment of inertia for the associated bands can be extracted. The $\mathcal{J}^{(1)}$ values for the $i_{13/2}$ band (Band 1) in ^{191}Bi as calculated before an alignment of a pair of neutrons in the $i_{13/2}$ orbital, are plotted in Figure 5.5 and qualitatively reproduce the experimental values. However, the frequency of the

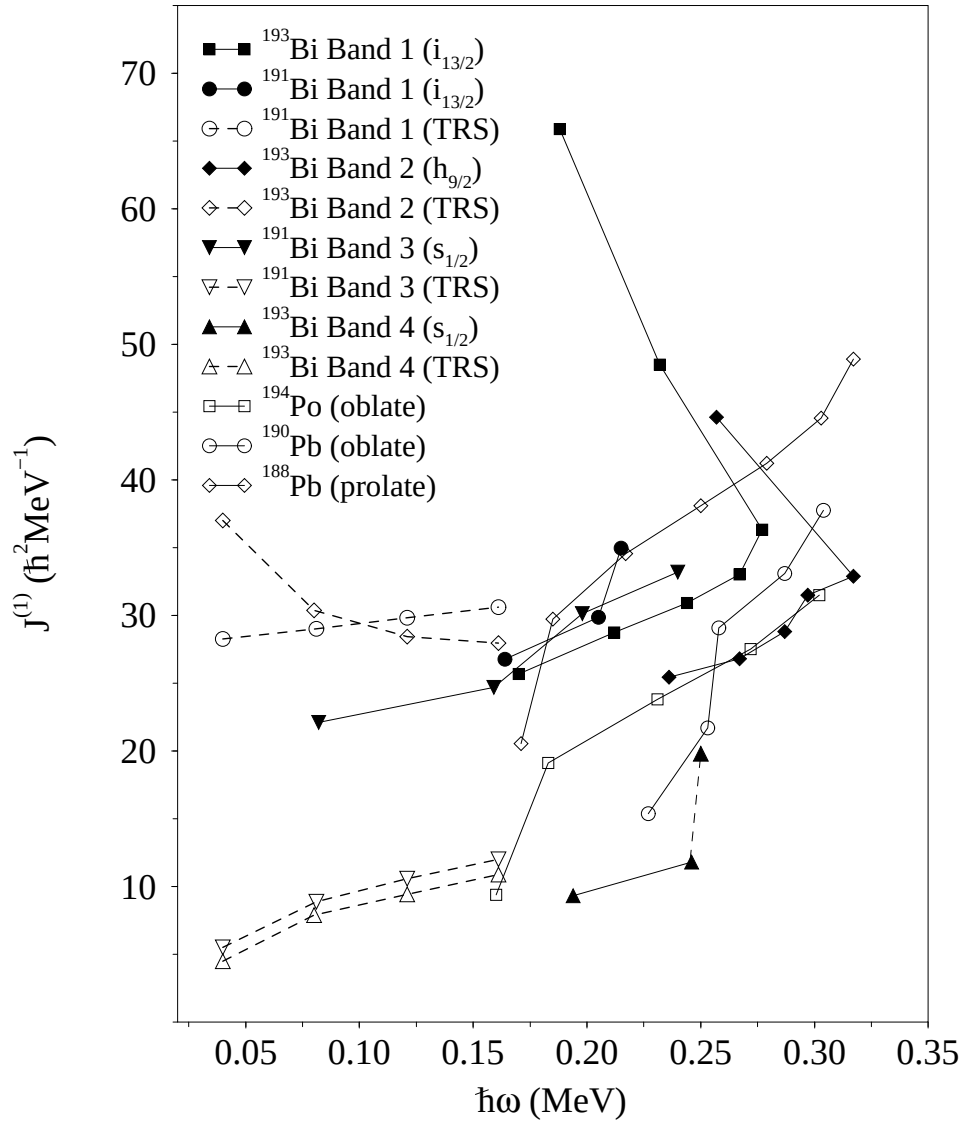

Figure 5.5: Experimental kinematic moments of inertia $\mathcal{J}^{(1)}$ for Band 1, Band 2 and Band 4 in ^{193}Bi and for Band 1 and Band 3 in ^{191}Bi (filled symbols). Theoretical predictions from TRS calculations for Band 2 and Band 4 in ^{193}Bi, for Band 1 and Band 3 ^{191}Bi (open symbols, dashed line) and experimental values of $\mathcal{J}^{(1)}$ for the yrast bands in ^{194}Po [Hel99] (oblate), ^{190}Pb [Dra98] (oblate) and in ^{188}Pb [Hee93] (prolate) (open symbols, solid line) are also presented. The values for 2^+ states in ^{188,190}Pb are not shown.

alignment is lower than that found experimentally hence preventing the comparison at higher rotational frequencies. The moments of inertia for the $h_{9/2}$ band (Band 2) in ^{193}Bi are quite similar to those of the oblate band in ^{194}Po, agreeing with the suggested oblate deformation. The magnitude of the $\mathcal{J}^{(1)}$ values from the TRS calculations, again plotted before a neutron alignment is in reasonable agreement with the experimental results.

The $\mathcal{J}^{(1)}$ values for the band feeding the $1/2^+$ intruder state in ^{193}Bi (Band 4) lie well below those for bands associated with oblate shape. This indicates a modest deformation which is in agreement with the results of the TRS calculations. When going from ^{193}Bi to ^{191}Bi, the observed change in the band structure feeding the $1/2^+$ intruder state naturally also results in different values of $\mathcal{J}^{(1)}$, which for Band 3 in ^{191}Bi turn out to be close to those of the prolate band in ^{188}Pb. However, the TRS calculations which suggest a similar deformation for the $1/2^+$ intruder structure in both nuclei, fail to reproduce this change. The calculations are in better accordance with the results of the decay studies which show no sign of change in the structure of the α-decaying $1/2^+$ state when going from ^{193}Bi to ^{191}Bi (Section 5.2.2).

5.5 Aligned angular momenta

The total aligned angular momentum (I_x) of a state has two components, the contribution of the core and that of quasiparticle excitations. A simple method to resolve the quasiparticle content and changes in the intrinsic excitations via the observation of collective bands is provided by the formalism of Bengtsson and Frauendorf [Ben79]. In this approach, the moment of inertia of the collective core is first evaluated by using the so-called Harris formula [Har65] $J_{ref} = J_0 + J_1\omega^2$ (J_0 and J_1 are the Harris parameters) when a reference value for the total aligned angular momentum can be obtained as

$$I_{x,ref}(\omega) = \omega[J_0 + J_1\omega^2]. \tag{5.4}$$

The quasiparticle component (i_x) at the intermediate spin I_a of the initial and final states then reads

$$i_x(I_a) = I_x(I_a) - I_{x,ref}(\omega(I_a)), \tag{5.5}$$

where I_x is extracted using Equation 5.3 and $I_{x,ref}$ is calculated at the experimental rotational frequency (Equation 5.2).

The aligned angular momenta i_x for the positive and negative signatures of the oblate $i_{13/2}$ and $h_{9/2}$ structures in ^{193}Bi together with those for the $i_{13/2}$ band in ^{191}Bi are shown in Figure 5.6 (a). The rotating reference was chosen to give a constant (zero) alignment for the low-spin states of the $i_{13/2}$ band in ^{193}Bi. Instead, the beginnings of the curves for the $h_{9/2}$ band in ^{193}Bi, corresponding to the band-head configuration, exhibit negative values of i_x due to the slightly lower deformation of this structure. The values of i_x for the $i_{13/2}$ band in ^{191}Bi lie above the zero level which may suggest a somewhat different character for this band.

In Figure 5.6 (b), the values of i_x for the $i_{13/2}$ band in ^{193}Bi are plotted along with those for the $i_{13/2}$ band in ^{191}Tl [Rev95] and the oblate band in ^{194}Po [Hel99]. Unfortunately, a more thorough comparison between the curves is impeded by the non-observation

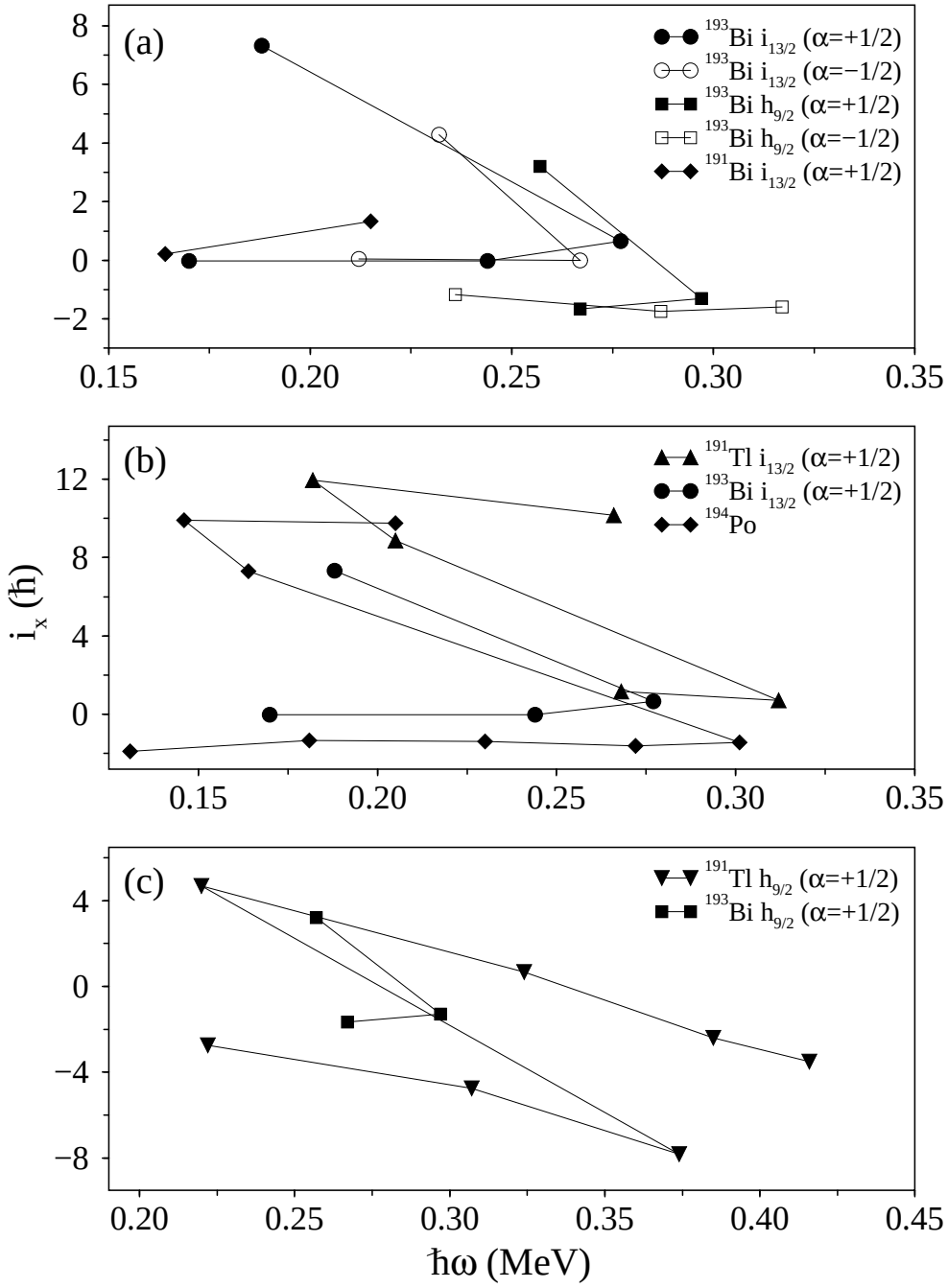

Figure 5.6: (a) Aligned angular momenta i_x for the favoured ($\alpha = +1/2$) and unfavoured ($\alpha = -1/2$) signatures of Band 1 ($i_{13/2}$, $K = 6.5$) and Band 2 ($h_{9/2}$, $K = 3.5$) in ^{193}Bi together with the $\alpha = +1/2$ signature of Band 1 ($i_{13/2}$) in ^{191}Bi. (b) Aligned angular momentum i_x for the $\alpha = +1/2$ signature of Band 1 in ^{193}Bi compared to the $\alpha = +1/2$ configuration of the $i_{13/2}$ band in ^{191}Tl [Rev95] and the oblate band in ^{194}Po [Hel99]. (c) The $\alpha = +1/2$ signature of the $h_{9/2}$ band (Band 2) in ^{193}Bi as compared to the $h_{9/2}$ band in ^{191}Tl ($K = 4.5$). In all plots, Harris parameters of $J_0 = 20.9\hbar^2\text{MeV}^{-1}$ and $J_1 = 169.9\hbar^4\text{MeV}^{-3}$ have been used for the rotational reference.

of the $i_{13/2}$ band in ^{191}Tl down to its band head. The behaviour of the aligned angular momenta beyond the band crossing is similar for all of the bands and the gain of $\sim 11\hbar$ both in ^{191}Tl and ^{194}Po agrees with the alignment of an $i_{13/2}$ neutron pair. The plots for the $i_{13/2}$ bands in ^{193}Bi and ^{191}Tl also indicate that the difference of a proton pair does not have an influence on the properties of the band. The opposite seems to be true for the oblate $h_{9/2}$ bands in ^{193}Bi and ^{191}Tl, as illustrated in Figure 5.6 (c). In this case, the removal of two protons in going from ^{193}Bi to ^{191}Tl apparently results in a smaller deformation for ^{191}Tl which is demonstrated by the downward slope and more negative values of i_x, as compared to the curve for the $h_{9/2}$ band in ^{193}Bi. The comparison of aligned angular momenta in ^{191}Bi to those in its $N = 108$ isotones is hindered by the lack of data points.

5.6 B(M1)/B(E2) ratios

Considering the structure of an odd-A nucleus, two limits for the coupling of a particle to a deformed even-even core have been introduced. In the strong-coupling scheme [Nil55] the odd particle adiabatically follows the rotation of the core whereas in the decoupling picture [Ste75], Coriolis effects distort the regular rotational bands. In practice, the observed band structures seldom purely obey these schemes but rather exhibit an intermediate form between the two limits. In the case of strong coupling when both the intraband M1 and inband E2 transitions are observed, the intrinsic nature of the initial state can be resolved by examining the probability of the two de-excitation paths as a ratio $B(M1)/B(E2)$.

The strength of a magnetic dipole transition $B(M1)$ is proportional to the magnetic dipole moment of the nuclear system which can be formulated in terms of single-particle (g_K) and collective (g_R) gyromagnetic ratios. Correspondingly, the probability for a de-excitation through an electric quadrupole transition depends on the intrinsic quadrupole moment Q_0. The observed $B(M1)/B(E2)$ ratios within a strongly coupled band can be shown to be proportional to the ratio $(g_K - g_R)^2/Q_0$. As Q_0 represents the deformation associated with the band and $g_R \approx Z/A$, the measured $B(M1)/B(E2)$ values indicate g_K which is very sensitive to the active single-particle orbital. The experimental ratios of reduced transition probabilities (in units $(\mu_N/eb)^2$) were extracted using the standard formula

$$\frac{B(M1)}{B(E2)} = 0.697 \frac{E_\gamma^5(I \to I-2) I_\gamma(I \to I-1)}{E_\gamma^3(I \to I-1) I_\gamma(I \to I-2)(1+\delta^2)}, \tag{5.6}$$

where E_γ is the γ-ray energy (in MeV), I_γ is the γ-ray intensity and δ is the E2/M1 mixing ratio. In the present case, the inband transitions are assumed to be pure and thus, δ is set to zero. The measured $B(M1)/B(E2)$ ratios within the observed bands in ^{191,193}Bi are compared to theoretical estimates calculated using the geometrical

model [Don83, Don87] for their presumed intrinsic configurations. The values of g_K for the proton orbitals are obtained from Woods-Saxon calculations and the radius parameter $r_0 = 1.275$ fm is used in the conversion between Q_0 and β_2 deformation.

For Band 1 in ^{193}Bi, a very good agreement between the experimental $B(M1)/B(E2)$ ratios and the theoretical estimate for an $i_{13/2}$ proton configuration at the calculated deformation of $\beta_2 = -0.21$ is achieved, as shown in Figure 5.7 (a). In contrast, the measured ratios for the corresponding structure in ^{191}Bi lie well below the theoretical estimate when using similar input parameters (Figure 5.7 (b)). One explanation for this behaviour could be triaxial shape, an assumption which is supported also by the slightly increased signature splitting in the observed band in ^{191}Bi as compared to that in ^{193}Bi. Even if K is not a good quantum number for triaxial deformation, it may be indicative to use lower values in the calculation as axial asymmetry can be considered to diminish the effective value of K. Following this idea for Band 1 in ^{191}Bi, the experimental B(M1)/B(E2) ratios can be better reproduced hence suggesting a change towards a decoupled prolate configuration for the $i_{13/2}$ state when approaching the neutron mid-shell.

For the negative-parity structure in ^{193}Bi (Band 2), the theoretically predicted values are in accordance with the experimental $B(M1)/B(E2)$ ratios (Figure 5.7 (c)) if the proposed mixed $f_{7/2}/h_{9/2}$ proton configuration with $\Omega = 7/2$ and $g_K = 1.16$ (see Section 5.3.1) is adopted. Calculations with a pure $h_{9/2}$ structure having $\Omega = 9/2$ and $g_K = 0.81$ result in unreasonably low values compared to the experiment. The data for the $h_{9/2}$ band in ^{191}Bi are scarce but seem to agree with the calculations when using the same intrinsic configuration as that for the corresponding band in ^{193}Bi (Figure 5.7 (d)). This presumed mixed character for this $\Omega = 7/2$ Nilsson orbital has also been used to explain the abnormally large strengths of the $11^- \rightarrow 8^+$ transitions in the ^{192,190}Pb core nuclei [Dra01], further supporting the configuration assignment.

5.7 Systematics, particle-core coupling and isomeric states

As collective excitations have not been observed in the heavier odd-A bismuth isotopes, their structure has been successfully interpreted in terms of a coupling of the odd proton to spherical states in the even-even lead core. In the present work, the situation is observed to change in ^{193}Bi and ^{191}Bi and discussion of the results has so far concentrated on properties extracted from the collective bands. However, despite the onset of deformation, some states in ^{193}Bi bear resemblance to those in the heavier isotopes and a systematic approach to describe these structures seems justified. The investigation of the particle-core coupling is heavily based on level energy systematics and also yields some information on the nature of the observed isomeric states.

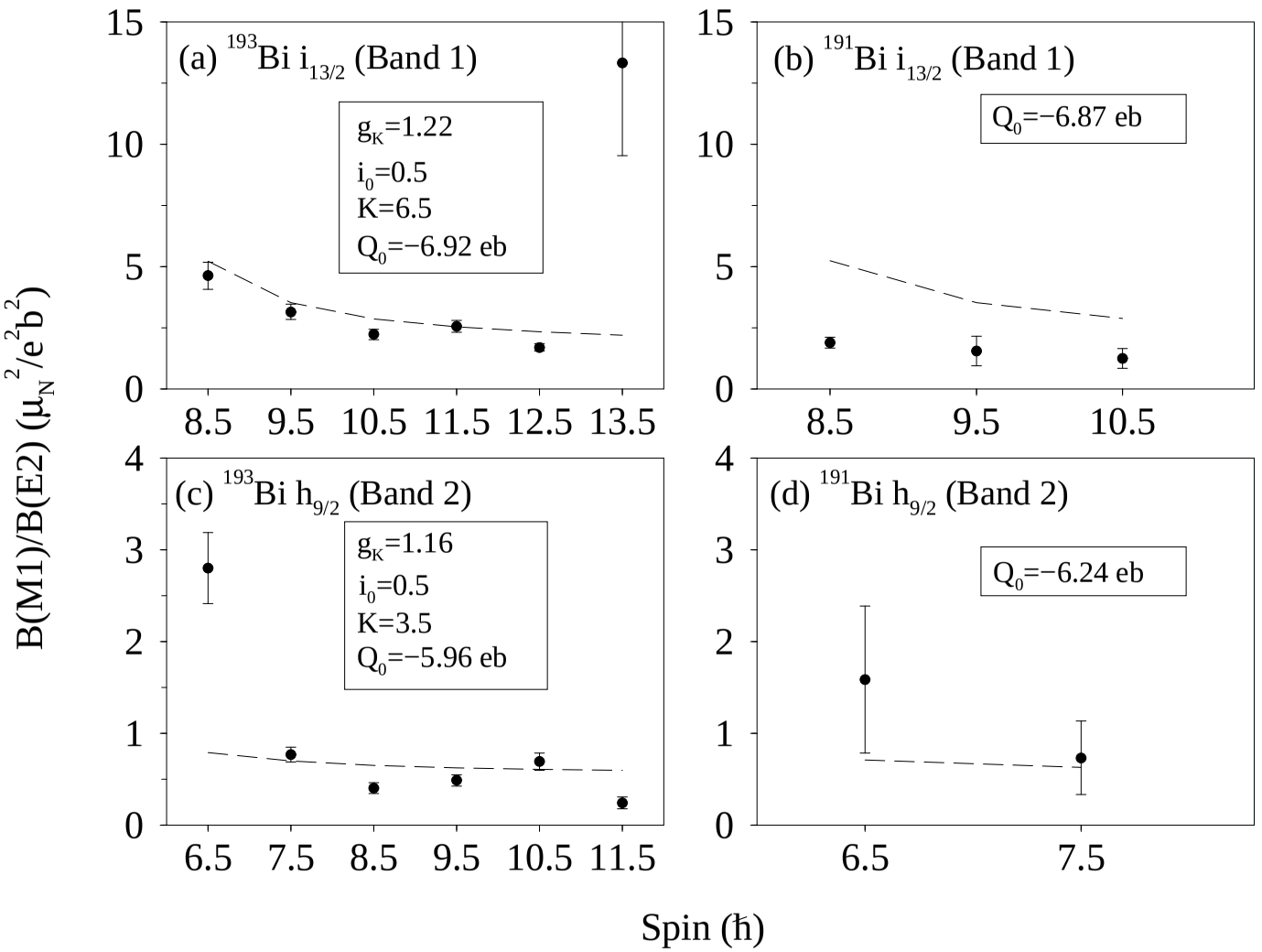

Figure 5.7: Experimental $B(M1)/(BE2)$ ratios for bands based on the $13/2^+$ state in (a) ^{193}Bi and (b) ^{191}Bi are marked with filled circles, theoretical estimates are indicated with dashed lines. Corresponding values for bands feeding the $9/2^-$ state are shown for ^{193}Bi in (c) and for ^{191}Bi in (d). The parameter values used for theoretical prediction for each band are indicated for ^{193}Bi, and for ^{191}Bi only if different.

5.7.1 Particle-core coupling in ^{193}Bi

It is natural to interpret the observed excited states in the odd-A bismuth isotopes as having a structure where the odd proton is coupled to states of the even-even lead core. More formally, this scheme can be expressed as $|\nu J^\pi, ^{A-1}\mathrm{Pb}\rangle \otimes |j_p\rangle = |I^\pi; ^A\mathrm{Bi}\rangle$, where ν refers to the core configuration, J^π and I^π are the total spin and parity of the active state in the Pb and Bi isotones, respectively, and j_p stands for the spin of the odd proton in the bismuth nucleus. This principle was already qualitatively utilised in the discussion for the oblate bands in ^{191,193}Bi and is now in a more quantitative manner applied in the description of quasiparticle excitations found in ^{193}Bi. As these configurations are of multi-nucleon character with one proton and 16 neutron holes outside the doubly-magic ^{208}Pb, a full shell-model calculation is not tractable. Instead, the present approach is based on the examination of experimental level energies in the lead and bismuth isotones and their systematic behaviour in the Bi isotopes. The excitation energies of configurations in the odd-A nucleus are determined by combining the energy of the even-even core state and the net interaction between the odd proton and the core. The former directly follows from experimental results for the lead nucleus whereas the latter can be deduced from the systematic behaviour of quasiparticle states in the bismuth isotopes. This so-called cluster interaction method using configurations characterised by the $h_{9/2}$ proton has been successfully employed to $^{201-197}$Bi [Cha86, Pie85] and the deduced interaction energies have been extrapolated to describe the observed states also in ^{195}Bi [Lon86].

If the proton $i_{13/2}$ orbital is also taken into account, there are two possibilities to produce both negative- and positive-parity states which would lie relatively low in excitation energy in ^{193}Bi. For negative-parity configurations, these are the coupling of the odd proton in the $h_{9/2}$ orbital to the positive-parity states of the lead core ($\pi h_{9/2} \otimes \nu J^+$) and alternatively, the coupling of an $i_{13/2}$ proton to the negative-parity core states, denoted as $\pi i_{13/2} \otimes \nu J^-$. In a similar manner, the low-lying positive-parity states could have the $\pi h_{9/2} \otimes \nu J^-$ or $\pi i_{13/2} \otimes \nu J^+$ structure. As a ground-state configuration, the $\pi h_{9/2} \otimes \nu J^+$ coupling is a natural choice for the negative-parity states since the structure involving the $i_{13/2}$ proton would contain additional excitation energy from both the single-particle part in ^{193}Bi and from the higher excitation energies of the core states. For the positive-parity configurations, the choice is not as obvious since both couplings include one component of extra energy compared to the ground-state structure. However, in the heavier odd-A bismuth isotopes, they are interpreted to be of the $\pi h_{9/2} \otimes \nu J^-$ configuration and even if the $13/2^+$ state having the odd proton in the $i_{13/2}$ orbital is lowered in excitation energy with decreasing N, the same interpretation is at first adopted also in ^{193}Bi.

The energy systematics of selected low-lying excited states in the odd-A bismuth isotopes is presented in Figure 5.8. In ^{193}Bi, the structures reminiscent of those estab-

lished in $^{195-201}$Bi are the irregular positive-parity sequence (Group A in Figure 4.6) together with the negative-parity bands (Band 2 and Band 3). The presumed core state involved in the $\pi h_{9/2} \otimes \nu J^-$ or $\pi h_{9/2} \otimes \nu J^+$ coupling is also indicated in Figure 5.8 (see [Lon86] and *e.g.* [Dra99] for level systematics in Pb isotopes). The spherical $J^\pi = 8^+, 10^+$ and 12^+ states in the lead isotopes down to ^{194}Pb have been assigned a rather pure $\nu i^2_{13/2}$ broken-pair configuration and they show a trend of decreasing excitation energy with decreasing N. The $J^\pi = 9^-$ state with its $\nu(f_{5/2} \otimes i_{13/2})$ structure and the mixed $J^\pi = 7^-, 6^+$ and 5^- states also follow the predictions for spherical two-quasiparticle configurations down to $A = 194$ [Ruy86, Pom90]. The spherical 2^+ and 4^+ states are lowered in excitation energy in Pb isotopes with $A < 196$ due to interaction with the deformed intruder-state bands [Dup87]. In ^{192}Pb, the ground-state band may be weakly oblate above the 2^+ state and the lowest observed 8^+ state at 2304 keV is interpreted to be a proton intruder whereas the second one at 2520 keV would have a dominant neutron configuration [Plo93a, Plo93b]. The closely-spaced 10^+ and 12^+ levels in ^{192}Pb are isomeric with half-lives of $t_{1/2} = 85(15)$ ns and $t_{1/2} > 1$ μs, respectively [Lag91].

The cluster interaction energies (E_{cl}) for $^{197-201}$Bi, extracted using the coupling of the $h_{9/2}$ proton to the core states are extrapolated to the present case. These energies are normalised to the ground-state $(\pi h_{9/2} \otimes \nu 0^+)_{9/2^-}$ interaction, which is set at zero, and combined with energies of states in the lead core. The calculated energy levels in ^{193}Bi (E_{theor}) together with the observed states both in ^{192}Pb (E_{core}) and in ^{193}Bi (E_{exp}) are listed in Table 5.1. The energy difference between the observed levels in ^{193}Bi and the corresponding core states is also given as $E_{exp} - E_{core}$. As the suggested 6^+- and 8^+-coupled configurations have not been observed earlier, the cluster interaction energies for these states could not be extracted.

The negative-parity states of Band 2 in ^{193}Bi seem to follow the systematic behaviour of the $2^+ - 8^+$ states in ^{192}Pb. However, the calculations give a reversed ordering for the $11/2^-$ and $13/2^-$ states compared to the experimental results which most probably is due to the extrapolation of the cluster interaction energies from ^{197}Bi. Generally, the observed states in the $h_{9/2}$ band appear to lie below the corresponding states in ^{192}Pb but are pushed higher in energy relative to the core configurations as the spin increases (see the right-hand column of Table 5.1). This behaviour suggests that the interaction between configurations having the $h_{9/2}$ proton coupled to the excited νJ^+ states and the $\pi h_{9/2} \otimes 0^+$ ground-state structure becomes increasingly repulsive with increasing spin J. This may be due to the fact that the $\nu i^{-2}_{13/2}$ component in the core state increases along with the spin and the largest repulsion compared to the ground state is obtained in the aligned $(\nu i^{-1}_{13/2} \otimes \pi h_{9/2})_{11^+}$ configuration. This interaction is 400 keV less repulsive for a coupling to spin 10^+ and even slightly attractive in some states [Lon81]. For the positive-parity states in Group A, the 1672 keV ($17/2^+$) and either one of the 2108 and 2127 keV levels below the long-lived isomer closely follow the systematics of the $17/2^+$ and $21/2^+$ states of $h_{9/2} \otimes 5^-$ and $h_{9/2} \otimes 7^-$ parentage,

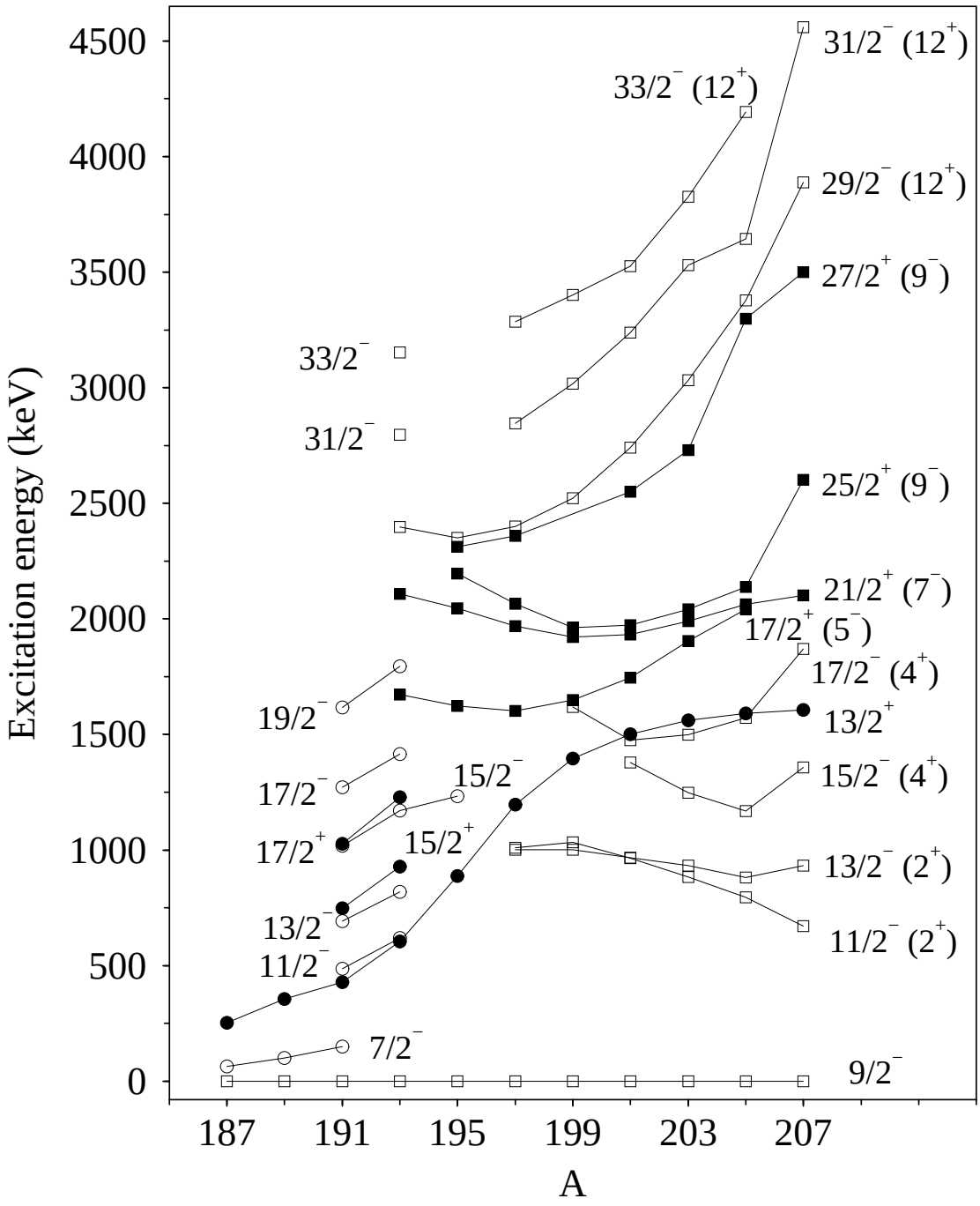

Figure 5.8: Systematics of selected low-lying excited states in odd-A Bi isotopes. States having positive (negative) parity are marked with filled (open) symbols. The presumed core state involved in the $\pi h_{9/2} \otimes \nu J^-$ or $\pi h_{9/2} \otimes \nu J^+$ coupling is also indicated. Where the exact excitation energy is not known due to unobserved low-energy transitions, Δ is set to 40 keV for clarity. The data are taken from [Ber69, Lon78, Lon79] (^{207}Bi), [Bro77, Lon82, Hüb83] (^{205}Bi), [Hüb78, Lon82, Hüb83] (^{203}Bi), [Bro82, Pie85] (^{201}Bi), [Pie85] (^{199}Bi), [Cha86] (^{197}Bi), [Lon86] (^{195}Bi), [And01, Ket03c] (^{189}Bi), [Hür02, Ket03c] (^{187}Bi) and for ^{193,191}Bi from the present work.

Table 5.1: Predicted excitation energies (E_{theor}) of states (I^π) in ^{193}Bi, calculated as the coupling of the odd proton (j_p) to the state in ^{192}Pb core (νJ^π) using the cluster interaction approach. The experimental level energies obtained in the present work for ^{193}Bi (E_{exp}) and their difference between the core states ($E_{exp} - E_{core}$) are also given. All energies are in units keV.

νJ^π	E_{core}	j_p	I^π	E_{theor}	E_{exp}	$E_{exp} - E_{core}$
2^+	854	$h_{9/2}$	$11/2^-$	850	620	−234
		$h_{9/2}$	$13/2^-$	750	818	−36
4^+	1356	$h_{9/2}$	$15/2^-$	1220	1170	−186
		$h_{9/2}$	$17/2^-$	1280	1415	59
6^+	1921	$h_{9/2}$	$19/2^-$	—	1795	−126
		$h_{9/2}$	$21/2^-$	—	2050	129
8^+	2520	$h_{9/2}$	$23/2^-$	—	2464	−56
		$h_{9/2}$	$25/2^-$	—	2588	68
12^+	2625	$h_{9/2}$	$29/2^-$	2420	2397[1]	−228
		$h_{9/2}$	$31/2^-$	2925	2796[1]	171
		$h_{9/2}$	$33/2^-$	3300	3152[1]	527
5^-	1860	$h_{9/2}$	$17/2^+$	1660	1672	−188
7^-	2323	$h_{9/2}$	$21/2^+$	2100	2108 or 2127	−215 or −196
9^-	2514	$h_{9/2}$	$25/2^+$	2400	—	
		$h_{9/2}$	$27/2^+$	2400	—	

[1] The unknown $(29/2^-) \rightarrow (25/2^-)$ transition energy is set to 40 keV.

respectively. Therefore, these states presumably would correspond to those observed in ^{195}Bi where they are yrast.

Considering the method itself, the description of states in an odd-A nucleus as having the weak-coupling type of structure does not set any boundary conditions to the shape of the core. However, the model predictions may not be valid for deformed core configurations as the extrapolated interaction energies do not account for the increased number of valence protons which are involved in the intruder structures. In this picture, the ^{193}Bi nucleus is at the borderline between spherical and deformed nuclei having features which are characteristic for both types of excitations. Although the low-lying states of the ^{192}Pb core may be weakly deformed, the cluster interaction calculations agree reasonably well with the experimental results for ^{193}Bi. Collective effects become more dominating in the low-lying structures of ^{191}Bi and ^{190}Pb and therefore, the cluster interaction approach using interaction energies extracted from the spherical bismuth isotopes is no longer suitable for an interpretation of the observed structures in ^{191}Bi.

5.7.2 Isomeric states in ^{191,193}Bi

The properties of the observed isomeric states in ^{191}Bi and ^{193}Bi are compiled in Table 5.2. Apart from the low-lying $13/2^+$ states, evidence for two high-spin isomers was found in ^{193}Bi and indications of one in ^{191}Bi. Since the direct de-excitations of these states were not observed, their excitation energies and spins could not be determined. However, isomeric $29/2^-$ states have been established in the heavier odd-A bismuth isotopes and the systematic trends suggest that such a state should be found in ^{193}Bi around 2.4 MeV in excitation energy (see Figure 5.8, Table 5.1). This is in good agreement with the energy of the 3-μs isomer which is observed at $2357 + \Delta$ keV, assuming that the energy of the unobserved de-exciting transition is too low to be detected in the present experiment. The isomeric $(29/2^-)$ state together with the $(31/2^-)$ and $(33/2^-)$ states feeding it are now interpreted to be of the $\pi h_{9/2} \otimes \nu i^{-2}_{13/2}$ configuration and they are in good agreement with the predictions of the cluster interaction calculations (Table 5.1). In ^{195}Bi, the isomeric $(29/2^-)$ state with a half-life of $t_{1/2} = 750$ ns de-excites to a $(27/2^+)$ state and consecutively to a $(25/2^+)$ and $(21/2^+)$ state by low-energy transitions [Lon86]. In the present work for ^{193}Bi, the topmost state observed below the 3-μs isomer is assigned to have spin and parity $I^\pi = (25/2^-)$ thereby suggesting a change in the decay path as compared to ^{195}Bi. Assuming that the de-excitation of the isomeric state in ^{193}Bi proceeds via a single transition to the $(25/2^-)$ state, the corresponding isomeric transition in the core could then be $h_{9/2} \otimes 12^+ \rightarrow h_{9/2} \otimes 10^+$ in character. In $A \sim 190$ lead nuclei, the transition between the 12^+ and 10^+ states from the neutron $i^2_{13/2}$ configuration is hindered due to the fact that the neutron $i_{13/2}$ orbital is half-filled [Bro92, Ruy86].

Table 5.2: Properties of isomeric levels in ^{191,193}Bi.

Nucleus	Level Energy (keV)	I^π	$t_{1/2}$
^{191}Bi	430	$13/2^+$	562(10) ns
^{191}Bi			400(40) ns
^{193}Bi	605	$13/2^+$	153(10) ns
^{193}Bi	$2357 + \Delta$	$(29/2^-)$	3.0(1) μs
^{193}Bi			> 10 μs

The other isomer in ^{193}Bi with a half-life of $t_{1/2} > 10$ μs is probably located just above the 2108 and 2127 keV levels and is much more difficult to interpret. Although many isomeric states have been observed in the heavier bismuth isotopes, none of these is as long-lived. As illustrated in the level energy systematics (Figure 5.8), the energy difference between the $27/2^+$ and $25/2^+$ states presumably of $h_{9/2} \otimes 9^-$ origin significantly decreases when going from ^{197}Bi to ^{195}Bi. This suggests that the $27/2^+$ state may be located below the $25/2^+$ state in ^{193}Bi, hence resulting in an isomeric state having a relatively long half-life. Another possibility is that this structure would

be related to the 11^- isomeric states which are associated with the oblate $\pi(i_{13/2}\otimes h_{9/2})$ configuration in Pb and Po nuclei. A weakly oblate band with a $\pi(i_{13/2}\otimes h^2_{9/2})$ character in ^{193}Bi would have $K = 29/2$ and the band head might be isomeric. In both cases, the isomeric state would de-excite via some intermediate state(s) to the observed 2108 and 2127 keV levels.

6 Conclusions and outlook

6.1 Summary

The very neutron-deficient ^{191,193}Bi nuclei have been studied using an experimental apparatus which combines the gas-filled recoil separator RITU and Ge-detector arrays for the observation of both prompt and delayed γ rays. Prior to the present work, only two α-decaying structures, the $9/2^-$ ground state and the $1/2^+$ intruder state were known in these two isotopes. Using the selective recoil-decay tagging (RDT), recoil gating and isomer tagging analysis techniques, excited states in ^{191}Bi and ^{193}Bi have for the first time been identified via in-beam γ-ray spectroscopic methods and extensive level schemes for both nuclei have been constructed. The level structures now observed disclose the competition between various nuclear shapes in the light bismuth isotopes close to the $82 < N < 126$ mid-shell.

The isomeric $13/2^+$ states were established in both ^{191}Bi and ^{193}Bi and strongly coupled bands based on them were observed indicating an oblate shape. A negative-parity band feeding the $9/2^-$ ground state, also having properties consistent with an oblate-deformed structure above the ground state was observed in both nuclei. The intrinsic excitation of this oblate band is assumed to be a mixed $h_{9/2}/f_{7/2}$ proton configuration with $\Omega = 7/2$. Quasiparticle states corresponding to spherical structures which dominate the level schemes of the heavier odd-A isotopes were observed in ^{193}Bi. Bands feeding the α-decaying $1/2^+$ states were identified and indicate some structural change between the ^{193}Bi and ^{191}Bi isotopes. Two higher-lying isomers, having halflives of $t_{1/2} = 3$ μs and $t_{1/2} > 10$ μs were observed in ^{193}Bi, the former continuing the systematic trend of isomeric $29/2^-$ states from the $h_{9/2} \otimes 12^+$ coupling. In ^{191}Bi, indications of an isomeric state with a half-life of $t_{1/2} = 400$ ns are obtained.

Nuclear shapes associated with various structures in ^{191}Bi and ^{193}Bi were extracted from TRS calculations. These calculations predict a nearly spherical $9/2^-$ ground state for both isotopes and deformations of $\beta_2 = 0.21$ and $\beta_2 = 0.18 - 0.19$ for the oblate $i_{13/2}$ and $h_{9/2}/f_{7/2}$ configurations, respectively. Both of these structures involve the proton $2p-2h$ intruder excitation across the $Z = 82$ shell gap. The calculated surfaces for positive-parity configurations also reveal minima at a more-deformed nearly prolate shape which are associated with the proton $1/2^+[660]$ configuration and in ^{191}Bi, a candidate band member for this low-Ω $i_{13/2}$ structure is observed. For the intruder $s_{1/2}$ configuration, a deformation of $\beta_2 = 0.13$ in both nuclei is predicted, being consistent with the observed level pattern in ^{193}Bi while that of ^{191}Bi indicates

increased collectivity. Whether this change indicates the observation of a prolate $1/2^+$ state in ^{191}Bi instead of the predicted oblate $2p-1h$ configuration, could not be established from the present data. Experimental results for the neighbouring Tl, Pb and Po nuclei reveal an onset of prolate deformation around $N = 106$, which is the neutron number of the next lightest bismuth isotope ^{189}Bi. The band structures observed in this nucleus infer a prolate deformation for both the $13/2^+$ isomeric and the $1/2^+$ intruder states and in the neutron mid-shell nucleus ^{187}Bi, a tentative assignment of prolate shape to the $13/2^+$ state has also been made [Hür03].

6.2 Present status and future perspectives at JYFL

In order to keep up with experimental challenges arising in the study of nuclear structure, new measurement techniques have to be developed or the existing ones have to be improved. As the principles described in the present work have proved their power and selectivity, several major upgrades for the system have already been performed. The most essential factor is to increase the efficiency of the Ge-detector array. This step has recently been realised by the implementation of the JuroGam array consisting of 43 Eurogam Phase I Ge detectors with a photopeak efficiency of 4.2% at 1.3 MeV. The singles efficiency compared to the Jurosphere II array is improved by a factor of $2.5-3$ which gives a factor of $6-9$ better efficiency in collecting γ-γ coincidences. Even if the new array as such is still not able to compete with for example Gammasphere, in conjunction with the efficiency of the RITU separator and the selectivity of the tagging methods it will reveal new nuclear information not probed before.

A large fraction of the γ-ray background in the present experiments originates from reactions of the beam with the helium gas in RITU and the window separating the gas-filled volume from the high vacuum of the beam line. The installation of a differential pumping system to operate without a gas window and the use of lower filling-gas pressures than in earlier experimental campaigns are found to decrease the counting rates of the Ge detectors, thereby allowing higher beam currents. Another recent modification for the separator is the mounting of a new dipole chamber where the scattered beam particles are effectively suppressed. The new chamber also enables the use of more symmetric reactions as the primary beam component is more strictly reduced and hence a smaller difference in the magnetic rigidities of the beam and fusion products can be distinguished. The availability of a large variety of beams with sufficient current requires constant development mainly in ion-source techniques. This has been realised at JYFL in the upgrade of the existing devices, the construction of new ones and the introduction of novel methods for production of ion beams from solid compounds. Moreover, practical work is invested into the preparation of thin targets from a variety of materials.

As the various tagging methods are based on the identification of the radioactivity of the nucleus of interest at the separator focal plane, a natural advancement is to increase the granularity of the detector system and its efficiency for the observation of these characteristic events. The most recent development in this respect is the GREAT (Gamma Recoil Electron Alpha Tagging) spectrometer [Pag03] which has been commissioned at the focal plane of RITU. An integral part of the GREAT setup is the Total Data Readout (TDR) data acquisition system which is able to treat all the output channels independently without a common hardware gate thus minimising the dead time in data collection. Recalling the discussion in Section 2.6, the upper limit for a measurable isomeric half-life in the TDR system is no longer limited by the width of the master gate, but restrictions for the lower limit due to the flight time of the recoils through the separator still remain.

The two main philosophies in exploiting the improved performance of an experimental setup of this type are to explore the known nuclei in more extreme conditions and in more detail, or to reach out for the last known isotope of a given element. The more detailed investigations are instructive especially for the odd-A nuclei where the paths of de-excitation are fragmented and the confirmation of even the lowest-lying structures requires the observation of γ-γ coincidences. On the other hand, structural studies of deformed nuclei at the limits of their existence are fruitful for the even-even isotopes, typically having a collective ground-state band with a sequence of E2 transitions whose level spacing already reveals some properties of the nucleus.

So far, the JuroGam+RITU+GREAT setup together with the TDR data acquisition system has been employed in experiments for the ^{254}No, ^{184}Pb, ^{170}Pt, ^{251}Md, ^{107}Te, ^{161}Re, ^{162}Os and ^{192}Po nuclei. The preliminary results obtained during the experiments have been very promising and a thorough analysis of the collected data is expected to reveal new features in these nuclei. Thus, a re-examination of the $^{193-187}$Bi isotopes with improved statistics would confirm whether the present interpretation of their structure holds and yield new knowledge on these exotic nuclei beyond the proton drip line. Moreover, in-beam spectroscopic study of the heaviest known proton emitter ^{185}Bi would provide the first observation of excited states in this nucleus and also elucidate nuclear properties affecting this exotic decay mode.

References

[All98] R.G. Allatt, R.D. Page, M. Leino, T. Enqvist, K. Eskola, P.T. Greenlees, P. Jones, R. Julin, P. Kuusiniemi, W.H. Trzaska and J. Uusitalo, Phys. Lett. B **437**, 29 (1976).

[Alp69] M. Alpsten and G. Astner, Nucl. Phys. A **134**, 407 (1969).

[And99] A.N. Andreyev, D. Ackermann, P. Cagarda, J. Gerl, F. Hessberger, S. Hofmann, M. Huyse, A. Keenan, H. Kettunen, A. Kleinböhl, A. Lavrentiev, M. Leino, B. Lommel, M. Matos, G. Münzenberg, C.J. Moore, C.D. O'Leary, R.D. Page, S. Reshitko, S. Saro, C. Schlegel, H. Schaffner, M. Taylor, P. Van Duppen, L. Weissman and R. Wyss, Eur. Phys. J. A **6**, 381 (1999).

[And00] A.N. Andreyev, M. Huyse, P. Van Duppen, L. Weissman, D. Ackermann, J. Gerl, F.P. Hessberger, S. Hofmann, A. Kleinböhl, G. Münzenberg, S. Reshitko, C. Schlegel, H. Schaffner, P. Cagarda, M. Matos, S. Saro, A. Keenan, C. Moore, C.D. O'Leary, R.D. Page, M. Taylor, H. Kettunen, M. Leino, A. Lavrentiev, R. Wyss and K. Heyde, Nature **405**, 430 (2000).

[And01] A.N. Andreyev, D. Ackermann, P. Cagarda, J. Gerl, F.P. Hessberger, S. Hofmann, M. Huyse, A. Keenan, H. Kettunen, A. Kleinböhl, A. Lavrentiev, M. Leino, B. Lommel, M. Matos, G. Münzenberg, C.J. Moore, C.D. O'Leary, R.D. Page, S. Reshitko, S. Saro, C. Schlegel, H. Schaffner, M.J. Taylor, P. Van Duppen, L. Weissman and R. Wyss, Eur. Phys. J. A **10**, 129 (2001).

[And02a] A.N. Andreyev, K. Van de Vel, A. Barzakh, A. De Smet, H. De Witte, D.V. Fedorov, V.N. Fedoseyev, S. Franchoo, M. Górska, M. Huyse, Z. Janas, U. Köster, W. Kurcewicz, J. Kurpeta, V.I. Mishin, K. Partes, A. Plochocki, P. Van Duppen and L. Weissman, Eur. Phys. J. A **14**, 63 (2002).

[And02b] A.N. Andreyev, M. Huyse, K. Van de Vel, P. Van Duppen, O. Dorvaux, P. Greenlees, K. Helariutta, P. Jones, R. Julin, S. Juutinen, H. Kettunen, P. Kuusiniemi, M. Leino, M. Muikku, P. Nieminen, P. Rahkila, J. Uusitalo, R. Wyss, K. Hauschild and Y. Le Coz, Phys. Rev. C **66**, 014313 (2002).

[And03] A.N. Andreyev *et al.*, private communication, to be published (2003).

[Arm71] P. Armbruster, J. Eidens, J.W. Grüter, H. Lawin, E. Roeckl and K. Sistemich, Nucl. Instr. and Meth. **91**, 499 (1971).

[Art98] A. Artna-Cohen, Nucl. Data Sheets **83**, 921 (1998).

[Bat99] J.C. Batchelder, K.S. Toth, C.R. Bingham, L.T. Brown, L.F. Conticchio, C.N. Davids, R.J. Irvine, D. Severyniak, W.B. Walters, J. Wauters, E.F. Zganjar, J.L. Wood, C. DeCoster, B. Decroix and K. Heyde, Eur. Phys. J. A **5**, 49 (1999).

[Bax93] A.M. Baxter, A.P. Byrne, G.D. Dracoulis, R.V.F. Janssens, I.G. Bearden, R.G. Henry, D. Nisius, C.N. Davids, T.L. Khoo, T. Lauritsen, H. Penttilä, D.J. Henderson and M.P. Carpenter, Phys. Rev. C **48**, R2140 (1993).

[Bea92] C.W. Beausang, S.A. Forbes, P. Fallon, P.J. Nolan, P.J. Twin, J.N. Mo, J.C. Lisle, M.A. Bentley, J. Simpson, F.A. Beck, D. Curien, G. DeFrance, G Duchêne and D. Popescu, Nucl. Instr. and Meth. A **313**, 37 (1992).

[Ben79] R. Bengtsson and S. Frauendorf, Nucl. Phys. A **327**, 139 (1979).

[Ber69] I. Bergström, C.J. Herrlander, P. Thieberger and J. Blomqvist, Phys. Rev. **181**, 1642 (1969).

[Ber95] L.A. Bernstein, J.A. Cizewski, H.-Q. Jin, W. Younes, R.G. Henry, L.P. Farris, A. Charos, M.P. Carpenter, R.V.F. Janssens, T.L. Khoo, T. Lauritsen, I.G. Bearden, D. Ye, J.A. Becker, E.A. Henry, M.J. Brinkman, J.R. Hughes, A. Kuhnert, T.F. Wang, M.A. Stoyer, R.M. Diamond, F.S. Stephens, M.A. Deleplanque, A.O. Macchiavelli, I.Y. Lee, B. Cederwall, J.R.B. Oliveira, J. Burde, P. Fallon, C. Duyar, J.E. Draper, E. Rubel and D.T. Vo, Phys. Rev. C **52**, 621 (1995).

[Boh41] N. Bohr, Phys. Rev. **59**, 270 (1941).

[Bon76] J. Bonn, G. Huber, H.-J. Kluge and E.W. Otten, Z. Physik A **276**, 203 (1976).

[Bra80] R.A. Braga, W.R. Western, J.L. Wood, R.W. Fink, R. Stone, C.R. Bingham and L.L. Riedinger, Nucl. Phys. A **349**, 61 (1980).

[Bro77] R. Brock, C. Günther, H. Hübel, A. Kleinrahm, D. Mertin, P. Meyer and R. Tischler, Nucl. Phys. A **278**, 45 (1977).

[Bro82] R. Broda, C. Günther and B.V. Thirumala Rao, Nucl. Phys. A **389**, 366 (1982).

[Bro92] R. Broda, R.H. Mayer, I.G. Bearden, Ph. Benet, P.J. Daly, Z.W. Grabowski, M.P. Carpenter, R.V.F. Janssens, T.L. Khoo, T. Lauritsen, E.F. Moore, S. Lunardi and J. Blomqvist, Phys. Rev. Lett. **68**, 1671 (1992).

[But96] P.A. Butler, P.M. Jones, K.J. Cann, J.F.C. Cocks, G.D. Jones, R. Julin and W.H. Trzaska, Nucl. Instr. and Meth. A **381**, 433 (1996).

[Car97] M.P. Carpenter, R.V.F. Janssens, H. Amro, D.J. Blumenthal, L.T. Brown, D. Seweryniak, P.J. Woods, D. Ackermann, I. Ahmad, C. Davids, S.M. Fischer, G. Hackman, J.H. Hamilton, J. Simpson and J. Wauters, Phys. Rev. Lett. **78**, 3650 (1997).

[Cha86] T. Chapuran, K. Dybdal, D.B. Fossan, T. Lönnroth, W.F. Piel, Jr., D. Horn and E.K. Warburton, Phys. Rev. C **33**, 130 (1986).

[Coc98] J.F.C. Cocks, M. Muikku, W. Korten, R. Wadsworth, S. Chmel, J. Domscheit, P.T. Greenlees, K. Helariutta, I. Hibbert, M. Houry, D. Jenkins, P. Jones, R. Julin, S. Juutinen, H. Kankaanpää, H. Kettunen, P. Kuusiniemi, M. Leino, Y. Le Coz, R. Lucas, E. Mergel, R.D. Page, A. Savelius and W. Trzaska, Eur. Phys. J. A **3**, 17 (1998).

[Coe85] E. Coenen, K. Deneffe, M. Huyse, P. Van Duppen and J.L. Wood, Phys. Rev. Lett. **54**, 1783 (1985).

[Coe86] E. Coenen, K. Deneffe, M. Huyse, P. Van Duppen and J.L. Wood, Z. Phys. A **324**, 485 (1986).

[Cre91] J. Cresswell, Eurogam project documentation, EDOC073, Nuclear Structure Software Support Group, Liverpool University, February 1991.

[Dav96] C.N. Davids, P.J. Woods, H.T. Penttilä, J.C. Batchelder, C.R. Bingham, D.J. Blumenthal, L.T. Brown, B.C. Busse, L.F. Conticchio, T. Davinson, D.J. Henderson, R.J. Irvine, D. Severyniak, K.S. Toth, W.B. Walters and B.E. Zimmerman, Phys. Rev. Lett. **76**, 592 (1996).

[Dia63] R.M. Diamond and F.S. Stephens, Nucl. Phys. A **45**, 632 (1963).

[Don83] F. Dönau and S. Frauendorf, Proceedings of the Conference on High Angular Momentum Properties of Nuclei, Oak Ridge, Tennessee, USA, 1982, edited by N.R. Johnson (Harwood, New York, 1983), p. 143.

[Don87] F. Dönau, Nucl. Phys. A **471**, 469 (1987).

[Dra88] G.D. Dracoulis, A.E. Stuchbery, A.O. Macchiavelli, C.W. Beausang, J.Burde, M.A. Deleplanque, R.M. Diamond and F.S. Stephens, Phys. Lett. B **208**, 365 (1988).

[Dra98] G.D. Dracoulis, A.P. Byrne and A.M. Baxter, Phys. Lett. B **432**, 37 (1998).

[Dra99] G.D. Dracoulis, A.P. Byrne, A.M. Baxter, P.M. Davidson, T. Kibédi, T.R. McGoram, R.A. Bark and S.M. Mullins, Phys. Rev. C **60**, 014303 (1999).

[Dra01] G.D. Dracoulis, T. Kibédi, A.P. Byrne, A.M. Baxter, S.M. Mullins and R.A. Bark, Phys. Rev. C **63**, 061302(R) (2001).

[Dup87] P. Van Duppen, E. Coenen, K. Deneffe, M. Huyse and J.L. Wood, Phys. Rev. C **35**, 1861 (1987).

[Fan91] B. Fant, R.J. Tanner, P.A. Butler, A.N. James, G.D. Jones, R.J. Poynter, C.A. White, K.L. Ying, D.J.G. Love, J. Simpson and K.A. Connell, J. Phys. G: Nucl. Part. Phys. **17**, 319 (1991).

[Fir96] R.B. Firestone, V.S. Shirley, C.M. Baglin, S.Y.F. Chu and J. Zipkin, *Table of Isotopes*, 8^{th} ed. Vol. II, John Wiley & Sons, Inc., New York (1996).

[Fra75] S. Frauendorf and V.V. Paskevich, Phys. Lett. **55B**, 365 (1975).

[Fra93] S. Frauendorf, Nucl. Phys. A **557**, 259c (1993).

[Ghi88] A. Ghiorso, S. Yashita, M.E. Leino, L. Frank, J. Kalnins, P. Armbruster, J.-P. Dufour and P.K. Lemmertz, Nucl. Instr. and Meth. A **269**, 192 (1988).

[Har65] S.M. Harris, Phys. Rev. C **138**, 509 (1965).

[Hee93] J. Heese, K.H. Maier, H. Grawe, J. Grebosz, H. Kluge, W. Meszynski, M. Schramm, R. Schubart, K. Spohr and J. Styczen, Phys. Lett. B **302**, 390 (1993).

[Hel96] K. Helariutta, T. Enqvist, P. Jones, R. Julin, S. Juutinen, P. Jämsen, H. Kankaanpää, P. Kuusiniemi, M. Leino, M. Muikku, M. Piiparinen, A. Savelius, W.H. Trzaska, S. Törmänen, J. Uusitalo, R.G. Allatt, P.A. Butler, P.T. Greenlees and R.D. Page, Phys. Rev. C **54**, R2799 (1996).

[Hel99] K. Helariutta, J.F.C. Cocks, T. Enqvist, P.T. Greenlees, P. Jones, R. Julin, S. Juutinen, P. Jämsen, H. Kankaanpää, H. Kettunen, P. Kuusiniemi, M. Leino, M. Muikku, M. Piiparinen, P. Rahkila, A. Savelius, W.H. Trzaska, S. Törmänen, J. Uusitalo, R.G. Allatt, P.A. Butler, R.D. Page and M. Kapusta, Eur. Phys. J. A **6**, 289 (1999).

[Hey83] K. Heyde, P. Van Isacker, M. Waroquier, J.L. Wood and R.A. Meyer, Phys. Rep. **102**, 291 (1983).

[Hey87] K. Heyde, J. Jolie, J. Moreau, J. Ryckebusch, M. Waroquier, P. Van Duppen, M. Huyse and J.L. Wood, Nucl. Phys. A **466**, 189 (1987).

[Hey88] K. Heyde, J. Ryckebusch, M. Waroquier and J.L. Wood, Nucl. Phys. A **484**, 275 (1988).

[Hey89] K. Heyde, C. De Coster, J. Ryckebusch and M. Waroquier, Phys. Lett B **218**, 287 (1989)

[Hüb78] H. Hübel, A. Kleinrahm, C. Günther, D. Mertin and R. Tischler, Nucl. Phys. A **294**, 177 (1978).

[Hüb83] H. Hübel, M. Guttormsen, K.P. Blume, J. Recht, A. von Grumbkow, K. Hardt, P. Schüler, Y.K. Agarwal and A. Maj, Z. Phys. A **314**, 89 (1983).

[Hür02] A. Hürstel, M. Rejmund, E. Bouchez, P.T. Greenlees, K. Hauschild, S. Juutinen, H. Kettunen, W. Korten, Y. Le Coz, P. Nieminen, Ch. Theisen, A.N. Andreyev, F. Becker, T. Enqvist, P.M. Jones, R. Julin, H. Kankaanpää, A. Keenan, P. Kuusiniemi, M. Leino, A.-P. Leppänen, M. Muikku, J. Pakarinen, P. Rahkila and J. Uusitalo, Eur. Phys. J. A **15**, 329 (2002).

[Hür03] A. Hürstel *et al.*, to be published.

[Jon95] P.M. Jones, Ph.D. Thesis, University of Liverpool, September 1995.

[Jon99] P. Jones, P. Rahkila, J.F.C. Cocks, K. Helariutta, R. Julin, S. Juutinen, H. Kankaanpää, P. Kuusiniemi, Y. Le Coz, M. Leino, M. Muikku, P. Nieminen and A. Savelius, Acta Physica Polonica B **30**, 671 (1999).

[Jul01] R. Julin, K. Helariutta and M. Muikku, J. Phys. G: Nucl. Part. Phys. **27**, R109 (2001).

[Juu94] S. Juutinen, R. Julin, M. Piiparinen, P. Ahonen, B. Cederwall, C. Fahlander, A. Lampinen, T. Lönnroth, A. Maj, S. Mitarai, D. Müller, J. Nyberg, P. Simecek, M. Sugawara, I. Thorslund, S. Törmänen, A. Virtanen and R. Wyss, Nucl. Phys. A **573**, 306 (1994).

[Kan03] H. Kankaanpää, P.A. Butler, P.T. Greenlees, R.-D. Herzberg, R.D. Humphreys, G.D. Jones, P. Jones, R. Julin, A. Keenan, L. Miettinen, P. Rahkila and C. Scholey, to be published.

[Ket03a] H. Kettunen, S. Eeckhaudt, T. Enqvist, T. Grahn, P.T. Greenlees, P. Jones, R. Julin, S. Juutinen, A. Keenan, P. Kuusiniemi, M. Leino, A.-P. Leppänen, P. Nieminen, J. Pakarinen, P. Rahkila, C. Scholey and J. Uusitalo. Proceedings of Conference Proton-Emitting Nuclei, Second International Symposium PROCON 2003, Legnaro, Italy, 12-15 February 2003, edited by E. Maglione and F. Soramel (AIP Conference proceedings **681**, Melville, New York, 2003), p. 26.

[Ket03b] H. Kettunen, T. Enqvist, M. Leino, K. Eskola, P.T. Greenlees, K. Helariutta, P. Jones, R. Julin, S. Juutinen, H. Kankaanpää, H. Koivisto, P. Kuusiniemi, M. Muikku, P. Nieminen, P. Rahkila and J. Uusitalo, Eur. Phys. J. A **16**, 457 (2003).

[Ket03c] H. Kettunen, T. Enqvist, T. Grahn, P.T. Greenlees, P. Jones, R. Julin, S. Juutinen, A. Keenan, P. Kuusiniemi, M. Leino, A.-P. Leppänen, P. Nieminen, J. Pakarinen, P. Rahkila and J. Uusitalo, Eur. Phys. J. A **17**, 537 (2003).

[Kno89] G.F. Knoll, *Radiation Detection and Measurement*, John Wiley & Sons, Inc., 1989, p. 322.

[Kre88] A.J. Kreiner, J. Davidson, M. Davidson, H. Mosca, L.L. Riedinger, C.R. Bingham, M.W. Guidry and A.C. Kahler, Phys. Rev. C **38**, 2674 (1988).

[Kum92] J. Kumpulainen, R. Julin, J. Kantele, A. Passoja, W.H. Trzaska, E. Verho, J. Väärämäki, D. Cutoiu and M. Ivascu, Phys. Rev. C **45**, 640 (1992).

[Lag91] J.M. Lagrange, M. Pautrat, J.S. Dionisio, Ch. Vieu and J. Vanhorenbeeck, Nucl. Phys. A **530**, 437 (1991).

[Lan95] G. Lane, G.D. Dracoulis, A.P. Byrne, P.M. Walker, A.M. Baxter, J.A. Sheikh and W. Nazarewicz, Nucl. Phys. A **586**, 316 (1995).

[Lei83] M. Leino, Ph.D. thesis, Department of Physics, University of Helsinki, Helsinki, Finland, Report HU-P-D37, 1983 (unpublished).

[Lei95a] M. Leino, J. Äystö, T. Enqvist, P. Heikkinen, A. Jokinen, M. Nurmia, A. Ostrowski, W.H. Trzaska, J. Uusitalo, K. Eskola, P. Armbruster and V. Ninov, Nucl. Instr. and Meth. B **99**, 653 (1995).

[Lei95b] M. Leino, J. Äystö, T. Enqvist, A. Jokinen, M. Nurmia, A. Ostrowski, W.H. Trzaska, J. Uusitalo, K. Eskola, P. Armbruster and V. Ninov, Acta Physica Polonica B **26**, 309 (1995).

[Lir76] S. Liran and N. Zeldes, Atomic Data Nuclear Data Tables **17**, 431 (1976).

[Lon78] T. Lönnroth and B. Fant, Physica Scripta **18**, 172 (1988).

[Lon79] T. Lönnroth, J. Blomqvist, I. Bergström and B. Fant, Physica Scripta **19**, 233 (1979).

[Lon81] T. Lönnroth, Department of Physics, University of Jyväskylä, Research Report 4/1981 (unpublished).

[Lon82] T. Lönnroth, Z. Phys. A **307**, 175 (1982).

[Lon86] T. Lönnroth, C.W. Beausang, D.B. Fossan, L. Hildingsson, W.F. Piel, Jr., M.A. Quader, S. Vadja, T. Chapuran and E.K. Warburton, Phys. Rev. C **33**, 1641 (1986).

[Mor56] H. Morinaga, Phys. Rev. **101**, 254 (1956).

[Mos89] M. Moszyński, J.H. Bjerregard, J.J. Gaardhoje, B. Herskind, P. Knudsen and G. Sletten, Nucl. Instr. and Meth. A **280**, 73 (1989).

[Mui98] M. Muikku, J.F.C. Cocks, K. Helariutta, P. Jones, R. Julin, S. Juutinen, H. Kankaanpää, H. Kettunen, P. Kuusiniemi, M. Leino, P. Rahkila, A. Savelius, W.H. Trzaska, J. Uusitalo, P.T. Greenlees and R.D. Page, Phys. Rev. C **58**, R3033 (1998).

[Mui01] M. Muikku, P.T. Greenlees, K. Hauschild, K. Helariutta, D.G. Jenkins, P. Jones, R. Julin, S. Juutinen, H. Kankaanpää, N.S. Kelsall, H. Kettunen, P. Kuusiniemi, M. Leino, C. J. Moore, P. Nieminen, C.D. O'Leary, R.D. Page, P. Rahkila, W. Reviol, M.J. Taylor, J. Uusitalo and R. Wadsworth, Phys. Rev. C **64**, 044308 (2001).

[Naz93] W. Nazarewicz, Phys. Lett. B **305**, 195 (1993).

[New70] J.O. Newton, S.D. Cirilov, F.S. Stephens and R.M. Diamond, Nucl. Phys. A **148**, 593 (1970).

[Nie01] P. Nieminen, J.F.C. Cocks, O. Dorvaux, P.T. Greenlees, K. Helariutta, P.M. Jones, R. Julin, S. Juutinen, H. Kankaanpää, H. Kettunen, P. Kuusiniemi, M. Leino, M. Muikku, P. Rahkila, A. Savelius, J. Uusitalo, A.N. Andreyev, F. Becker, K. Eskola, K. Hauschild, M. Houry, M. Huyse, W. Korten, Y. Le Coz, R. Lucas, T. Lönnroth, Ch. Theisen, K. Van de Vel, P. Van Duppen, N. Amzal, P.A. Butler, N. Hammond, C. Scholey and R. Wyss, Acta Physica Polonica B **32**, 1019 (2001).

[Nie03a] P. Nieminen, S. Juutinen, J.F.C. Cocks, O. Dorvaux, T. Enqvist, T. Grahn, P.T. Greenlees, K. Helariutta, P.M. Jones, R. Julin, H. Kankaanpää, A. Keenan, H. Kettunen, P. Kuusiniemi, M. Leino, A.-P. Leppänen, M. Muikku, J. Pakarinen, P. Rahkila, A. Savelius, J. Uusitalo, E. Bouchez, A. Hürstel, K. Hauschild, W. Korten, Y. Le Coz, M. Rejmund, Ch. Theisen, N. Amzal, A.N. Andreyev, K. Eskola, N. Hammond, M. Huyse, T. Lönnroth, C. Scholey, P. Van Duppen and R. Wyss, Proceedings of Conference Frontiers of Nuclear Structure, Berkeley, California, USA, 29 July - 2 August 2002, edited by P. Fallon and R. Clark (AIP Conference proceedings **656**, Melville, New York, 2003), p. 63.

[Nie03b] P. Nieminen, S. Juutinen, A.N. Andreyev, J.F.C. Cocks, O. Dorvaux, K. Eskola, P.T. Greenlees, K. Hauschild, K. Helariutta, M. Huyse, P.M. Jones, R. Julin, H. Kankaanpää, H. Kettunen, P. Kuusiniemi, Y. Le Coz. M. Leino T. Lönnroth, M. Muikku, P. Rahkila, A. Savelius, J. Uusitalo, N. Amzal, N.J. Hammond, C. Scholey and R. Wyss, to be published.

[Nil55] S.G. Nilsson, Kgl. Dan. Viden. Selsk. Mat. Fys. Medd. No. **16**, 29 (1955)

[Nol85] P.J. Nolan, D.W. Gifford and P.J. Twin, Nucl. Instr. and Meth. A **236**, 95 (1985).

[Nov02] Yu.N. Novikov, F. Attallah, F. Bosch, M. Falch, H. Geissel, M. Hausmann, Th. Kerscher, O. Klepper, H.-J. Kluge, C. Kozhuharov, Yu.A. Litvinov, K.E.G. Löbner, G. Münzenberg, Z. Patyk, T. Radon, C. Scheidenberger, A.H. Wapstra and H. Wollnik, Nucl. Phys. A **697**, 92 (2002).

[Oro99] A.M. Oros, K. Heyde, C. De Coster, B. Decroix, R. Wyss, B.R. Barrett and P. Navratil, Nucl. Phys. A **645**, 107 (1999).

[Pag03] R.D. Page, A.N. Andreyev, D.E. Appelbe, P.A. Butler, S.J. Freeman, P.T. Greenlees, R.-D. Herzberg, D.G. Jenkins, G.D. Jones, P. Jones, D.T. Joss, R. Julin, H. Kettunen, M. Leino, P. Rahkila, P.H. Regan, J. Simpson, J. Uusitalo, S.M. Vincent and R. Wadsworth, Nucl. Instr. and Meth. B **204**, 634 (2003).

[Pau95] E.S. Paul, P.J. Woods, T. Davinson, R.D. Page, P.J. Sellin, C.W. Beausang, R.M. Clark, R.A. Cunningham, S.A. Forbes, D.B. Fossan, A. Gizon, J. Gizon, K. Hauschild, I.M. Hibbert, A.N. James, D.R. LaFosse, I. Lazarus, H. Schnare, J. Simpson, R. Wadsworth and M.P. Waring, Phys. Rev. C **51**, 78 (1995).

[Pie85] W.F. Piel, Jr., T. Chapuran, K. Dybdal, D.B. Fossan, T. Lönnroth, D. Horn and E.K. Warburton, Phys. Rev. C **31**, 2087 (1985).

[Plo93a] A.J.M. Plompen, M.N. Harakeh, W.H.A. Hesselink, G. van't Hof, N. Kalantar-Nayestanaki, J.P.S. van Schagen, M.P. Carpenter, I. Ahmad, I.G. Bearden, R.V.F. Janssens, T.L. Khoo, T. Lauritsen, Y. Liang, U. Garg, W. Reviol and D. Ye, Nucl. Phys. A **562**, 61 (1993).

[Plo93b] A.J.M. Plompen, J. Blomqvist, M.P. Carpenter, M.N. Harakeh, W.H.A. Hesselink, R.V.F. Janssens, R.J. Liotta and N. Sandalescu, Nucl. Phys. A **562**, 88 (1993).

[Pol01] G.L. Poli, C.N. Davids, P.J. Woods, D. Severyniak, M.P. Carpenter, J.A. Cizewski, T. Davinson, A. Heinz, R.V.F. Janssens, C.J. Lister, J.J. Ressler, A.A. Sonzogni, J. Uusitalo and W.B. Walters, Phys. Rev. C **63**, 044304 (2001).

[Pom90] C. Pomar, J. Blomqvist, R.J. Liotta and A. Insolia, Nucl. Phys. A **515**, 381 (1990).

[Pre47] M.A. Preston, Phys. Rev. **71**, 865 (1947).

[Rad95] D.C. Radford, Nucl. Instr. and Meth. A **361**, 297 (1995).

[Rad00] T. Radon, H. Geissel, G. Münzenberg, B. Franzke, Th. Kerscher, F. Nolden, Yu.N. Novikov, Z. Patyk, C. Scheidenberger, F. Attallah, K. Beckert, T.

Beha, F. Bosch, H. Eickhoff, M. Falch, Y. Fujita, M. Hausmann, F. Herfurth, H. Irnich, H.C. Jung, O. Klepper, C. Kozhuharov, Yu.A. Litvinov, K.E.G. Löbner, F. Nickel, H. Reich, W. Schwab, B. Schlitt, M. Steck, K. Sümmerer, T. Winkler and H. Wollnik, Nucl. Phys. A **677**, 75 (2000).

[Ras59] J.O. Rasmussen, Phys. Rev. **113**, 1593 (1959).

[Rev95] W. Reviol, L.L. Riedinger, J.M. Lewis, W.F. Mueller, C.R. Bingham, J.Y. Zhang and B.E. Zimmerman, Physica Scripta **T56**, 167 (1995).

[Ros78] F. Rösel, H.M. Fries, K. Alder and H.C. Pauli, Atomic Data Nuclear Data Tables **21**, 291 (1978).

[Ruy86] J.J. Van Ruyven, J. Penninga, W.H.A. Hesselink, P. Van Nes, K. Allaart, E.J. Hengeveld, H. Verheul, M.J.A. De Voigt, Z. Sujkowski and J. Blomqvist, Nucl. Phys. A **449**, 579 (1986).

[Sav98] A. Savelius, S. Juutinen, K. Helariutta, P. Jones, R. Julin, P. Jämsen, M. Muikku, M. Piiparinen, J. Suhonen, S. Törmänen, R. Wyss, P.T. Greenlees, P. Simecek and D. Cutoiu, Nucl. Phys. A **637**, 491 (1998).

[Sch84] K.-H. Schmidt, C.-C. Sahm, K. Pielenz and H.-G. Clerc, Z. Phys. A **316**, 19 (1984).

[Sha61] A. de Shalit, Phys. Rev. **122**, 1530 (1961).

[Sim86] R.S. Simon, K.-H. Schmidt, F.P. Hessberger, S. Hlavac, M. Honusek, G. Münzenberg, H.-G. Clerc, U. Gollerthan and W. Schwab, Z. Phys. A **325**, 197 (1986).

[Sin02] B. Singh, R. Zywina and R.B. Firestone, Nucl. Data Sheets **97**, 241 (2002).

[Smi99] M.B. Smith, R. Chapman, J.F.C. Cocks, O. Dorvaux, K. Helariutta, P.M. Jones, R. Julin, S. Juutinen, H. Kankaanpää, H. Kettunen, P. Kuusiniemi, Y. Le Coz, M. Leino, D.J. Middleton, M. Muikku, P. Nieminen, P. Rahkila, A. Savelius and K.-M. Spohr, Eur. Phys. J. A **5**, 43 (1999).

[Ste75] F.S. Stephens, Rev. Mod. Phys. **47**, 43 (1975).

[Tan85] I. Tanihata, H. Hamagaki, O. Hashimoto, Y. Shida, N. Yoshikawa, K. Sugimoto, O. Yamakawa, T. Kokayashi and N. Takahashi, Phys. Rev. Lett. **55**, 2676 (1985).

[Twi85] P.J. Twin, A.H. Nelson, B.M. Nyako, D. Howe, H.W. Cranmer-Gordon, D. Elenkov, P.D. Forsyth, J.K. Jabber, J.F. Sharpey-Schafer, J. Simpson and G. Sletten, Phys. Rev. Lett. **55**, 1380 (1985).

[Twi86] P.J. Twin, B.M. Nyako, A.H. Nelson, J. Simpson, M.A. Bentley, H.W. Cranmer-Gordon, P.D. Forsyth, D. Howe, A.R. Mokhtar, J.D. Morrison, J.F. Sharpey-Schafer and G. Sletten, Phys. Rev. Lett. **57**, 811 (1986).

[Uus03] J. Uusitalo, private communication (2003).

[Vel02] K. Van de Vel, A.N. Andreyev, M. Huyse, P. Van Duppen, J.F.C. Cocks, O. Dorvaux, P.T. Greenlees, K. Helariutta, P. Jones, R. Julin, S. Juutinen, H. Kettunen, P. Kuusiniemi, M. Leino, M. Muikku, P. Nieminen, K. Eskola and R. Wyss, Phys. Rev. C **65**, 064301 (2002).

[Vel03] K. Van de Vel, A.N. Andreyev, R.D. Page, H. Kettunen, P.T. Greenlees, P. Jones, R. Julin, S. Juutinen, H. Kankaanpää, A. Keenan, P. Kuusiniemi, M. Leino, M. Muikku, P. Nieminen, P. Rahkila, J. Uusitalo, K. Eskola, A. Hürstel, M. Huyse, Y. Le Coz, M.B. Smith, P. Van Duppen and R. Wyss, Eur. Phys. J. A **17**, 167 (2003).

[Wau93] J. Wauters, P. Dendooven, M. Huyse, G. Reusen, P. Van Duppen, P. Lievens and the ISOLDE Collaboration, Phys. Rev. C **47**, 1447 (1993).

[Woo92] J.L. Wood, K. Heyde, W. Nazarewicz, M. Huyse and P. van Duppen, Phys. Rep. **215**, 101 (1992).

[Wys02] R. Wyss, private communication (2002).

[Yam67] T. Yamazaki, Nuclear Data A **3**, 1 (1967).